# Multidimensional Scan of the Saturnian E-ring based on the Data Record of Cassini's Cosmic Dust Analyzer

Dissertation

zur Erlangung des akademischen Grades

*Doktor der Naturwissenschaften*

(Dr. rer. nat.)

Eingereicht im

Fachbereich Geowissenschaften

Freie Universität Berlin

Von

Lenz Nölle

Berlin, 2022

**Erstgutachter/First Reviewer:**

Prof. Dr. Frank Postberg

**Zweitgutachter/Second Reviewer:**

Prof. Dr. Jürgen Schmidt

**Tag der Disputation/Day of Disputation:**

27. Juli 2022

# Abstract

The Cassini spacecraft orbited Saturn from 2004 to 2017. During this period, Cassini's onboard dust instrument – the Cosmic Dust Analyzer (CDA) – recorded numerous in situ time of flight mass spectra, generated from µm to sub-µm sized dust particles. Most of these spectra originate from ice particles sampled in Saturn's large, diffuse E-ring. This ring is mainly sustained by material ejected from the cryo-volcanic plumes at the south polar terrain of Saturn's icy moon Enceladus. Previous analyses of CDA spectra revealed the existence of three different compositional main types of ice particles: salt- and organic-poor (Type 1), salt-poor but enriched in organics (Type 2) and salt-rich (Type 3). A new compositional type was discovered during the course of this work, called Type 5. Its CDA spectra indicate a very high salt concentration; far above the level found for Type 3 particles of about 1 % by mass. So this work represents the first, large-scale investigation of the spatial distribution of these four types to study the compositional structure of the E-ring. For this purpose, more than 10000 CDA spectra of ice grains were analyzed for their composition and particle size with respect to the spacecraft position and trajectory.

The results of this investigation not only revealed distinct spatial correlations and trends but are also in good agreement with previously published E-ring results, obtained during close Enceladus flybys. Moreover, they show that, although the absolute number density of all E-ring grains drops when moving radially outwards from Enceladus or vertically away from Saturn's equatorial ring plane, the relative frequencies of the compositional types vary significantly. Type 1 particles generally represent the majority of all ice particles in the E-ring and become relatively more frequent at larger radial and vertical distances. Type 2 particles exhibit the opposite trend with the relative frequency declining at larger distances. Thus, it is proposed that Type 2 particles are converted into secondary Type 1 particles, through photochemical degradation of the embedded organic molecules. For Type 3 particles the radial and vertical trends differ. Radially, the relative frequency first rises to a maximum and then decreases, while vertically it remains almost constant, with only a minor indication of a North-South asymmetry. The newly discovered particle type (Type 5) is most frequently detected in a relatively narrow region of the E-ring, between the orbital distances of Dione and Rhea, confirming existing theories about the dynamical evolution of E-ring grains. This argues against a direct Enceladian source, instead favoring a formation within the E-ring itself. Hence, it is proposed that Type 5 represents secondary particles, formed from Type 3 grains via plasma sputtering of the more volatile water component.

To understand the impact, that particle composition has on the determination of the particle size, particularly the organic substances in the ice particles, laboratory experiments were undertaken using a Laser-Induced Liquid Beam Ion Desorption (LILBID) approach. By irradiating a µm-sized liquid water beam with a pulsed, infrared laser, LILBID simulates the impact ionization process of ice grains in space. The experiments revealed a distinct difference in ion yields between salt-rich and organic-rich compositions. While the latter increases the ion yields just slightly, compared to pure water, the addition of salts increases them significantly. Considering these results, it is inferred that Type 2 particles are, on average, the largest particles. The average sizes of the other three types overlap within the errors, depending on the particular radial distance to Saturn. The overall shape of the radial size distribution seems to be intimately related to the particles' salinities. The average sizes of the salt-poor particle types (Type 1 and 2) decrease linearly in the inner E-ring up to 10 $R_{Saturn}$ (Saturn radius $R_{Saturn}$ = 60268 km) from Saturn, then remain more or less constant. In comparison, salt-rich particles (Type 3 and 5) exhibit a similar initial decrease but reach their minima sooner, at around 8 $R_{Saturn}$. These minima are followed by a distinct increase in the populations' average grain sizes in the outer E-ring. Although it is currently unclear why the average grain sizes of salty ice grains increase again in the outer E-ring, the two different distribution shapes – those of the salt-poor types on one side and the salt-rich types on the other – again indicate that two different transformation processes, responsible for the transformation of Type 2 to Type 1 and Type 3 to Type 5, are occurring, as also inferred from the compositional data.

# Zusammenfassung

Die Raumsonde Cassini umkreiste den Planeten Saturn von 2004 bis 2017. Während dieser Zeit zeichnete Cassinis Staubinstrument – der Cosmic Dust Analyzer (CDA) – zahlreiche Flugzeit-Massenspektren auf, die von µm bis sub-µm großen Staubteilchen erzeugt wurden. Die meisten dieser Spektren stammen von Eispartikeln aus Saturns großem, diffusen E-Ring. Dieser besteht hauptsächlich aus Material, welches von den Kryo-Vulkanen auf dem Gebiet des Südpols von Saturns Eismond Enceladus ausgeworfen werden. Erste Analysen von CDA Spektren belegen die Existenz von drei Haupttypen in der Zusammensetzung von Eispartikeln im E-Ring: Arm an Salzen und organischen Substanzen (Typ 1), arm an Salzen aber reich an organischen Substanzen (Typ 2) und reich an Salzen (Typ 3). Ein neuer Typ wurde im Zuge dieser Arbeit entdeckt, genannt Typ 5. Die CDA Spektren dieses Typs deuten auf eine sehr hohe Salzkonzentration hin, weit über dem Niveau von ungefähr 1 %-Masse, welches für den Typ 3 ermittelt wurde. Diese Arbeit repräsentiert nun die erste, großräumige Untersuchung der räumlichen Verteilung dieser vier Typen, um die Struktur der Zusammensetzung des E-Rings zu erforschen. Zu diesem Zweck wurden mehr als 10000 CDA Spektren von Eisteilchen auf deren Zusammensetzung und Teilchengröße analysiert und in Bezug zur Raumschiffposition und -trajektorie gesetzt.

Die Ergebnisse dieser Untersuchung haben nicht nur ausgeprägte, räumliche Zusammenhänge und Trends offengelegt, sondern stimmen auch gut mit zuvor publizierten Ergebnissen bezüglich des E-Rings überein, deren Daten während naher Enceladus-Vorbeiflüge aufgezeichnet wurden. Zudem zeigen die Untersuchungsergebnisse, dass, obwohl die absolute Teilchenzahldichte aller E-Ring Teilchen deutlich abnimmt, wenn man sich von Enceladus radial nach außen oder vertikal von der äquatorialen Ringebene des Saturn wegbewegt, die relativen Häufigkeiten der Teilchentypen deutlich variieren. Grundsätzlich repräsentieren Typ 1 Teilchen die Mehrheit aller Eisteilchen im E-Ring, doch ihre relative Häufigkeit nimmt mit größeren radialen und vertikalen Abständen noch zu. Typ 2 Teilchen zeigen den entgegengesetzten Trend und deren relative Häufigkeit nimmt mit größeren Abständen ab. Als Erklärung wird ein photochemischer Abbau der organischen Substanzen in den Typ 2 Partikeln vorgeschlagen, durch den diese in sekundäre Typ 1 Teilchen umgewandelt werden. Für Typ 3 Teilchen unterscheiden sich die radialen und vertikalen Trends. Während in radialer Richtung die relative Häufigkeit zunächst zu einem lokalen Maximum ansteigt und dann wieder abnimmt, bleibt diese in vertikaler Richtung auf einem ungefähr konstanten Niveau, mit einer schwachen Andeutung einer Nord-Süd-Asymmetrie. Der neu entdeckte

Teilchentyp (Typ 5) wird am häufigsten in einem relativ schmalen Bereich des E-Rings zwischen den Bahnen von Dione und Rhea detektiert, was bestehende Theorien zur dynamischen Entwicklung von E-Ring Teilchen bestätigt. Dies spricht gegen eine direkte Herkunft von Enceladus sondern für eine Bildung innerhalb des E-Rings selbst. Daher wird hier vorgeschlagen, dass der Typ 5 sekundäre Teilchen repräsentiert, welche sich aus Typ 3 Teilchen durch Plasma Sputtering der volatileren Wasser Komponente bildet.

Um den Einfluss zu verstehen, welcher die Teilchenzusammensetzung auf die Bestimmung der Teilchengrößen hat, im Besonderen die organischen Subtanzen in den Eisteilchen, wurden Laborexperimente mithilfe eines laserinduzierten Flüssigstrahl-Desorptions (LILBID) Mechanismus durchgeführt. Die Bestrahlung eines µm großen Wasserstrahls mit einem gepulsten Infrarotlaser simuliert dabei den Prozess der Einschlagsionisation von Eisteilchen im Weltall. Die Experimente ergaben einen deutlichen Unterschied der Ionenausbeuten zwischen Salz-reichen und Organik-reichen Zusammensetzungen. Während letztere die Ionenausbeute nur geringfügig ansteigen lassen, relativ zu purem Wasser, erhöht die Zugabe von Salzen die Ionenausbeute deutlich. Die Berücksichtigung dieser Ergebnisse egab, dass Typ 2 Teilchen im Mittel die größten Teilchen darstellen. Die durchschnittlichen Teilchengrößen der anderen Teilchentypen überlappen innerhalb der Fehlergrenzen, in Abhängigkeit von der betrachteten Entfernung zu Saturn. The Gesamtform der radialen Teilchengrößenverteilung scheint eng mit dem Salzgehalt der Teilchen in Verbindung zu stehen. Die durchschnittlichen Teilchengrößen der salzarmen Teilchen Typen (Typ 1 und 2) nehmen im inneren E-Ring bis 10 $R_{Saturn}$ (Saturnradius $R_{Saturn}$ = 60268 km) relativ zu Saturn linear ab und verbleiben dann ungefähr konstant. Zum Vergleich, salzreiche Teilchen (Typ 3 und 5) weisen eine ähnliche, anfängliche Abnahme auf, erreichen ihre Minima allerdings schon bei ungefähr 8 $R_{Saturn}$. Auf diese Minima folgt allerdings ein deutlicher Anstieg der durchschnittlichen Teilchengrößen im äußeren E-Ring. Obwohl gegenwärtig unklar ist warum genau die durchschnittliche Teilchengröße salzreicher Teilchen im äußeren E-Ring wieder zunimmt, deuten die beiden beobachteten Formen der Größenverteilungen – jene der salzarmen Typen auf der einen Seite und die der salzreichen auf der anderen – erneut darauf hin, dass zwei unterschiedliche Transformationsprozesse, verantwortlich für die Umwandlung von Typ 2 zu Typ 1 und Typ 3 zu Typ 5, vonstatten gehen, wie auch schon anhand der Daten der Teilchenzusammensetzungen gefolgert.

# Contents

# List of Figures

# List of Tables

# A. Introduction

This chapter provides an introduction and overview of the background and setting of this thesis. The first section introduces cosmic dust in the solar system, and its characteristics. This is followed by a detailed overview of the Saturnian system, the location of interest of this work. The third section is a resumé of the Cassini-Huygens space mission, which was designed to analyze the Saturn system in-depth. Its instruments provided the major part of the data used in this thesis. The last section sums up the objectives of this work.

## 1. Dust in the Solar System

Solid particles smaller than about 0.1 mm in size found in the solar system are known as cosmic dust and have a wide range of characteristics. Cosmic dust is the general term for all kinds of microscopic, solid particles of extraterrestrial (cosmic) origin. From sub-mm to nm sized particles, it spans a wide range of microscopic sizes. Three main populations can be distinguished:

- Interplanetary Dust Particles (IDP)
- Interstellar Dust (ISD)
- Circumplanetary Dust (CPD)

IDP are dust particles populating interplanetary space in the solar system. They usually originate from bodies and processes within the solar system, such as:

- Active asteroids and comets
- Geologically active moons
- Collisions between, and impacts of larger bodies
- Ejecta from micrometeorite impacts

Fig. 1: Comet Hale Bopp (C/1995 O1) during its active phase in 1997. The dust “tail” contributes to the IDP population. Image Credit: Geoff Chester/US Navy

Vice versa, the ISD particles are not descendants of the solar system but represent the dust flux from the local interstellar dust cloud. Dust inflow is caused by the relative motion of the solar system with respect to the interstellar medium and the dust thus is not dynamically bound to the solar system.

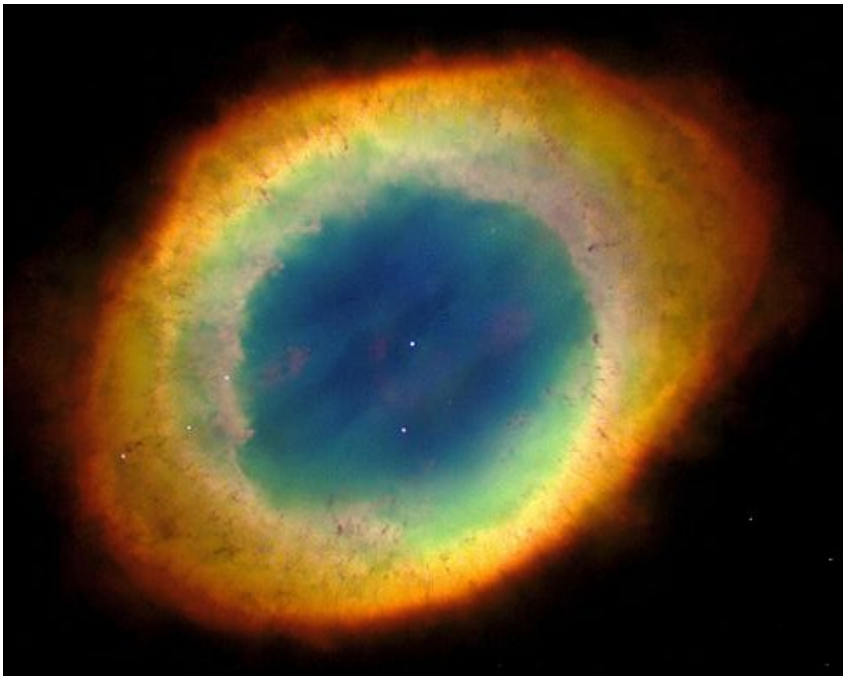

Fig. 2: The Ring Nebula (M57) in the consellation Lyra. A former star ejecting its outer layers into space. Image Credit: Hubble Heritage Team (AURA/STScI/NASA)

Contributions to the interstellar dust cloud are for example (Draine, 2003):

- Stellar nova & supernova
- Planetary nebulae

While ISD is typically not gravitationally bound to the Sun, and IDP are unbound with respect to the planets, CPD is usually found orbiting a planetary body. This kind of dust forms either within the planetary system itself (endogenic origin) or represents captured IDP (exogenic origin). In the exogenic case, the particles exhibit a wide range of orbital elements with respect to the planetary body system, with orbits often highly inclined, or even retrograde, potentially with high orbital eccentricities. Vice versa, endogenic particles share the same dynamical settings as the parent body system, most importantly the angular momentum. Therefore, they're mostly confined to the planetary system's ecliptic plane (low inclination), with low-to-moderate eccentricities, often forming planetary rings (see Fig. 6). CPD forms from similar processes to IDP: collisions, impact ejecta and active bodies but may also form from tidal disruption of smaller bodies by the central planetary body (Aggarwal & Oberbeck, 1974).

In general, cosmic dust particles can usually be assigned to one of the following compositional categories (Hillier et al., 2007a+b; Westphal et al., 2014):

- Silicates → mainly Mg-Fe-rich and Ca-Al-rich silicates (e.g. Olivine, Pyroxene & Plagioclase)
- Metals → essentially Fe/Ni-alloys (e.g. Kamacite & Taenite)
- Ices → primarily of $H_2O$ or $CO_2$; secondarily of $CH_4$, $N_2$, $NH_3$, CO and further low-mass organics
- Other minerals (e.g. carbonates, oxides or sulfides)

Each category comes along with a different thermal durability. On one side, metals, silicates and other minerals usually remain solid up to several hundred °C, before they sublimate under the low-pressure conditions of space. They are called refractory materials or just refractories. On the other side, ices maintain their solid state for significant periods of time only at temperatures below 0°C. Thus, they are also called volatile materials or just volatiles. Material sublimation temperature variations, coupled with the spatial heat distribution in the solar system, dictate the steady state spatial abundance of dust made of refractories or volatiles. Two heat sources have to be considered here:

- solar radiation
- radiogenic heating by radionuclides, e.g. $^{26}Al$, $^{40}K$ or $^{238}U$

Since cosmic dust particles are so small, they have a large surface/volume ratio. Thus, any heat produced by radioactive decays, exceeding the equilibrium with the solar radiation heat, is quickly lost through radiative emission. Therefore, radiogenic heating can be neglected and solar radiation considered to be the main direct heat source onto dust grains. Solar radiative heat continuously drops with increasing distance to the sun[a], which leads to a characteristic spatial distribution of the two material categories. The high temperatures required to sublimate and thus eliminate solid, refractory, dust particles, are only achieved in the direct vicinity of the sun. Thus, such dust particles can be found in most parts of the solar system. In contrast, dust particles of volatile materials are only found outside a characteristic distance-temperature boundary, the so-called frost line, snow line or ice line. This marks the radial distance to the Sun at which solar heating has decreased enough to keep a particular material frozen/solid, even under direct sunlight. Inside this boundary particles of the relevant material are not stable and start to sublimate. Each of volatile conpound actually possesses its own frost line, because of the varying sublimation temperatures of the materials. $H_2O$ for example exhibits one of the highest sublimation temperatures of all cosmologically-relevant volatile materials and hence its frost line is located among the closest to the sun. Consequently, the frost line of $H_2O$ can be considered to represent an innermost limit for dust particles made of volatile materials and its location determines their steady state spatial extent. Thus, any following reference to the frost line refers to the $H_2O$ frost line, if not mentioned explicitly.

The actual position of the frost line depends not only on the respective material but also both on the current solar luminosity and the opacity of the solar system. Since the latter two parameters have changed significantly during the lifetime of the solar system, the frost line has moved as well. Thus, it is necessary to distinguish between the current and the formation frost lines, that which was present when the planetary building blocks formed. In its early stages the sun had a considerably lower luminosity and the forming solar system was filled with a dense light-absorbing cloud of dust and gas, the solar nebula. Both factors resulted in significantly lower temperatures inside the solar nebula, allowing the frost line to be closer to the sun. Theoretical models (Hayashi, 1981; Podolak & Zucker, 2004; Martin & Livio, 2012; D'Angelo & Podolak, 2015) as well as observations of asteroids in the main belt between Jupiter and Mars (Abe et al., 2000[b]; Morbidelli et al., 2000) indicate that the formation frost line could have been located somewhere near today's main belt region, at around 2.7 to 3.1 AU[c]. Currently the frost

[a] $T_{rad} \sim r^{-0.5}$

[b] Part of Canup & Righter (2000)

[c] 1 AU ≈ 149 597 870 700 m (Brumfiel, 2012)

line is thought to be positioned further outwards, at around 5 AU (Jewitt et al., 2007[a]), close to Jupiter's orbit. However, it's still possible to find icy dust temporarily inside the frost line, for example near active comets.

The frost line is considered to have played an essential part in the formation of the giant planets during the early solar system (D'Angelo et al., 2010[b]). Beyond this boundary there was additional solid matter available in the form of ice dust. This allowed to form planetesimals, that were heavy enough to gravitationally capture Hydrogen and Helium gas permanently from the surrounding proto-planetary disk, eventually forming the giant planets. Vice versa, planetesimals, which formed inside the frost line, had to grow from lesser amounts of predominantly refractory dust. Due to the resulting lower masses, these planetesimals were not able to permanently capture light gases as Hydrogen or Helium. This way the inner planets gained their predominantly rocky composition, while the outer planets are called gas- or ice-giants.

[a] Part of Reipurth et al. (2007)
[b] Part of Saeger & Dotson (2010)

# 2. The Saturn System

The Saturn system is one of the, or perhaps the most, multifaceted planetary systems in the solar system. Dozens of different moons, a highly complex atmosphere and most obviously the prominent ring system make the Saturn system a very fascinating object of research, and it represents the main subject of this work. It was the destination of the Cassini-Huygens mission, which is, to date, probably one of the most successful space missions, delivering a large amount of new scientific data. This subchapter will give an overview of the planet itself, its ring system and last, but not least, its moons.

## 2.1 Saturn

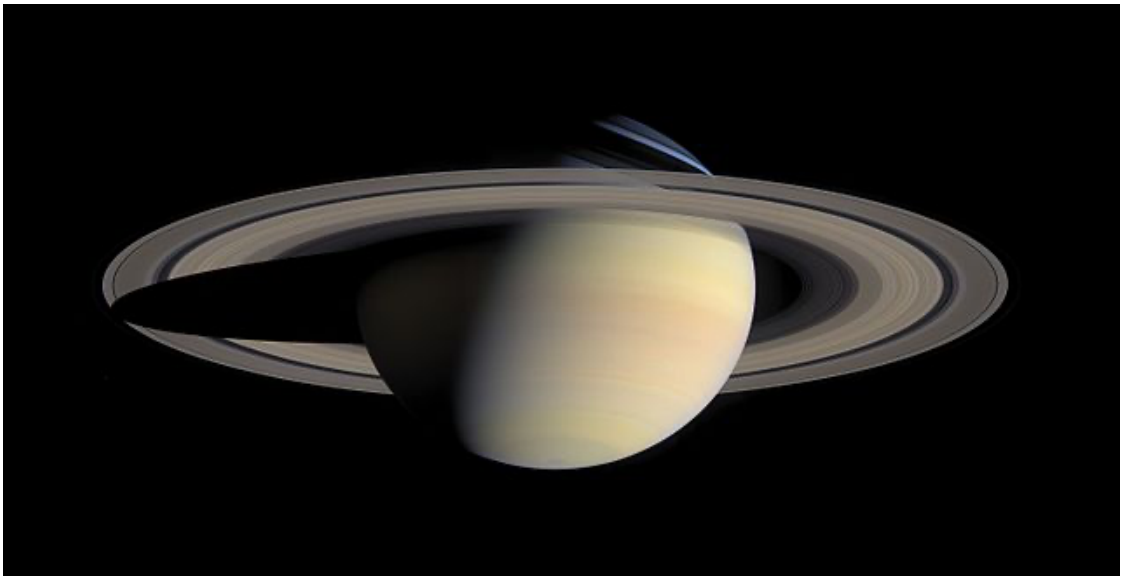

Fig. 3: Photo of Saturn, recorded by the Cassini-Huygens spacecraft in 2004. Image Credit: NASA/JPL/Space Science Insitute

Saturn is one of the gas giants and the sixth planet from the sun. It is second in size after Jupiter. Its mean density is lower than 1 g/cm$^3$ (Hide, 1966) and thus the planet is therefore, on average, even less dense than liquid water at standard conditions on Earth. Due to its fast rotation and fluid-like behavior, Saturn is an oblate spheroid. Therefore, its equatorial and polar radii differ by about 10%[a]. The atmosphere of Saturn contains mainly molecular Hydrogen, with a small proportion of Helium (~6%-wt; Conrath et al., 1984). There are also traces of Methane in the atmosphere and frozen Ammonia represents the main part of the visible clouds. Between Saturn's atmosphere and its rocky core, there is a deep mantle layer of metallic hydrogen overlain by an upper mantle of super critical molecular hydrogen (Courtin et al., 1984; Guillot, 1999; Fortney & Nettelmann, 2010). Similar to Jupiter's "Giant Red Spot", a

[a] https://nssdc.gsfc.nasa.gov/planetary/factsheet/saturnfact.html (NASA, 2019)

"Giant White Spot" has been observed in the Saturnian northern hemisphere, a giant whirlwind with a periodicity of ~30 years (Sánchez-Lavega & Battaner, 1987; Sánchez-Lavega, 1994; Sánchez-Lavega et al., 2012). During their passage in the 1980s, the Voyager probes discovered an almost perfectly hexagonal whirlwind at the north pole of Saturn (Godfrey, 1988). It was later confirmed by the Cassini-Huygens spacecraft (see Fig. 4).

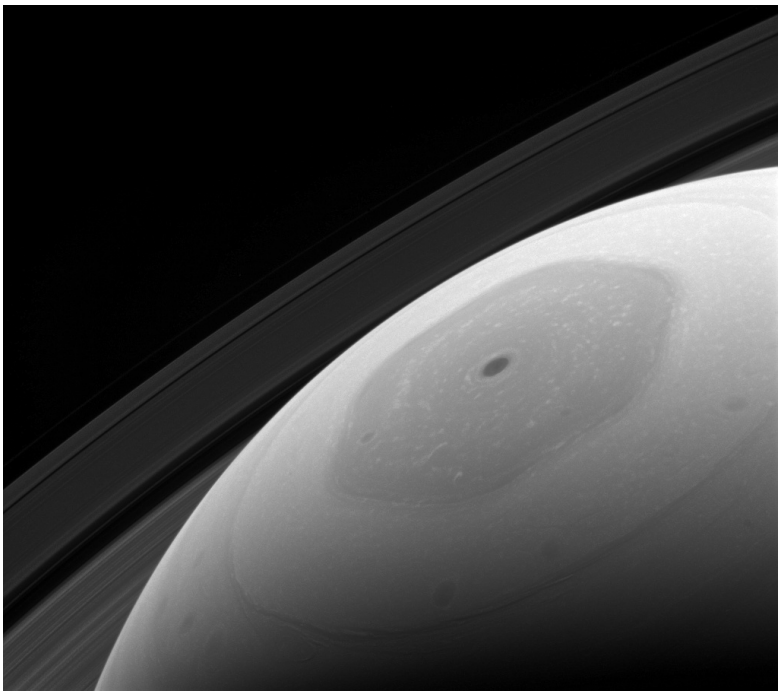

Fig. 4: The hexagonal whirlwind at Saturn's north pole, photographed by the Cassini-Huygens wide-angle camera in 2017. Image Credit: NASA/JPL/Space Science Insitute

The origin of this phenomenon is not completely understood and several hypotheses are currently pursued. For example, laboratory experiments indicate that speed differences between atmospheric winds could be the reason for this structure (Barbosa et al., 2010; Lakdawalla, 2010). Another theory suggests the cause to be shallow, localized meandering jet streams (Morales-Juberías et al., 2015).

## 2.2 Saturn's rings

Saturn is the only planet which possesses such a bright and massive ring system. While Uranus has a moderately bright ring system, those of Jupiter and Neptune are faint and dark, of only minor extent. Large telescopes and sophisticated observation techniques are required to observe them from Earth (de Pater et al., 1999; Meier, 1999). By contrast, Saturn's rings are not only vastly extended, but also show a bright inner region, that can even be seen from Earth with simple binoculars.

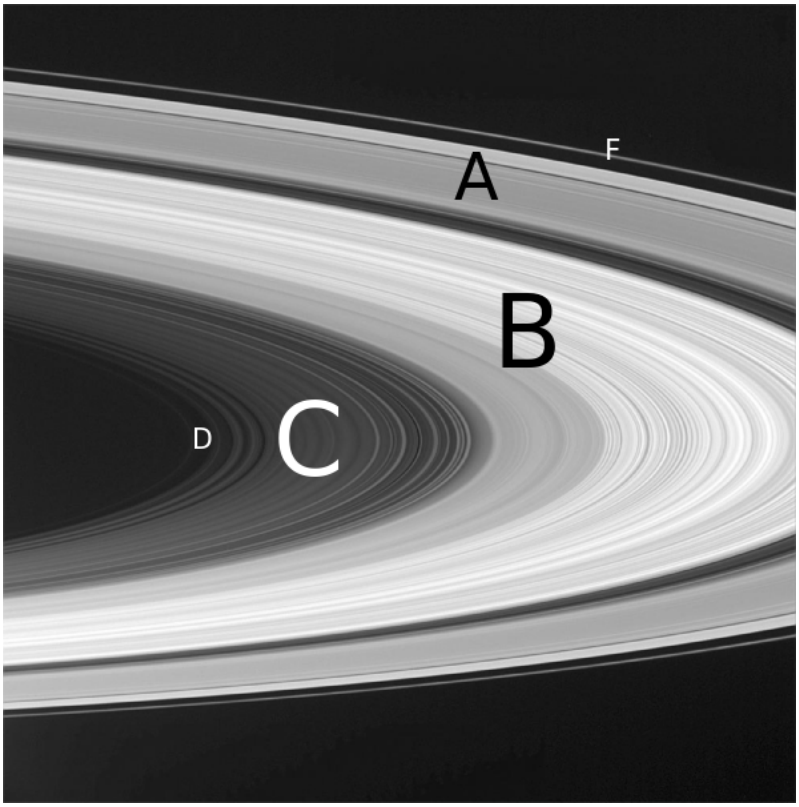


Fig. 5: Close view of the inner rings with corresponding letters. Credits: NASA/JPL/Space Science Institute

Saturn's bright inner rings, the so-called "main rings" or "main ring system", have been known for several hundred years. Galileo Galilei first observed them at the beginning of the 17th century but he believed them to be part of the planet (Whitehouse, 2009). In the 1650s, almost 50 years after Galileo's discovery, Christiaan Huygens correctly described them as an individual ring system, not touching the planet (Huygens, 1659). A few decades later, Giovanni Domenico Cassini found a gap in this ring system (Cassini, 1685), later known as the Cassini division. It divides the apparently single ring system into two separate parts, the A and B rings. In the middle of the 19th century, James Clerk Maxwell demonstrated theoretically that the rings must be formed by many individual grains orbiting Saturn (Maxwell, 1859), thus finally rejecting the idea of a solid structure. Maxwell's hypothesis was later proven by the observational work of James E. Keeler (Keeler, 1895). In the 19th and 20th centuries further rings were found, and named from A to G, according to the sequence of their discovery. Galileo's and Huygens' former single ring is represented today by the A and B rings (see Fig. 5). They form the most prominent part of the main ring system which also includes the rarefied sections C and D (see Fig. 5). The C ring was discovered in 1850 by William C. Bond and his son George P. Bond (Bond, 1850 & 1851). The first observations of the innermost D ring were reported by N. P. Barabashov and B. Semejkin and date back to 1933 (Barabashov & Semejkin, 1933). Its existence was eventually confirmed by Pierre Guérin in 1970 (Guérin, 1970). The

remaining three rings, E, F and G, are also rarefied and located outside the main ring system. The vast E-ring wasn't discovered until 1967, by Walter Feibelman (Feibelman, 1967), while the smaller F- and the G-rings were discovered in 1979/80 by Pioneer 11 (Gehrels et al., 1980) and Voyager 1 (Smith et al., 1981), respectively. After its arrival in 2004, the Cassini-Huygens spacecraft revealed the existence of several previously unknown, much fainter rings, which turned out to be connected to the tiny moons Janus/Epimetheus, Methone, Anthe and Pallene (Cassini-Huygens Press Release 2006 & 2008; Hedman et al., 2009). In 2009, Spitzer infrared space telescope images showed another dark and diffuse ring along the orbit of the moon Phoebe (Verbiscer et al., 2009; Tamayo et al., 2014; Hamilton et al., 2015).

The rings are composed of varying mixtures of rocky and icy material, with grain sizes ranging from sub-µm to m. While the bright A-, B- and C-rings consist of pebbles and boulders mm to m in size (Zebker et al., 1985), the diffuse E and G rings are mainly made of much smaller grains (Dollfus & Brunier, 1982; Pang et al., 1984; Showalter et al., 1991; Nicholson et al., 1996).

## 2.3 The E-ring

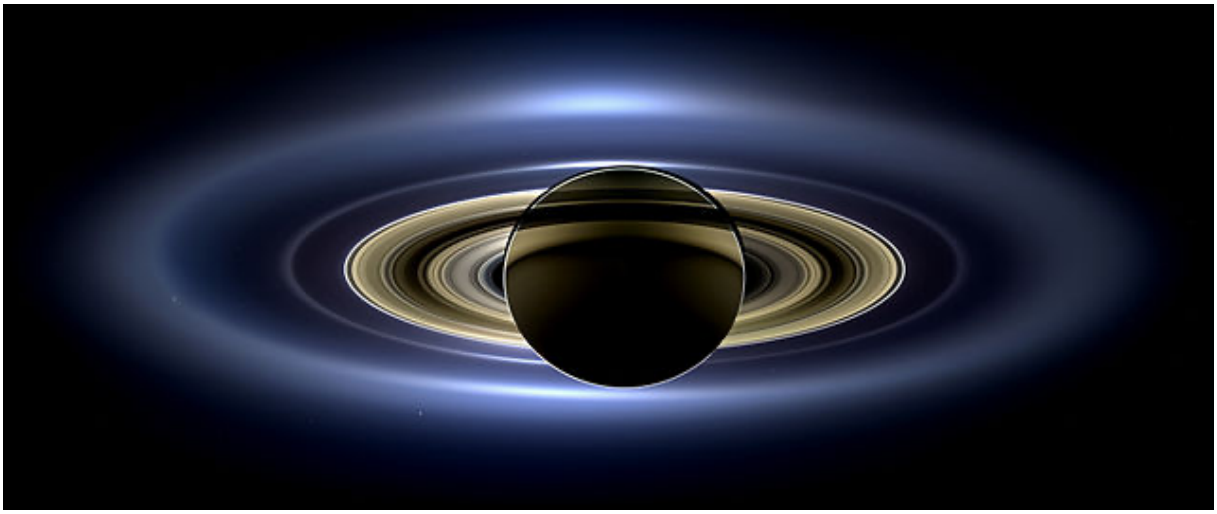

Fig. 6: Image of Saturn's rings at a phase angle of 180° in July 2013 (brightness exaggerated). The outermost ring visible in this picture represents the densest part of the large, diffuse E-ring. The diffuse G-ring is located right interior to the E-ring. Credits: NASA/JPL/Space Science Institute

The large and diffuse E-ring represents the major subject of this work and thus is introduced separately in more detail here. It is located outside the main rings, and the F- and G-rings (see Fig. 6). It is predominantly composed of µm to sub-µm water ice grains (Hillier et al., 2007a; Kempf et al., 2008), thought as early as 1981 (Baum et al., 1981) to originate mainly from the mid-sized ice moon Enceladus (Haff et al., 1983; Pang et al., 1984). This idea was based on the observation that the optically densest part of the ring coincides with the moon's orbit (see Fig. 7). Another, albeit minor, region of enhanced ring particle number density was

found in the vicinity of Tethys's orbit, suggesting it might be a possible secondary source (de Pater et al., 2004). After its arrival, the Cassini-Huygens spacecraft revealed a region of active cryo-volcanism at the south pole of Enceladus (Spahn et al., 2006a+b), the so-called plume, which supplies material to the E-ring by ejecting streams of water ice particles into space (see section "Enceladus", Fig. 11 A). More details about Enceladus and its cryovolcanic plume will be presented later in a separate section.

Fig. 7: Backlight-image of Enceladus embedded within the dense part of the E-Ring, recorded by Cassini's Imaging Space Subsystem (ISS) - Wide Angle. Credits: NASA/JPL/Space Science Institute

However, Cassini found that the E-ring actually reaches far beyond Tethys' orbit. The E-ring seems to extend from the F-ring (Linti 2018, Buratti et al., 2019) to at least the orbit of Rhea (Srama et al., 2011). Data from the Cosmic Dust Analyzer (CDA) instrument, onboard Cassini-Huygens spacecraft, even indicate the presence of ice particles near Titan's orbit (Srama et al., 2006 & 2011), which could still belong to the E-ring. The exact radial extent of the E-ring is still under debate and the results of this work will hopefully help to solve this issue.

Unlike the other rings, the E-ring also exhibits an appreciable vertical dimension. Earth-bound infrared observations found a vertical full-width-half-maximum (FWHM) of approximately 9000 km between Mimas and Enceladus (de Pater et al., 2004). At Enceladus' orbital distance the vertical FWHM is around 8000 km, which increases to approximately 40000 km at 8 $R_S$[a] near Rhea (Kempf et al., 2008). Similar values were found from Cassini Imaging Science Subsystem (ISS) data (Hedman et al., 2012) and Cassini's Radio and Plasma

[a] 1 $R_S$ = 60330km (Kempf et al., 2008)

Wave Science (RPWS; Ye et al., 2016). For comparison, values measured by the High-Rate-Detector (HRD) subunit of Cassini's cosmic dust analyzer instrument (Kempf et al., 2008), an in-situ dust counter, were approximately half the size. The authors explain this discrepancy by the fact that the particles observed in the observational data cover a size range of 0.3 to 3 µm, while the HRD was only sensitive to particles of approximately 1 µm and larger. These vertical ring extents can, however, only be explained by many dust particles on inclined orbits.

Due to the small grain sizes, low spatial density and the large distance to Earth, terrestrial E-ring observations based on visible light are quite difficult. Observations from Earth are thus usually conducted using near-infrared light. There is much less disturbing light emitted by Saturn in this wavelength region because of the methane present in Saturn's upper atmosphere. It has absorption bands at around 2.26 µm and thus absorbs incoming infrared light, preventing disturbing reflection/re-emission (de Pater et al., 1996). Alternatively, observations at visible wavelengths can be conducted by spacecraft, for example as done by Cassini-Huygens. Here, optimal results were produced when the spacecraft was at opposition to the Sun (w.r.t. Saturn), thus within the shadows of Saturn's nightside, and the rings had a significant tilt w.r.t. the solar ecliptic. Saturn was thus blocking the direct sunlight and the instruments, onboard the spacecraft, were able observe the faint light scattered from the rarefied E-ring (see Fig. 6). The E-ring's "blurred" shape is the result of the wide spread of orbital parameters of its icy dust particles. As mentioned before, the densest part of the ring is located along and near Enceladus' orbit ($r_E = 3.95\ R_S$[a]). This represents the region where the pericenters of many dust particle orbits accumulate, and many particle trajectories cross Saturn's equatorial plane. At the outer edges of the ring the opposite effect occurs. Since the available spatial volume there is much larger compared to the inner sections, the same number of dust particles distribute over a much larger region and the particle number density drops appreciably.

The E-ring needs constant replenishment of dust particles because particle migration, plasma sputtering, sublimation and other dynamical sinks continuously reduce the number of dust particles. The particles migrate outwards through the E-ring during their lifetime, due to plasma drag forces (Morfill et al., 1983; Havnes et al., 1992; Dikarev, 1999). Meanwhile, the plasma also sputters the dust particles (Jurac et al., 2001a+b, Johnson et al., 2008), eroding them, which limits their lifetimes to a few centuries at most (Horányi et al., 2008). Due to dynamical interaction with the moons, particles are removed as well, either by collision with the main rings or with one of the moons. However, when the surviving particles finally reach

[a] Kempf et al., 2008

Titan's orbit, they're either captured by the large moon or just dissipate into interplanetary space. Some of the dust particles are already smaller than 100 nm before colliding or reaching Titan's orbit. At these sizes they become susceptible to electro-magnetic forces, caused by the interaction of particle surface charges and the Saturnian magnetosphere, that in this size regime becomes dominant over Saturn's gravitation. When reaching sizes in the order of 10 nm these so-called stream particles are rapidly accelerated (>100 km/s) and leave the Saturn system (Horányi et al., 2000; Kempf et al., 2005a+b; Hsu et al., 2011a+b, 2012[a] & 2015).

## 2.4 Saturn's moons

At the time of writing, 82 moons are known to orbit Saturn . They possess a wide range of sizes, shapes and orbital parameters. At one size extreme is the planet-like moon Titan, with a radius of approximately 2575 km (Iess et al., 2010) and a stable, dense atmosphere. At the other extreme are dozens of m- to km-sized, irregularly shaped moons, moving on inclined and eccentric trajectories, some of which are even moving on retrograde orbits around Saturn (Denk & Mottola, 2019). The basic composition of the moons is a mixture of ice, mostly $H_2O$, and rock. Five larger moons are embedded within the E-ring (see Fig. 8): Mimas, Enceladus, Tethys, Dione and Rhea.

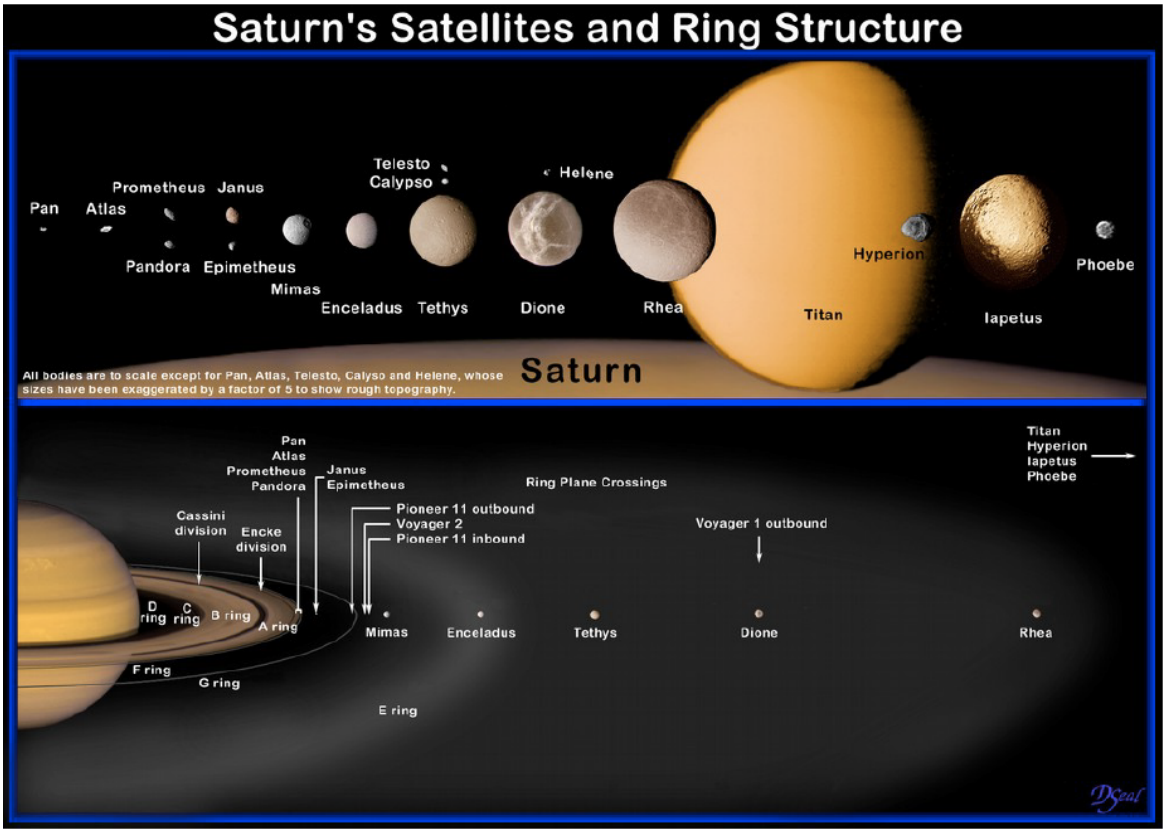


Fig. 8: Comparison of the size (top) and the distance to Saturn (bottom) of Saturn's satellites. The E-Ring spans from around Mimas to Titan. Image Credit: David Seal

[a] Part of Mann et al. (2012)

They’re approximately spherical, exhibit a relatively high albedo, low density and a differentiated interior structure, typically with a rocky core surrounded by a crust of mostly $H_2O$ ice (Spencer & Nimmo, 2013).

## 2.5 Enceladus

Enceladus plays an essential role for the E-ring and thus will be described in more detail. As mentioned before, Earth-bound observations, preceding the arrival of Cassini-Huygens, had revealed that the moon’s orbit is co-located with the densest part of the E-Ring (see Fig. 7). The Voyager Saturn flybys also provided further details about the surface properties of Enceladus, with, for example, different surface types discovered (Smith et al., 1982):

- Cratered, most likely old
- Smooth and apparently young
- Geologically stressed, full of cracks and ridges, presumably very young

Enceladus’ surface also has an extremely high Bond albedo of 0.85 (0.77 leading vs 0.93 trailing hemisphere; Pitman et al., 2010), which means it reflects 85 % of the incoming sunlight, a value unmatched in the solar system.

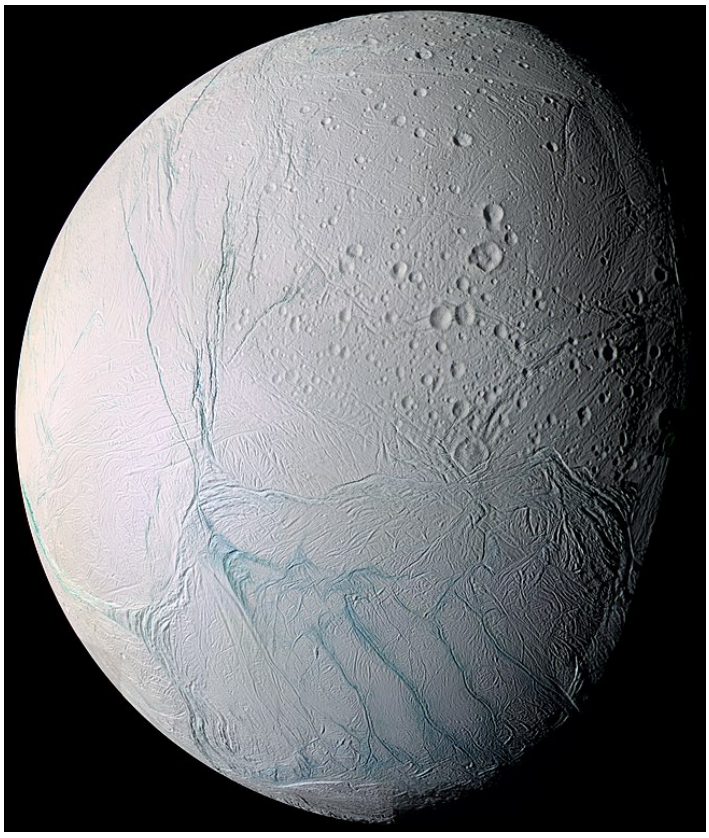

Fig. 9: Cassini-Huygens image mosaic of Enceladus and its south polar terrain. Thanks to the false color scheme the Tiger stripes are easy to recognize. Image Credit: NASA/JPL/Space Science Institute

In 2005, Cassini-Huygens recorded images of previously unseen regions of Enceladus. These pictures uncovered a region at the south pole with several parallel, giant cracks and embedded active cryovolcanoes (Porco et al., 2006; see Fig. 10), the so-called Tiger stripes. The cryovolcanoes continuously eject water vapor (Dougherty et al., 2006; Waite et al., 2006; Hansen et al., 2006) and water ice dust particles (Spahn et al., 2006a+b; Hillier et al., 2007a; Schmidt et al., 2008) into space from which much falls back as snow, covering the moon's surface (Kempf et al., 2010). This freshly fallen snow is ultimately responsible for the high reflectivity and young and smooth terrains. But some of the ejected ice particles do not fall back. They're able to exit the gravitational influence of Enceladus but not that of Saturn. Thus, Enceladus formed the E-ring (Spahn et al., 2006a+b; Schmidt et al., 2008) and continuously refreshes it (Kempf et al., 2010).

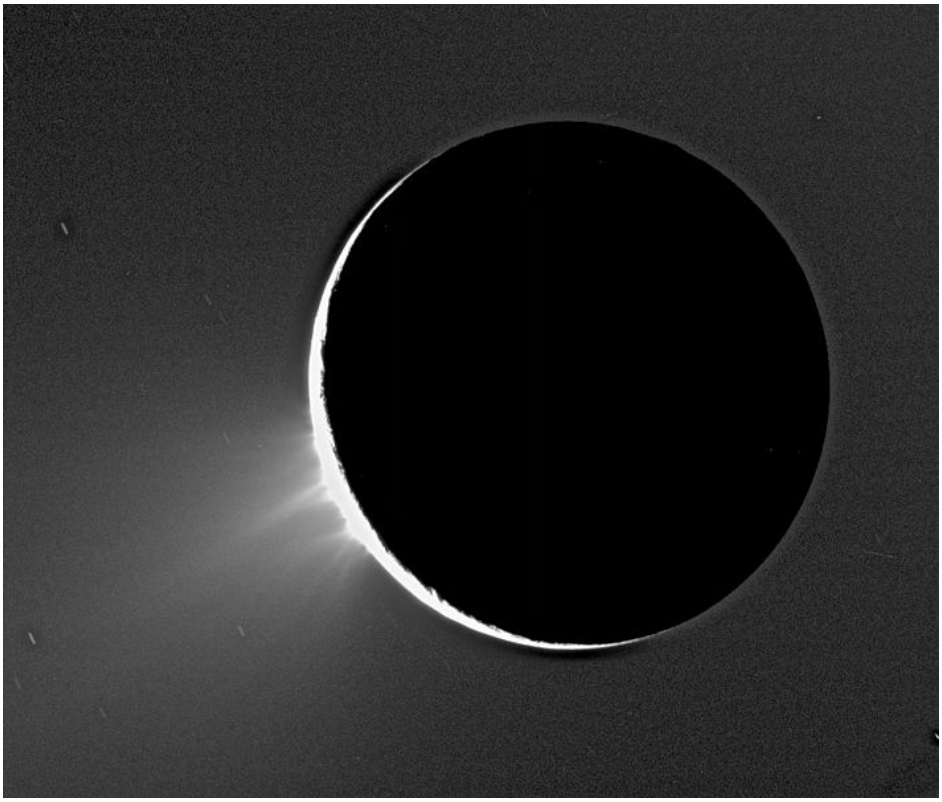

Fig. 10: Enceladus' night side, its active cryovolcanoes and the ejected dust stream, recorded by Cassini's Imaging Science Subsystem – Narrow Angle. Image Credit: NASA/JPL/Space Science Institute.

The Tiger stripes also show significantly increased thermal radiation in comparison with the rest of the moon's surface (Spencer et al., 2006; see Fig. 11). The discovery of salts in the ejected ice grains (Postberg et al., 2009a and 2011a) strongly indicated the presence of a liquid ocean below Enceladus' surface, in contact with its rocky core. Furthermore, the identification of nanophase silica particles in E ring grains also indicated ongoing hydrothermal activity at the core-ocean boundary (Hsu et al., 2015). Although the presence of organic material within

the icy dust particles had been known since 2008 (Postberg et al. 2008), later discoveries enabled different organic compounds to be distinguished. They range from simple volatiles to highly complex, polymer-like structures and include nitrogen- and oxygen-bearing as well as unsaturated, aromatic functional groups (Postberg et al., 2018a & Khawaja et al., 2019). Thus, there is thought to be significant thermal activity and chemistry going on within, or interacting with, the subsurface ocean, perhaps providing appropriate conditions for prebiotic chemistry or even the formation and conservation of life (McKay et al., 2004 & 2018). This has made Enceladus of great interest for astrobiological research.

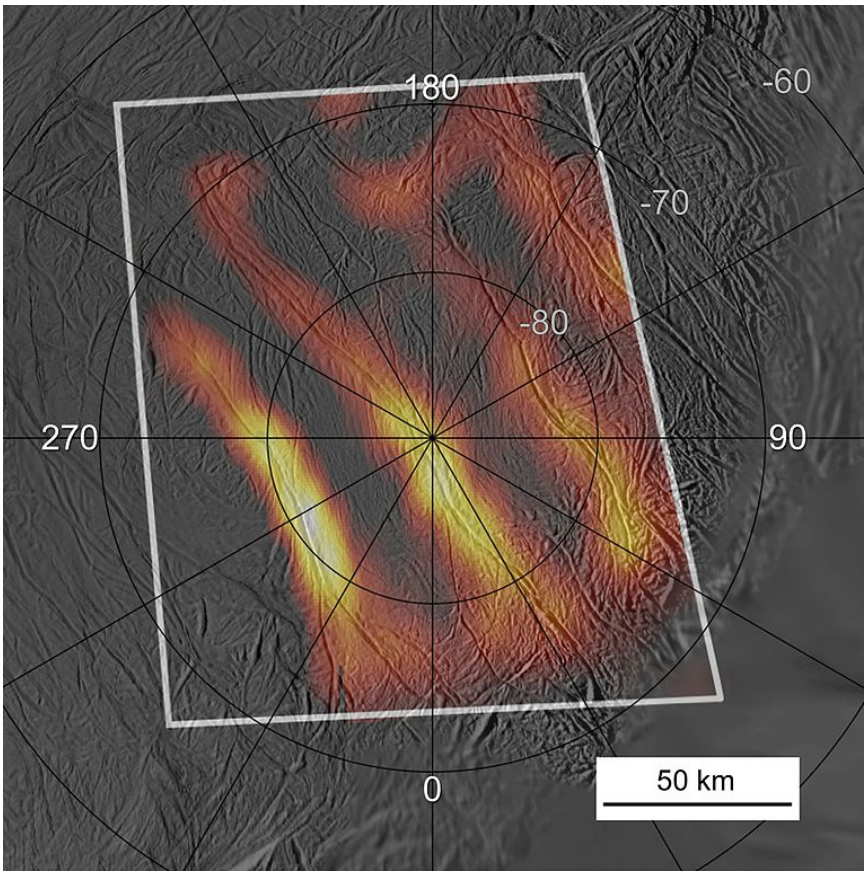


Fig. 11: Thermal emission map from the Tiger stripes at Enceladus' south polar terrain. Image Credit: NASA/JPL/GSFC/SwRI/SSI

# 3. The Cassini-Huygens Spacecraft

This flagship mission was a collaboration between NASA, ESA and the ASI, with the primary goal of examining the Saturnian system in detail. It was named after the astronomers Giovanni Domenico Cassini and Christian Huygens. Launched in 1997, it reached Saturn in 2004 after several swing-by maneuvers (see Fig. 12). The end of the mission was on the 15th September 2017. Having been placed on a collision course with Saturn, Cassini burned up in its atmosphere.

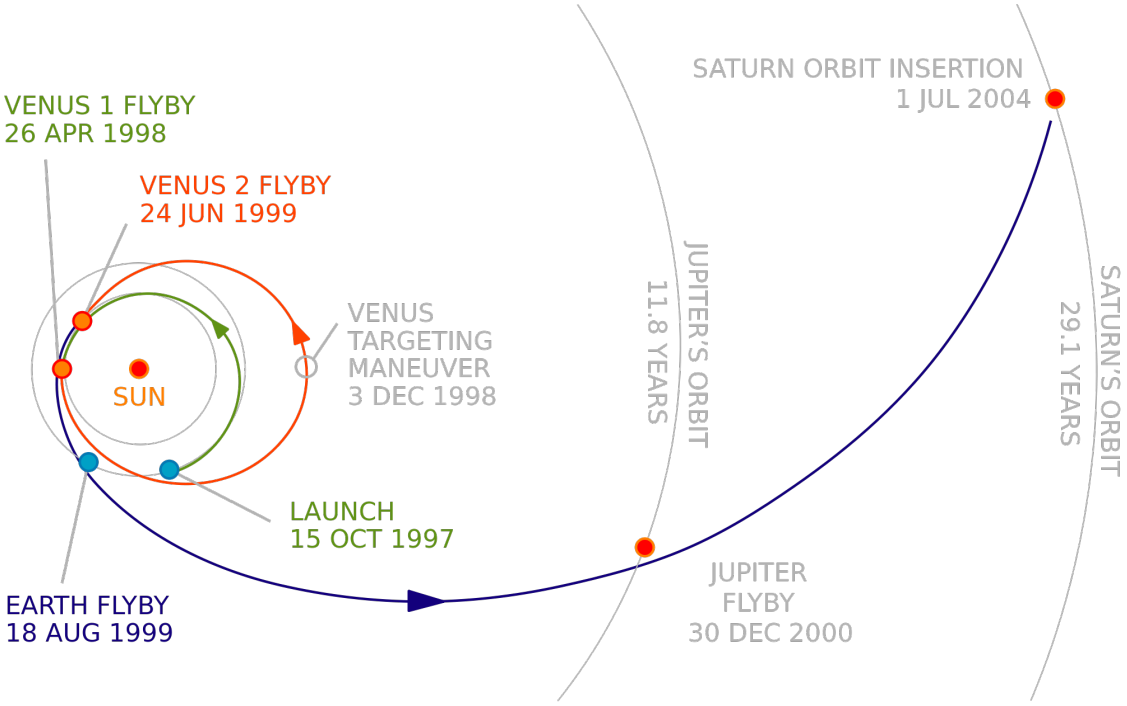


Fig. 12: Flight path of the Cassini-Huygens spacecraft with the respective swing-by maneuvers. Image Credit: NASA/JPL

The mission's main objectives were the investigation of Titan's atmosphere and surface, Saturn's atmosphere and magnetosphere, its ring system and the mid-sized icy moons. For this task the spacecraft was equipped with a collection of specialized instruments (see Fig. 13):

- CAPS: Cassini Plasma Spectrometer
- CIRS: Composite Infrared Spectrometer
- CDA: Cosmic Dust Analyzer
- INMS: Ion & Neutral Mass Spectrometer
- ISS: Imaging Science Subsystem
- MAG: Dual Technique Magnetometer
- MIMI: Magnetic Imaging Instrument
- RPWS: Radio & Plasma Wave Science
- RSS: Radio Science Instrument

- UVIS: Ultraviolet Imaging Spectrograph
- VIMS: Visible and Infrared Mapping Spectrometer

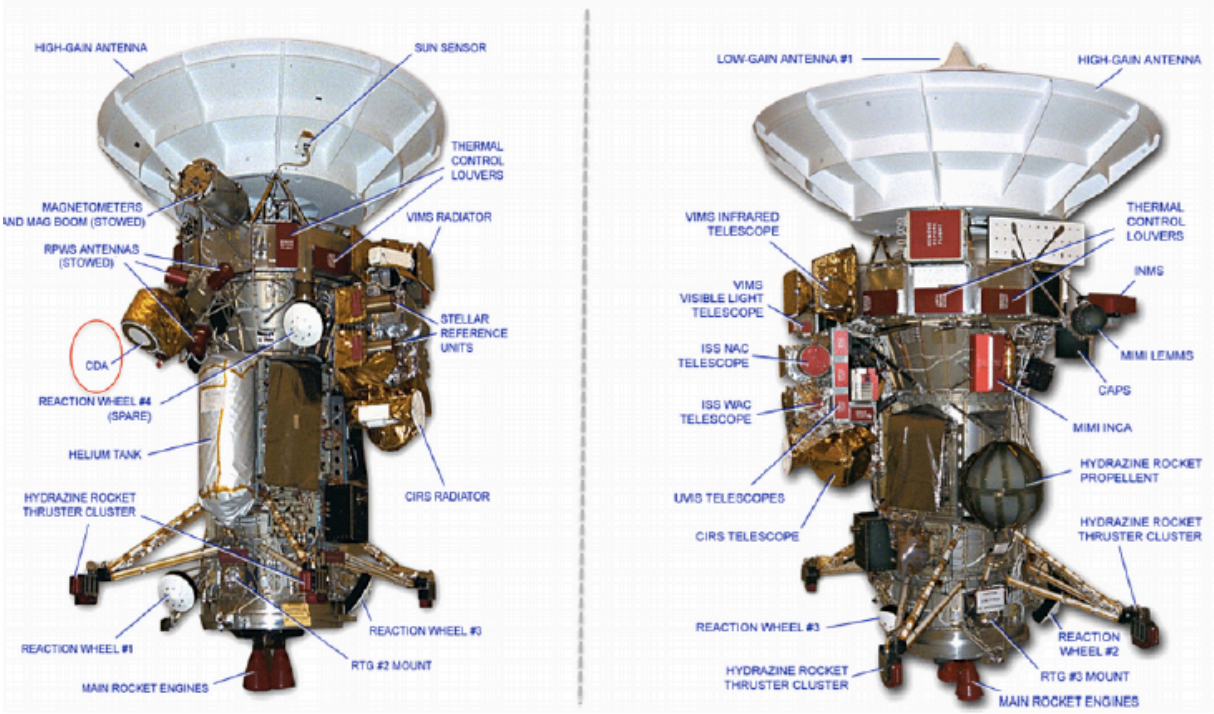


Fig. 13: Schematic of the spacecraft showing the position of each instrument, except the Huygens lander. Image Credit: NASA

As well as the aforementioned instruments, Cassini also carried the Huygens lander. The lander was dispatched to Titan to study directly its atmosphere (Tomasko et al., 2005) and surface (see Fig. 14). It returned data for several hours after landing before its batteries ran flat.

Fig. 14: Image of Titan's surface recorded at the Huygens landing site. Image Credit: ESA/NASA/JPL/University of Arizona; processed by Andrey Pivovarov

On Cassini, the Cosmic Dust Analyzer (CDA) instrument is of special interest, because it provided the major part of the data for this work. It was designed for the in-situ analysis of cosmic dust particles and had several subunits, designed to e.g. record dust fluxes or analyze the physical & chemical properties of individual particles. It will be described in detail in main chapter B.

# 4. Objectives of this work

The first main objective of this work was to produce a comprehensive picture of the µm to sub-µm ice particles found in the E-Ring. This includes two steps:

1. Analysis and compositional classification of thousands of individual impact ionization time-of-flight mass spectra, recorded by the Cosmic Dust Analyzer (CDA) instrument, onboard the Cassini-Huygens spacecraft.
2. Conduct a compositional mapping of the E-ring by connecting the aforementioned, individual, classifications to instrument metadata. The latter includes parameters provided by the instrument or the spacecraft, e.g. particle impact speed or impact strength and most important, the spacecraft position within the E-ring at the moment of detection.

To provide more complete spatial coverage, spectra from both planar, radial passages along the equatorial ring plane as well as highly inclined, steep ring plane crossings were chosen for this study.

Another auxiliary objective was to determine the impact of different compositions, e.g. organic substances or salts, onto the ion yield of ice particles after impact ionization. This is done using a laboratory instrument, which works on the principle of Laser-Induced Liquid Beam Ion Desorption (LILBID). Combined with a time-of-flight (tof) mass spectrometer, this equipment is capable of producing analogue mass spectra of those created by impact ionization of microscopic water ice particles in space. The results enable more precise determination of particle sizes from ion yields (QI amplitude) in CDA data.

# B. Instruments and methods

In this chapter the instruments, data and methods used for this thesis will be described. The first section will introduce Cassini's Cosmic Dust Analyzer instrument and its working principles. There will be a detailed focus on the Chemical Analyzer subsystem and the resulting data from its in situ compositional dust measurements, which represent the predominant part of this work. The second section provides an overview of the laser desorption laboratory experiments conducted to produce analogue measurements of the organic-bearing, micron-sized water ice particles sampled by the Cosmic Dust Analyzer.

## 1. The Cosmic Dust Analyzer instrument

The Cosmic Dust Analyzer, henceforth referred to as CDA (see Fig. 15), was one of the instruments carried by the Cassini-Huygens mission to Saturn. It was designed for the in-situ detection and analysis of µm to sub-µm size dust grains, sampled during Cassini's flight through the solar system and its orbits around Saturn. This section will give a brief summary of its construction, the applied physical mechanisms, results preceding this thesis and finally the methods applied to produce the results presented in this work. All stated technical parameters and information about the instrument in this chapter are based on Srama et al. (2004), if not explicitly mentioned otherwise.

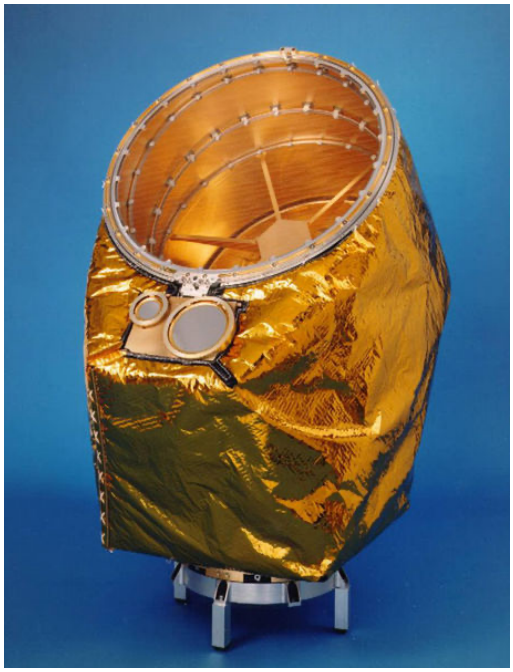

Fig. 15: Image of the Cosmic Dust Analyzer. Image Credit: NASA/JPL

## 1.1 Instrument setting and underlying mechanisms

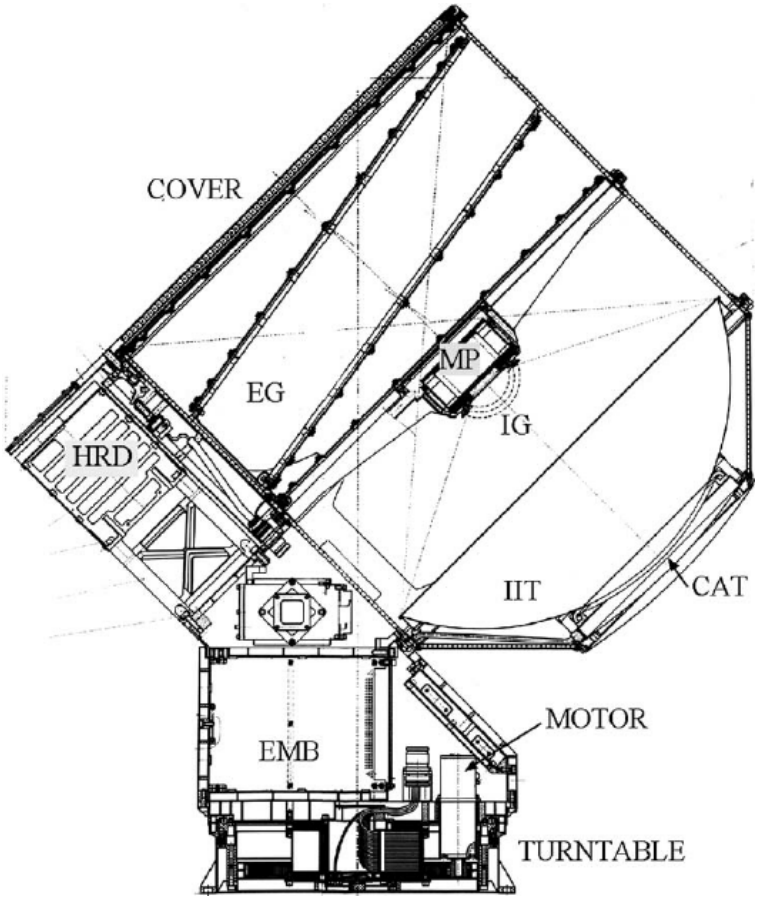


Fig. 16: Scheme of the CDA, showing: the High-Rate-Detector (HRD), the Entrance Grids (EG), the Multiplier (MP), the Ion Grids (IG), the large Gold target of the Impact Ionization Target (IIT), the small Rhodium target of the Chemical Analyzer Target (CAT) and the Electronics Main Box (EMB). Adapted from Srama et al. (2004).

The interface of CDA to the spacecraft included a turntable, which allowed the instrument to be rotated by up to 270° around the mounting vector, to maintain wide sky coverage. Such a measure was necessary as the originally planned rotation platform for the Cassini spacecraft was cancelled during the descoping phase and thus orientation with the help of the spacecraft was highly limited. This limitation was due to the three-axis stabilization and limited rotation speed of the spacecraft, together with the varying pointing priorities of the other instruments.

There are two detector units integrated in the CDA, the High-Rate Detector (HRD) and the Dust Analyzer (DA). The HRD featured two polyvinylidene fluoride (PVDF) sensors and was designed to measure dust fluxes, with particular focus on the high fluxes expected to be found during ring plane crossings of the E-ring. HRD data were not used for this work, so a

detailed explanation of its working principle will not be given and instead Srama et al. (2004) should be referred to for further details. The Dust Analyzer (DA) consists of the following components (Fig. 16 and Fig. 17):

- the Entrance Grids (EG)
- the Impact Ionization Target (IIT)
- the Chemical Analyzer Target (CAT)
- the Chemical Analyzer Grid (CAG)
- the Ion Grids (IG)
- the Multiplier (MP)

Charge sensitive amplifiers were connected to each component to record their signals (see Fig. 17), except the multiplier, which is itself a recording amplifier itself.

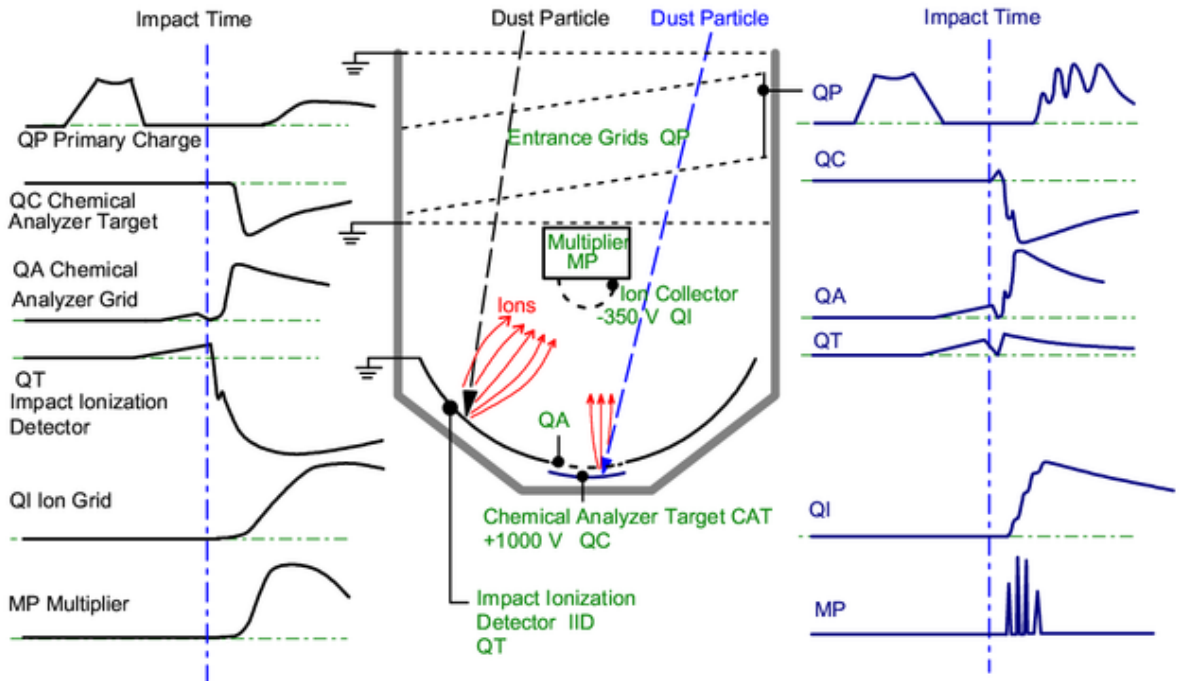


Fig. 17: Schematic of the working principle of the CDA during a particle impact. The different amplifier channel signals are shown for an impact onto the large outer, ring-shaped Gold target (IIT) and the small Rhodium target (CAT) at the center. Adapted from Srama et al. (2004).

The EG consisted of four grids placed across the aperture of the DA, capable of measuring the surface charges carried by incoming dust particles. Its signals were recorded via the QP channel (see Fig. 17). The duration of this signal, combined with the known distance between the first and the fourth grid (see Fig. 17) could be used to calculate the particle's velocity component in the direction of the instrument's boresight (Auer et al., 2002). The slightly inclined geometry of the inner two grids of the EG resulted in an asymmetric signal that provided information about the particle's direction in one plane.

After passing the EG, a particle hits either the big IIT (d = 41 cm) or the smaller CAT (d = 16 cm; see Fig. 17). The ring-shaped IIT, which represented the basis of the Impact-Ionization-Detector (IID), was coated in gold and covered a field of view (FOV) of 45° half angle, with respect to the instrument's boresight (BS). The CAT was located in the center of the IIT, was made of Rhodium and covered a FOV of 28° half angle from the BS. To achieve the capability to analyze an impacting particle's chemical composition, it had an additional CuBe grid 3 mm in front of it, the Chemical Analyzer Grid (CAG). Together the CAT and CAG – along with the ion detector and near-drift region – formed the chemical analyzer (CA) subsystem of CDA's dust analyzer. The exact working principle of the CA will be described later in this chapter.

Both IID and CA worked on the principle of impact ionization. If a dust grain hits the target at a velocity of typically ≳2 km/s, the so-called hypervelocity regime, the particle together with some target material evaporates and partially ionizes (Friichtenicht et al., 1963 & 1971) The generated impact cloud consists of various components from the particle and target material, such as ions/molecular fragments, neutral molecules, atoms and electrons, as well as macroscopic ejecta. The degree of ionization is mostly dependent of the particle's kinetic energy and thus its mass and velocity (Friichtenicht et al., 1963 & 1971). The ions can then be extracted via electric fields and eventually analyzed, while neutrals are lost.

As previously mentioned, there was a crucial difference between the IID and the CA, the CAG. While the IIT itself was grounded (see Fig. 17) the CAT was held at +1000V and instead the CAG was grounded (see Fig. 18). Thus, ions generated on the IIT were only subject to the weak electrostatic field generated by the IG (and subsequently the MP), which resulted in only a minor acceleration due to the relatively large distance to the target ($a \sim E = \frac{U}{d}$). The combination of the small distance between the CAT and CAG (d ≈ 3 mm) and the relatively large potential difference (+1000V) resulted in a narrow, yet very strong field and thus in a high acceleration. After this initial acceleration field, the velocity gained by the ions is reciprocally proportional to the square root of their mass ($v \sim \frac{1}{\sqrt{m}}$), resulting in light cations gaining a higher velocity than heavier cations. The subsequent, relatively weak, acceleration produced by the IG field resulted in a quasi-field-free drift region of ~230 mm, compared to the region between CAT & CAG (~230 mm vs 3mm). The mass dependence on ion speed, results in different arrival times at the MP and therefore in the mass sensitive separation of the ions ($t \sim \frac{1}{v} \sim \sqrt{m}$), the working principle of a simple time-of-flight mass spectrometer (TOF-MS).


Fig. 18: Scheme of the Chemical Analyzer (CA), its parts and the attached voltages. The metal target is made of Rhodium. Adapted from Klenner et al. 2019

Due to the instrument field configuration, all negatively charged particles (anions/electrons) remain at, or are rapidly accelerated onto, the impact target. The positive ions (cations) are accelerated by the potential difference of 1000V between the acceleration grid (CAG) and the CAT, towards the IG and the MP, which are both set to negative voltages of approximately -350V and -2750V respectively (see Fig. 18). The charge signals recorded by the charge-sensitive amplifiers connected to the IIT (QT), the CAT (QC) and the central ion grid (QI) could be used later to estimate the mass and speed of the impacting particle, depending on its impact site.

The mass spectra, recorded by the multiplier (MP), show the various ion pulses as peaks, or mass lines, as a function of their detection/arrival times (see Fig. 19). As the raw spectra are recorded in time space, a calibration into mass space is required, to enable accurate analysis of the particle's chemical composition. This grew significantly in importance after the discovery of Enceladus' icy plume and the various unexpected compounds within E-ring ice grains (Postberg et al., 2009a, 2011a, 2018a; Khawaja et al., 2019). Hence, it represents an essential part of this work.

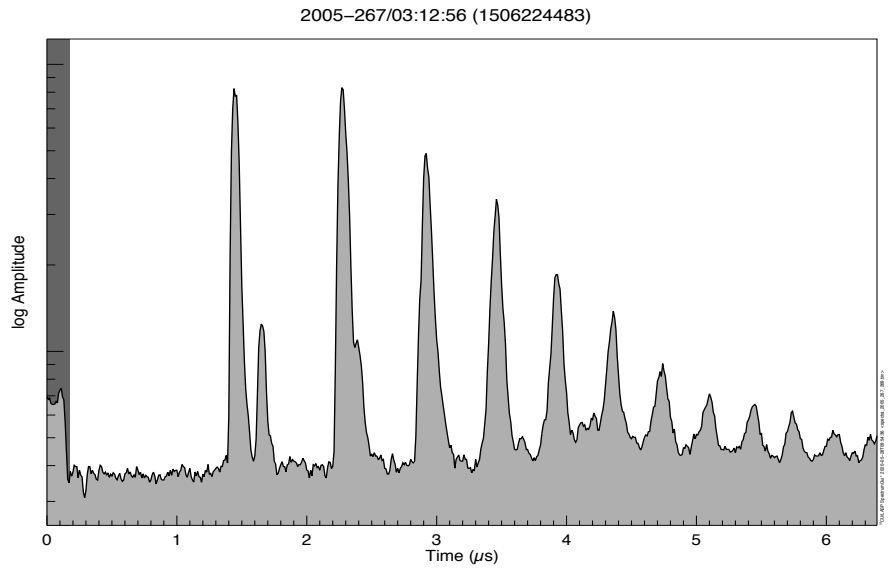


Fig. 19: Spectrum example recorded by the CDA in 2005.

Data recording, subsequent processing (e.g. wavelet compression) and storage of one event results in an effective instrument dead time of approximately 1s. This limited the CA's recording rate. To reduce the dead time and thus achieve better sampling rates for the CA, from time to time the QP channel (EG) was switched off. That was scientifically permissible because the EG and CA had non-overlapping sensitivity ranges (with respect to particle size/mass) and particles detected by one system usually did not produce useable signals for the other. Another way to reduce the instrument data rate and with that the dead time was to increase the MP shrink level. The shrink level determined the level of wavelet compression and therefore the required processing time, which was a major part of the dead time. A shrink value of "1" represented the lowest level of wavelet compression and hence highest spectrum resolution, however it also required the longest processing time. Higher shrink values ($\geq 2$) increased the compression level and thus reduced the processing time but resulted in decreasing spectrum resolution (by a factor given by the value). All spectral data used in this work exhibit a MP shrink value of 1.

Neither EG nor IID data are used in this thesis because they do not provide information about chemical composition or, as already mentioned, have non-overlapping sensitivity ranges. Therefore, all the following information refers to the CA subsystem, including QC, QI and MP.

## 1.2 Analysis of CA-spectra

Much work has already been invested in analyzing the records of the DA, especially in data recorded by the CA subsystem, e.g. Altobelli et al. (2016), Hillier et al. (2007a+b), Hsu et al. (2011a+b, 2015), Khawaja et al. (2019) and Postberg et al. (2006, 2008, 2009a, 2011, 2018a). The number of published results is growing continuously but much remains to be analyzed. In the following two sections the most important information both from published and still unpublished work, which is essential reading for the interpretation of spectral data of the CA discussed later, will be summarized. Following this, an overview of the chosen data and the method(s) used for the data analysis, will be given.

### 1.2.1 Trigger mechanisms and basic spectral properties

The wide range of particles masses/sizes and impact speeds means that not all particle impacts are strong enough to trigger the DA data recording. To trigger recording of the amplifier signals (QC, QI and MP) for the spectrum, the signal level at one channel had to exceed a specified threshold. The primary trigger channel was designed to be the QC signal channel of the target itself. As this trigger is synchronous with the particle impact, the zero point of the resulting spectra indicates almost exactly (bar minor electronics delays) the moment of impact and represents the zero mass. Therefore, this trigger method is called 'impact trigger' in the

following. But the other channels could serve also as triggers. In general, the most frequently activated trigger option, even more frequent than the impact trigger, was by the initial signal of the MP channel itself. Often the impact signal pulse on the target channel was not sufficient to trigger recording. In such cases the first sufficiently strong ion pulse reaching the MP, and exceeding its trigger threshold, was able to trigger recording. This resulted in a delayed start to spectrum recording and the resulting spectra did not start at zero mass but instead at a mass equivalent to that of the ions which triggered recording. This trigger method is referred to in the following as 'line trigger'. However, due to the aforementioned minor electronics delays the triggering ion signal was not recorded completely by the MP channel and the exact information about its signal amplitude was lost. There were further ways to trigger spectrum recording, for example thresholds being exceeded on the IG or the CAG, through ions generated by wall or CAG impacts, but the latter of these happened quite rarely and typically did not produce meaningful spectra. In autumn 2008 one amplifier of the QC channel was unexpectedly broken during a close flyby through Enceladus' plume, resulting in an extensive loss of sensitivity, and hence trigger capability, by two orders of magnitude (J. Simolka, personal communication, September 22, 2021). After this, other trigger techniques, in particular the line trigger, grew in importance.

When triggering occurs, the sample frequencies of the QC and QI channel amplifiers, which were previously working continuously at 0.375 MHz, were significantly increased, to 6 MHz, to achieve a high temporal resolution. Prior to triggering, the signals from both channels were recorded for 42.66 µs (16 samples at 0.375 MHz) to preserve pre-trigger signal slope information. After triggering, the QC channel was recorded for 32.66 µs (196 samples at 6 MHz) and the QI channel for 82.33 µs (494 samples at 6 MHz). The MP, being on standby otherwise, initially records at a sampling frequency of 100 MHz for 6.4µs (640 samples at 100 MHz). This part will be referred to as the spectrum. However, after this high-resolution period, the MP continues recording at a reduced sampling frequency of 10 MHz, and thus lower resolution. This lasts for 38.4 µs (384 samples at 10 MHz). Due to this length, it is capable of providing signals from ions with potentially much higher masses than the typical ~200 u limit provided by the high-resolution sampling (see Postberg et al., 2018a) and will be referred to as the late MP signal (see Fig. 20).

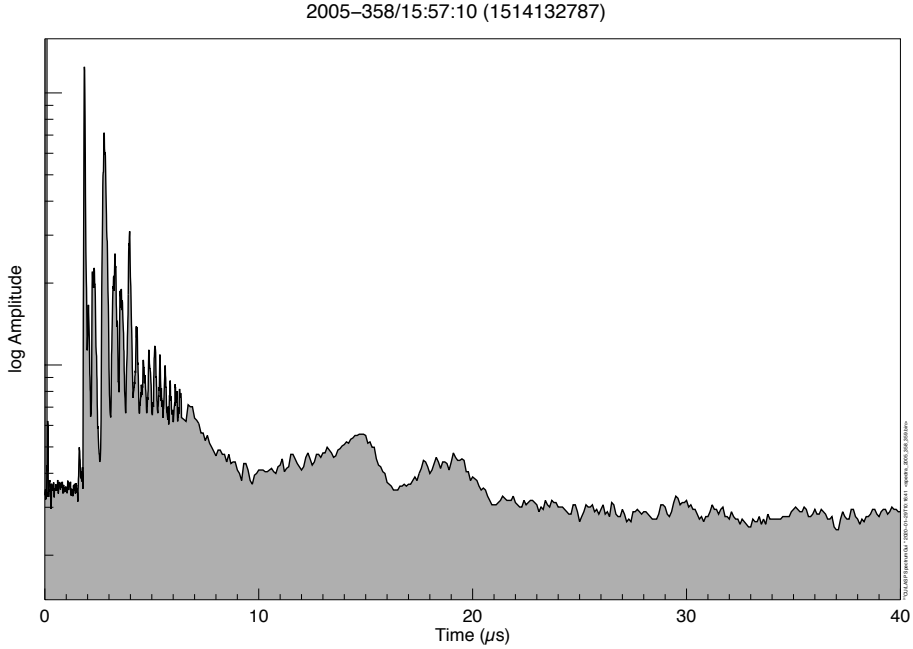


Fig. 20: Spectrum including late-MP signal. To the left the main part of the spectrum is visible.

### 1.2.2 Mass resolution and calibration of TOF mass spectra

CDA mass spectra are recorded with respect to the time after triggering, which is not necessarily the actual time of flight and depends on the specific trigger type. Therefore, it is necessary to individually mass calibrate each spectrum to correctly correlate MP signal, time of flight and corresponding ion mass. This allows the comparison of spectra with each other (adapted from Fiege, 2013; Khawaja, 2016 and references therein).

Considering a cation produced upon a CAT-impact, with a given mass "$m_{ion}$", charge "$q_{ion}$" and no initial speed; its kinetic energy and thus its speed "$v_{ion}$" originates exclusively from the electrostatic field ($U_{acc}$) between CAT and CAG:

$$\frac{1}{2} * m_{ion} * v_{ion}^2 = q_{ion} * U_{acc} \tag{2.1}$$

The arrival time "$t_{ion}$" at MP after impact (i.e. time of flight) of this ion can then be determined based on the length "d" of the drift path:

$$t_{ion} = \sqrt{\frac{d^2}{2*U_{acc}}} * \sqrt{\frac{m_{ion}}{q_{ion}}} \tag{2.2}$$

But one has to keep in mind, for CDA this represents just an approximation, since the region between CAG and IG has not completely been free of electrostatic fields. Depending on the trigger type, spectrum recording may or may not start at the impact time. Thus, the recorded

time "$t_{MP}$", which begins at triggering (i.e. the impact detection time), may deviate from "$t_{ion}$". This shift has to be taken into account and leads to the final relation between mass and time:

$$t_{MP} = b + a\sqrt{\frac{m_{ion}}{q_{ion}}} \tag{2.3}$$

Where "a" is the stretch parameter, a constant value defined by the instrument geometry and field strengths and "b" is the shift parameter, which represents the time shift between impact and the start of spectrum recording, and thus correlates with the actual trigger type. To determine "a" and "b" the following methods can be used:

- With a cross correlation to a theoretical template spectrum (Lavila, 2002)
- By fitting the detection times $t_1$ and $t_2$ of two assigned peaks to their respective masses $m_1$ and $m_2$ via the following equation (under the assumption of equal ion energies):

  $$t_2 - t_1 = a * (\sqrt{m_2} - \sqrt{m_1}) \tag{2.4}$$
- By doing a least square fit of "n" assigned lines $t = \{t_1, t_2, \ldots, t_n\}$ to the corresponding masses $m = \{m_1, m_2, \ldots, m_n\}$

Calibration of thousands of spectra recorded in space, showed that "a" lies approximately between 470 and 480 ns, with about 477 ns (J. K. Hillier, personal communication, April 19, 2021) being the theoretical value for the nominal instrument voltages and zero initial energy ions. While "a" can be considered to be a relatively constant value for a given set of e.g. voltages, the observable mass range is strongly affected by the shift parameter "b", which directly depends on the underlying trigger type. Impact triggered spectra ($0 \geq b > -0.3$ µs) represent near instantaneous recording after impact, and thus exhibit mass ranges of approximately 1 u to 180 u. Line triggered spectra thus represent delayed recording. As previously mentioned, these start spectrum recording with the first sufficiently strong ion pulse (e.g. $Na^+$), which takes a certain time to arrive at the MP after particle impact and ion formation (e.g. $Na^+$: m/z ≈ 23 u → TOF ≈ 2.3 µs). Because the instrument always records signals with respect to the trigger time, the recorded signals are stated on a shifted time scale, which now start at zero with the mass line of the triggering ion pulse. Ions arriving prior to the trigger are lost. The actual shift (shift parameter "b") is given approximately by the negative TOF value of the triggering ion pulse (e.g. $Na^+$: m/z ≈ 23 u → TOF ≈ 2.3 µs → b ≈ -2.3 µs). With the shifted lower mass limit, the line triggered spectra consequently also have a shifted higher mass limit as compared to impact triggered spectra (1 – 180 u vs. 23 – 330 u) because of the set recording time of 6.4 µs. Though losing faster and lighter ions in the lower mass range, whose signals were absent or too weak to trigger recording, there is an advantage in the

detection of heavier ions in the high mass range, which usually would not reach the MP in time to be recorded.

In reality ions have nonzero initial speeds after impact, with a broad speed distribution. Therefore, the actual time of flight "$t_{ion}$" and thus also the detection time "$t_{MP}$" of an ion species exhibits variations compared to the previous considerations. This issue results in broader peaks and asymmetric peak shapes in the spectra and consequently lowers the mass resolution significantly. Though there are measures known to neutralize, or reduce, these effects, such as a reflectron (Mamyrin et al., 1973) and improved ion focusing, they were not chosen for CDA in order to keep the instrument simple but robust (Srama et al., 2004). The mass resolution of a TOF mass spectrometer can be defined the following way:

$$\frac{m}{\Delta m} = \frac{t}{2*\Delta t} \tag{2.5}$$

Where "m" and "t" are the peak locations of a particular ion in mass- and time-space. and "Δm" and "Δt" are the FWHM[a] of the peak in the respective parameter space. Srama et al. (2004) showed that the CA achieved a mass-dependent mass resolution of approximately 20 to 50. But these values can decrease significantly for higher MP shrink values.

### 1.2.3 Known spectral types

From Cassini's Saturn tour, several types of dust particles have so far been identified from the large number of recorded spectra produced by the CA subsystem (see Table 1). Three main categories can be defined, which reflect the particles' basic materials:

- Water ice
- Mineral dust
- Stream particles

The first category, water ice, represents the most abundant composition found around Saturn. Its spectra are characterized by dominant clustering of water with cations in the form $X^+ [H_2O]_n$ ($n \geq 0$), where X is most frequently $H_3O$ but also regularly present are ions of $Na^+$ and $K^+$. Salts (e.g. NaCl or $Na_2CO_3$) and organics (e.g. amines or aldehydes) are the major constituents besides water ice in this category. This category is further subdivided into three different types, which are defined by the individual non-water compositions:

- Type 1 → salt- & organic-poor water ice
- Type 2 → organic enriched, salt poor water ice
- Type 3 → salt-rich water ice

[a] FWHM = Full Width at Half Maximum

Mineral dust spectra are dominated by the mass lines of $Mg^+$, $Ca^+$ and/or $Fe^+$ ions, with occasional minor indications of $Al^+$, $Si^+$ or $S^+$ and molecular species. These mass lines are accompanied by a collection of peaks characteristic of high-speed impacts: $H_{1-3}^+$, $C^+$, $O^+$ and $Rh^+$ (Postberg et al., 2009b; Fiege et al., 2014), and have a distinct lack of molecular peaks from water. Stream particles almost exclusively show these "high speed" mass lines, especially $C^+$ and $Rh^+$, with, in some cases, $Si^+$ present as a small spectral feature. In terms of the previous type classification of water ice, the mineral dust is also referred to as Type 4, while Stream particles form their own group and have no additional type designation (see Table 1). These known five types form the base to classify spectra from CDA spectral data. The respective spectral properties are summarized in Table 1 and Fig. 21 shows a selection of archetypal spectra for each type. It's important to notice that not all spectra present in the data exhibit the same "good" quality as shown in Fig. 21. Variations, even if tiny, in particle composition or mass, spectral trigger mechanism, and impact conditions, affect the quality and shape of a spectrum and lead to variations within each type.

Aside: Target contamination

More than one decade of flight around Saturn did not leave the instrument target untouched and contamination, not removeable by the decontamination heater, grew. From the start, there was carbon contamination in the Rhodium target. It was presumably caused by the diamond paste, used to polish the target surface on Earth prior to the mission launch, which got stuck in surface cracks. It is the main source for the observed $C^+$ signals in high-speed impact spectra. Furthermore, multiple deep dives through the Enceladus plume deposited detectable amounts of sodium and potassium on the target, at a ratio similar to that found in the grains. Compared to carbon, these elements are very easy to ionize but similarly hard to remove. Thus, Na and K contamination is believed to have frequently produced artificial, interfering signals in many spectra, which otherwise would not exhibit distinct amounts of these elements. The mineral dust spectra in particular suffer from this issue, because the mass lines of $Mg^+$ and $Ca^+$ are located next to $Na^+$ and $K^+$. Due to CDA's mass resolution, their peaks often merge. This makes it hard to distinguish their respective abundance. Moreover, this contamination impedes exact size estimations, especially for ice grains. There are ongoing efforts to disentangle the actual particle signal from the contamination in affected spectra.

Table 1: List of published compositional types of particles detected around Saturn. Jovian stream particles and other particles detected prior to Saturn apporach are not listed. Subtypes have not been considered because they've been part of the work of others (e.g. Khawaja et al., 2019 and Zou, 2021). The HMOC subtype of Type 2 represents an exception here, since it is used in this work, and the given mass lines were extracted from a separate reference (see below). Masses are for dominant isotope.

| Name & short description | Main Spectral Characteristics | Relevant Mass Lines | Presumed Origin | References |
|---|---|---|---|---|
| Type 1<br>Salt- & organic-poor water ice | Hydronium ion and its water clusters<br>$H_3O^+[H_2O]_n$<br>(n = 0, …, ≥10) | 19 u +<br>n*18 u | Enceladus frozen water vapor condensate | Hillier et al. (2007a); Postberg et al. (2008 & 2009a) |
| Type 2<br>organic enriched water ice | Low-mass molecular fragments of organic molecules, including N- & O-bearing compounds | 26 u – 31 u &<br>39 u – 45 u | Enceladus frozen water vapor condensate coated by a layer of adsorbed/condensed volatile organics | Postberg et al. (2008); Khawaja et al. (2019) |
| | **HMOC**:<br>Phenyl- & Benzyl-cations as well as high-mass organic cations | 77 u – 79 u<br>&<br>91 u – 93 u<br>+<br>n*(11-14 u) | Enceladus frozen water vapor condensate around a core of non-volatile, high-mass organics | Postberg et al. (2018a) |
| Type 3<br>salt-rich water ice | Sodium ions and clusters with its salts<br>e.g. $Na^+[NaOH]$, $Na^+[NaCl]$ or $Na^+[Na_2CO_3]$ | 23 u, 63 u, 81 u, 129 u | Frozen droplets of salty oceanic water from Enceladus | Postberg et al. (2009a & 2011a) |
| Type 4<br>Mineral dust | Ions of Magnesium, Aluminum, Silicon, Calcium & Iron | 24 u, 27 u, 28 u, 40 u, 56 u, 72 u or 88 u | Mg-Ca-Silicates, Fe-metal/oxides/sulfides from Interplanetary or Interstellar Dust | Postberg (2007); Fiege (2013); Altobelli et al. (2016) |
| Stream particles | Ions of Carbon, Silicon and Rhodium | 12 u, 28 u & 103 u | Nano silica inclusions in E-ring ice grains | Kempf et al. (2005a+b); Hsu et al. (2011a+b & 2015) |

Besides these five compositional types, there are two further "working" types, "?" and "noise", neither listed in Table 1 nor shown in Fig. 21 but used during the process of CDA spectra analysis and processing. Noise events/spectra are an obstacle when working with new, unprocessed data from the CDA flight spectra database and their removal is the major task during manual data processing. Noise events include spectra showing either no peaks at all or wide unidentifiable structures (such as those produced by IID impacts), which are not in agreement with any known peaks and are not considered to be a mass spectrum. Real spectra of unknown composition or other unassignable signatures, which clearly differ from noise and probably should be considered to be mass spectra, were collected in the category "Type ?" to save them for future analyses. Both types are not considered for evaluation.

The manual processing, calibration and noise removal of spectral data were conducted with the "Spectrum Analyzer" tool (version 5.011), developed by Sascha Kempf, based on IDL. Data export into the flexible HDF5 data format was done with the "Spectrum App" tool (version 1.6.5.1, build 150) also developed by Sascha Kempf.

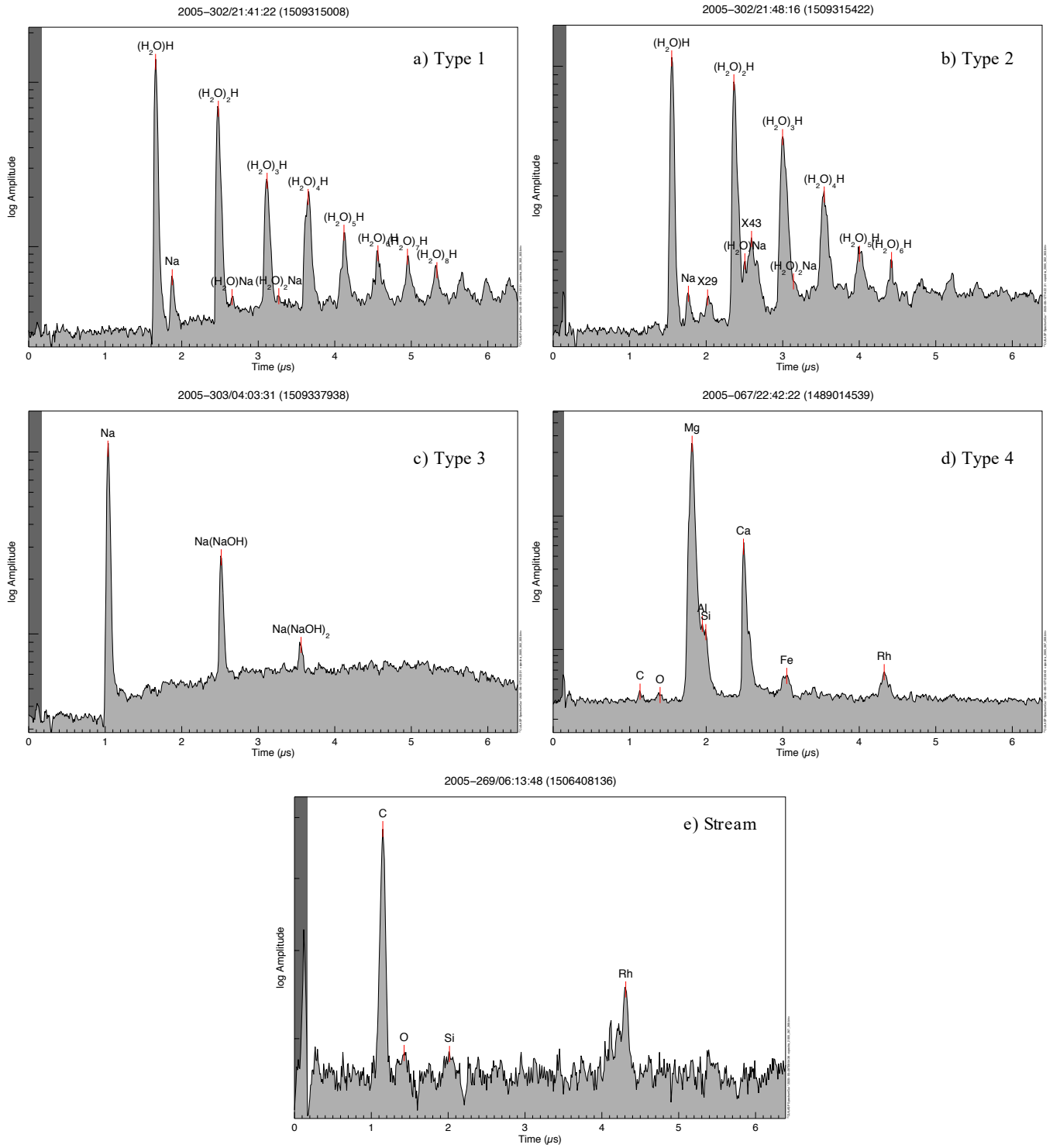


Fig. 21: (a-e) Example spectra for each of the compositional types listed in Table 1. Note, there are variations within each type category, so there are also numerous variants of spectral appearance in each category.

### 1.2.4 Particle size determination

In addition to a mass spectrum, another important parameter for characterizing a detected dust particle is its mass (and hence size). As there is no way to directly measure an impacting particle's mass, it is necessary to determine it in an indirect way. The amplitudes of the target (QC channel) and the ion grid signals (QI channel), which record the number of charges produced during impact, correlate with the impacting particle's mass but also depend on particle composition and impact speed. The EG would be the most accurate method to determine the impact speed but only works for particles with diameters of about 3 µm and above (Kempf et al., 2006). Besides that, there are currently three further ways and each of them is subject to certain restrictions:

- QC and/or QI channel rise time:
  The higher the impact speed, the faster the channel signal rises and thus the shorter the rise time is. In reality, this method only works fine for IIT impacts, because on one hand the QC channel went insensitive in late 2008 and on the other hand the additional, strong acceleration caused by the CAG compresses the ion stream too much for a precise QI channel rise time determination.
- Spectral appearance:
  The spectral appearance speed estimate relies on the speed dependent change in ion cluster size, presence of target material ions (e.g. $Rh^+$) and the appearance of ions with high ionization energies, e.g. $C^+$ or $O^+$ (Fiege, 2013; Fiege et al., 2014; Hillier et al., 2012 & 2018; Mocker et al., 2012; Postberg et al., 2009b) in spectra. This enables broad speed regimes (Klenner et al., 2019) for low to high impact speeds and also lower limits for very high impact speeds, to be assigned. However, this method requires a significant amount of manual processing of the spectra and is therefore only efficiently applicable to small data samples.
- Dynamical consideration:
  This technique assumes the impacting particle to have been moving on a circular, Keplerian orbit prior to meeting the spacecraft and hitting the target. This method is particularly useful for E ring dust, which can be assumed to be in prograde, low inclination orbits. Based on the known position and velocity of Cassini, it is possible to reconstruct the theoretical apparent velocity of such a particle and an impact speed vector can then be calculated, the so-called Kepler-RAM vector or just Dust-RAM vector. The length of this vector, the actual impact speed, is mainly dependent on the radial distance to Saturn but also reflects the characteristics of

Cassini's orbit, for example a high orbital eccentricity or inclination of the spacecraft results in higher Kepler-RAM speeds. The vector's orientation in space serves as the spatial reference of zero orbital eccentricity. For single impacts, the error in the derived impact speed might be considerable, due to deviations in the true orbital orientation, eccentricity and inclination of the particle. Under the assumption that the majority of particles are in near-circular orbits, the error in the derived modal impact velocity significantly decreases when looking at larger numbers of particle impacts, as done in this work. Therefore, given the small number of requirements, mainly Cassini's location and movement, both included in the state vector, this technique was used in this work when assessing the speeds and masses of E-ring ice grains.

After the speed is estimated, the particle mass can be calculated using the amplitude of the QI channel, based on the following formula (Srama, 2009):

$$log_{10}(m) = -4.15 + 0.558 * log_{10}(QI) - 5.59 * log_{10}(v) - 0.144 * log_{10}(QI) * log_{10}(v) \quad (2.6)$$

"QI" means the aforementioned QI channel amplitude in [C], "v" is the impact speed in [km/s] and "m" is the particle equivalent mass in [kg]. It's important to point out here that this formula was established using iron particles in a Van de Graaff accelerator experiment and not for water ice particles. Hence, a systematic bias is very likely but currently there is neither a way to quantify it nor to avoid it.

Making the assumption of spherical particles with radius "r" and constant particle density "ρ", the particle equivalent radius can be calculated via:

$$V\ [m^3] = \frac{m\ [kg]}{\rho\ [\frac{kg}{m^3}]} = \frac{4}{3}\pi\ (r\ [m])^3 \quad (2.7)$$

This formula can be rearranged for "r" in microns:

$$r\ [\mu m] = 10^6 \cdot \sqrt[3]{\frac{3m}{4\rho\pi}} \quad (2.8)$$

Here it's important to briefly mention the total sensitivity range of the QI amplitude channel, from 1-2 fC at the lower limit to 2-3 pC (1 pC = $10^3$ fC, 1 fC = $10^{-15}$ C) at the upper end. The lower limit results from the necessary, minimal number of ions required to produce spectral signatures in the instrument, as well as e.g. trigger signals. The upper limit is not as distinct as the lower but approximately defines the boundary, at which the spectra start to get heavily distorted by the large number of ions, to the extent that mass lines are difficult to identify or resolve, or are saturated. This sensitivity range of the QI amplitude limits the total

range of particle sizes for a given impact speed, which produce useable spectra and can be considered here.

Another very important issue is the influence the impact speed has on the resulting particle sizes. Due to the large coefficient of -5.59 (Equ. 2.6), small changes in the impact speed cause the observed size range to shift significantly (Fig. 22). For example, at 4 km/s the calculated size range spans radii of approximately 1 to 3 µm, whereas for 8 km/s it ranges from approximately 0.5 to 1.25 µm, potentially less than half the size at double the velocity. At 4 km/s and 10 km/s the size windows that can be observed by the CA subsystem do not overlap. Thus, it is clear that any distribution of calculated particle radii will be dominated by the underlying impact speed distribution. To minimize this effect when comparing CDA spectra, the respective size calculations are conducted only for data in a given narrow speed range. Although this results in a significant fraction of the data being ignored, the 'speed effect' on the calculated/observed size range is mostly neutralized and comparability between calculated particle radii is more reliable.

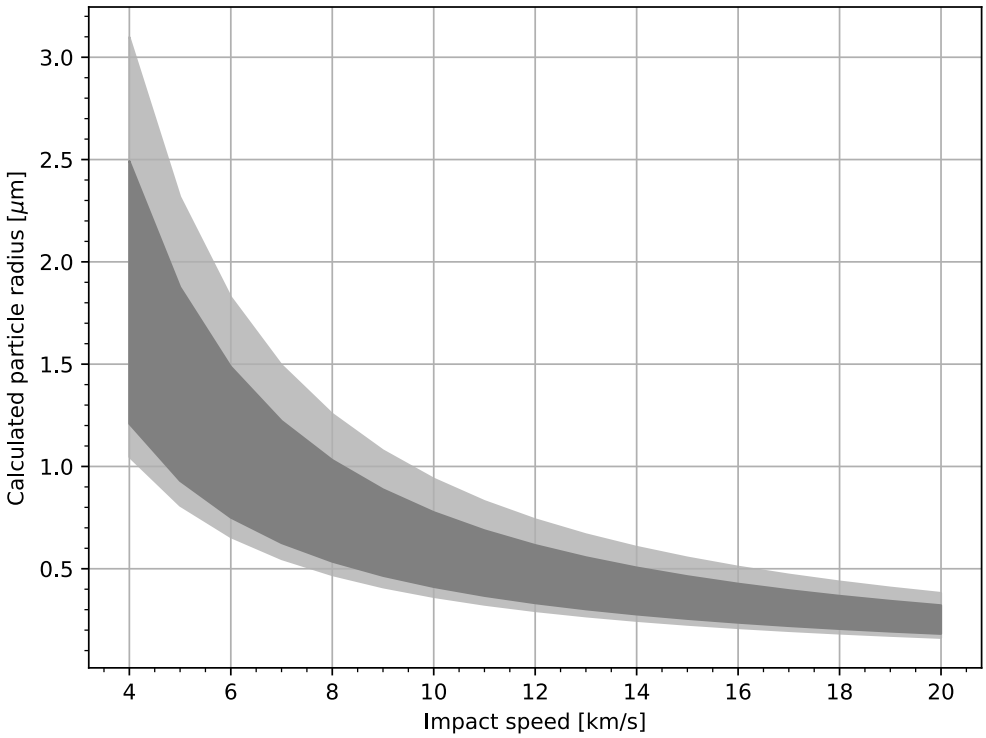


Fig. 22: Calculated particle radii in a maximum QI amplitude range of 2 to 2000 fC as a function of the impact speed, assuming an ice particle with a density of 1000kg/m$^3$. The dark gray area marks the instrument's region of optimal sensitivity between 5 to 500 fC, whereas the light gray areas indicates the total range.

As well as the impact speed "bias", particle composition also has an interfering effect on calculated particle sizes, though usually not as strong as that of the impact speed. Because each chemical compound or element exhibits a different ionization efficiency, or tendency to

form detectable ions, each substance behaves differently during impacts. For example, an ice grain rich in compounds which produce alkaline solutions, such as some salts, produces larger amounts of ions at any given impact speed than an impact of an alkaline-poor composition grain. In minerals (see below) the relative tendency to form ions is quantified using relative sensitivity factors (RSFs, eg. Stephan, 2001). For ice grains with different compositions, the surplus or varying ion production has to be taken into account or the resulting sizes will be overestimated. Hence, it's necessary to apply an RSF-like composition-correction ($k_{comp}$) for the QI amplitudes:

$$QI_{corr}[C] = \frac{QI_{raw}}{k_{comp}}, \tag{2.9}$$

which reflects this tendency to produce ions (e.g. as performed by Fiege et al., 2014 for individual elemental abundances). For various kinds of mineral dust (metal and silicates) first results have already been produced and published by using a Van de Graaff dust accelerator (Fiege et al., 2014; Hillier et al., 2013 & 2018). Because icy dust samples cannot be used in such an accelerator, an alternative experimental approach had to be used, the LILBID experiment. This instrument allows spectra due to ice particle impacts to be mimicked, and thus provides a method to experimentally determine the required correction values for the different compositional types of ice particles. This was already performed by Wiederschein et al. (2015) with aqueous salt solutions with different salt concentrations ($c_{salt}$; Postberg et al., 2009a) for salty ice particles:

- Type 1 → $c_{salt}$: $10^{-6}$ mol/L NaCl in $H_2O$ → $k_{comp} = 1$
- Type 3 → $c_{salt}$: 0.2 – 0.3 mol/L NaCl in $H_2O$ → $k_{comp} \approx 4$

As presented later, a part this work is to determine the first time such values for organic-bearing ice particles (Type 2) and compare the results with the values determined for the other types of ice grains from Wiederschein et al. (2015). Both the details of the task as well as the setup itself will be introduced in section 2 of this main chapter.

## 1.3 Data

The major objective of this work is to derive a comprehensive image of the E-ring dust as seen by CDA's chemical analyzer subsystem. Because the E-ring is a spatially extended object, its dust particle constituents vary across a wide range of orbital parameters. To disentangle them, two orthogonal spatial parameters were chosen for the analysis:

- **Radial distance**

  Cassini was orbiting Saturn close to the ring plane at low inclinations

  Variable parameter → radial distance to the Saturnian barycenter (SBC)

  Fixed parameter → < 0.1 $R_{Saturn}$[a] distance to the equatorial ring plane (RPL)

- **Vertical distance**

  Cassini was orbiting Saturn on significantly inclined orbits

  Variable parameter → height above/below RPL

  Fixed parameter → 4.3 – 5.0 $R_{Saturn}$ radial distance to SBC at RPX[b]

The radial selection criteria are limited to the close proximity of the RPL to minimize vertical interferences. The vertical selection criteria have been limited to the region between Enceladus' and Tethys' orbital distance, as it is the youngest and densest part of the E-ring and thus provides compositional information which are least altered by radial migration and potential ageing effects. It is not possible to completely avoid interferences between these two criteria, but by taking into account instrument pointing as well as the impact speed, it's possible to reduce the bias. Based on these two criteria, the periods listed in Table 2 and 3 have been selected as a basis for the data used for this three-dimensional E-ring analysis. It is also important to mention here the difference in the Kepler-RAM speeds between the two spatial selection criteria. While the radial spectral data were recorded at Kepler-RAM speeds of approximately 4 to 8 km/s, the vertical data were recorded at significantly higher speeds of at least 10 km/s. Since Cassini moved on highly inclined orbits during the measurements for the vertical data, the relative velocities between particles and spacecraft were much faster and the resulting impact speeds therefore much higher.

[a] 1 $R_{Saturn}$ = 60268 km (Kempf et al., 2018)

[b] RPX = moment of ring plane crossing

Table 2: Data sets selected for the analysis with respect to the radial distance. Those marked with "*" represent data that were compositionally analyzed for the first time in this work. Vertical distance to RPL is < 0.1 $R_{Saturn}$.

| Year | Day of Year (DoY) | | UTC-Time | | Number of events (incl. noise events) | Av. Kepler-RAM speed [km/s] | Total radial distance to SBC [$R_{Saturn}$] | MP trigger threshold |
|---|---|---|---|---|---|---|---|---|
| | Start | End | Start | End | | | | |
| 2005 | 67 | 69 | 20:03:02 | 03:36:04 | 1421 | 8.0 | 3.5-10.3 | 1-2 |
| 2005 | 267 | 269 | 03:02:44 | 14:08:37 | 562 | 8.2 | 5.1-26.0 | 1 |
| 2005 | 302 | 303 | 20:51:10 | 09:29:16 | 910 | 6.4 | 4.6-7.8 | 2 |
| 2005 | 358 | 359 | 04:12:00 | 06:57:38 | 819 | 6.2 | 4.6-10.6 | 2 |
| 2006 | 56 | 57 | 20:00:36 | 02:28:47 | 6757* | 6.5 | 7.6-10.0 | 2 |
| 2006 | 80 | 88 | 01:03:37 | 21:37:31 | 1046 | 6.5 | 6.2-54.4 | 1-2 |
| 2006 | 182 | 182 | 02:20:01 | 09:29:55 | 5739* | 6.7 | 9.1-12.0 | 2 |
| 2015 | 129 | 129 | 05:03:38 | 22:07:27 | 2601 | 6.5 | 4.1-8.7 | 1 |
| 2015 | 130 | 130 | 18:43:25 | 21:38:59 | 83 | 6.4 | 13.5-14.6 | 1-2 |

Table 3: Data sets selected for the analysis with respect to the vertical distance. Negative values for the distance to RPL represent the southern hemisphere below Saturn's equatorial ring plane (z < 0) and positive values indicate a northern hemisphere position above the equatorial ring plane. Cassini's vertical flight direction is given by the order of the distance values: - → + = upwards & + → - = downwards

| Year | Day of Year (DoY) | | UTC-Time | | Number of events (incl. noise events) | Av. Kepler-RAM speed [km/s] | Vert. distance to RPL [$R_{Saturn}$] | Distance to SBC at RPX [$R_{Saturn}$] | RPX angle [°] | MP trigger threshold |
|---|---|---|---|---|---|---|---|---|---|---|
| | Start | End | Start | End | | | | | | |
| 2006 | 337 | 337 | 00:15:36 | 03:30:41 | 605 | 12.5 | -0.25 to 0.8 | 4.97 | 52.9 | 1-2 |
| 2007 | 130 | 130 | 19:13:38 | 19:59:51 | 170 | 10.3 | 0.16 to -0.27 | 4.76 | 37.1 | 2 |
| 2008 | 130 | 131 | 22:07:52 | 03:23:14 | 553 | 14.5 | 1.55 to -2.53 | 4.48 | 61.2 | 1-2 |
| 2008 | 321 | 321 | 20:09:16 | 21:54:49 | 60 | 16.2 | 0.84 to -0.68 | 4.34 | 69.6 | 1-2 |

The spectral data from Postberg et al. (2018a) are used to augment the radial analysis in a second analysis step. These data represent an extensive collection of Type 2-HMOC spectra, a subtype of Type 2 with spectral features indicative of high-mass organic cations (Table 1). Since subtypes are not taken into account during the analysis of the other data sets (Table 2 and 3), these additional data can provide a better insight into Type 2. It is important to note that these data have neither been limited with respect to the vertical distance to RPL nor the impact speed. Thus, interpretation of the respective results must be undertaken with even more caution than for the results derived from the data in Table 2 and 3.

## 1.4 SPICE based spectra analysis

The evaluation of the processed spectral data was conducted with routines based on Python 3 and the boxcar analysis method (see appendix, section "Boxcar analysis"), using a 50 % overlap of the boxes. The applied size determination was previously explained in detail (section 1.2.4), and the relative frequencies ($\nu_{Type}$) of the spectral types in each box, used for the compositional analysis, were calculated by:

$$\nu_{Type}[\%] = \frac{n_{type}}{n_{tot}} * 100 \tag{3.0}$$

where $n_{type}$ represents the respective individual spectrum count and $n_{tot}$ the sum of all spectral counts in one box ($n_{tot} = n_{type1} + n_{type2} + n_{type3} + n_{type4}$). It is important to note that this does NOT represent an absolute abundance but instead the relative frequencies of particular types. This approach is necessary because the absolute numbers of dust particles in the E-ring decrease by several orders of magnitude, both radially from 4 to 18 $R_{Saturn}$ relative to Saturn's Barycenter (SBC), as well as vertically, when going from the ring plane (RPL) to heights of ± 1 $R_{Saturn}$ (see e.g. Fig. 38, or Srama et al., 2011 for an illustrations of this). The applicable error bars represent the standard error of the mean (SEM, $\Delta\nu_{type}$) and are calculated by:

$$\Delta\nu_{type}[\%] = 100 * \sqrt{\tau_{type} * \frac{1-\tau_{type}}{n_{tot}}} \tag{3.1}$$

where $\tau_{type} = \frac{\nu_{type}}{100} = \frac{n_{type}}{n_{tot}}$. For the HMOC data from Postberg et al. (2018a) the same formulae are applied, where $n_{type} = n_{HMOC}$.

All required metadata, e.g. spacecraft position, speed and instrument pointing were extracted via SPICE (Acton, 1996; Acton et al., 2018) and the CSPICE[a,b] based "SpiceyPy" python tool (Annex et al., 2020). This provides many routines for multiple purposes, for

[a] CSPICE is the implementation of SPICE for C-based programming languages
[b] https://naif.jpl.nasa.gov/pub/naif/toolkit_docs/C/cspice/

example data extraction and vector analysis, as well as spacecraft navigation and trajectory reconstruction. For more details about the used routines, see the respective links to the CSPICE homepage, provided by footnotes in the text. All bar one of the SPICE kernels of the Cassini orbiter used in this research are freely available on the NAIF homepage[a]. The only kernel not originating from NAIF is the SATURNJ2000 coordinate reference frame kernel, which is a modified version of the common J2000 reference frame kernel. This coordinate frame is defined as follows:

- The x-axis is directed towards the vernal equinox of January 2000
- The z-axis is parallel to Saturn's positive rotational axis
- The y-axis is the cross product of x- & z-axis.

This reference frame kernel was kindly provided by colleagues of the IRS[b] in Stuttgart, Germany.

[a] https://naif.jpl.nasa.gov/naif/data_archived.html
[b] https://www.irs.uni-stuttgart.de/

## 2. Laser desorption laboratory experiments for icy dust analogues

The characteristics of microscopic water ice particles make it hard to conduct analogue measurements with a Van de Graaff-accelerator-based impact ionization mass spectrometer, as can be done for refractory dust grains (e.g. Hillier et al., 2009; Mocker et al., 2011; Fiege et al., 2014; Li et al., 2013 and 2014). In general, nonconductive particle samples need to be coated first with a conductive layer (Hillier et al., 2009; Fielding et al., 2015), e.g. conductive polymers or platinum, before they can be accelerated in electrostatic fields. This process involves wet-chemical, room temperature and above, treatment and thus works only for sufficiently durable materials, e.g. silicates (Srama et al., 2009; Hillier et al., 2009, 2012, 2018; Fiege, 2013; Fiege et al., 2014). Therefore, a different approach is required to simulate the impact ionization process of water ice grains. This is based on the desorption of ions and molecular fragments from a µm-beam of liquid water by a pulsed infrared laser, known as laser-induced liquid beam ion desorption (LILBID). Combined with a time-of-flight mass spectrometer and delayed ion extraction, this new approach enables CDA spectra of ice particles and their components to be mimicked for detailed analysis (e.g. Charvat & Abel, 2007; Postberg et al., 2009a; Wiederschein et al., 2015; Klenner et al., 2019, 2020a+b). By varying the duration of the extraction delay, the so-called delay time (DT), it's possible to emulate different impact speed regimes (IS) of CDA spectra, with an approximate correlation of $DT \sim IS^{-1}$ (see Klenner et al., 2019). Hence, a low DT implies a high IS and vice versa.

The LILBID experiments conducted for this work are dedicated to studying the effect on the ion yield of adding specific amounts of particular compounds to the LILBID water matrix. This is done by comparing the compound-containing spectra with spectra of the well-known reference of $10^{-6}$ M NaCl. This reference was chosen because it represents the compositional analogue for the numerous Type 1 particles (Postberg et al., 2009a) and thus are of particular interest. The resulting ratios can then be used to calculate the composition-correction applicable to the CDA ion yields (in particular the QI-channel amplitudes) to improve the aforementioned particle size determination. As a first step, this work focused on the more abundant organic compounds, described by Khawaja et al. (2019). After the organics' measurements, a very high concentration of NaCl was analyzed for the newly introduced Type 5 (see main chapter D). The required measurements of the highly concentrated NaCl solution were conducted by Fabian Klenner.

In the first part of the following section there will be a summary of the substances and mixtures used to conduct the measurements. The second part provides an overview of the evaluation steps based on a simple Python routine. For a more detailed description of the instrument and its working principles see appendix (section "LILBID experimental setup").

## 2.1 Used substances and mixtures

Several classes of organic molecules have been identified by Khawaja et al. 2019 in CDA spectra of E-ring water ice particles (Type 2):

- N-bearing
  e.g. amines or nitriles
- O-Bearing
  e.g. alcohols or aldehydes
- Pure hydrocarbons
  e.g. aliphatic and aromatic

However, it was not possible to clearly identify single substances out of these classes. Consequently, there is the possibility that there is more than one substance responsible for the broad spectral features observed in Type 2 spectra. This issue makes it necessary to introduce a preparatory step. Before the actual measurements can start, a suitable set of single substances must be identified, whose combined spectral features exhibit the best possible match for "ordinary" Type 2 spectra (see Fig. 21-b). These CDA spectra do neither exhibit clear high mass organic features, as shown in Postberg et al. (2018a), nor do they reveal a significantly enhanced concentration of salts ($>>10^{-6}$ M). As previously mentioned in section "Known spectral types" (Table 1), there are two prominent, broad spectral features in Type 2 spectra, which are crucial to match:

- X29: 26 u – 31 u
- X43: 39 u – 45 u

According to Khawaja et al. 2019, the X29 feature is formed of two-part organic fragments, either from pure hydrocarbons with various degrees of H-saturation or N- & O-bearing fragments. Vice versa, the X43 feature represents three-part compounds, predominantly O-bearing molecular fragments but also again hydrocarbons with various degrees of saturation. As well as X29 and X43, there are two further distinct, but less abundant features, seen in Type 2 spectra:

- X18: 17 u – 18 u
- X77: 77 u – 79 u

The X18 feature is most frequently produced from ammonia ions $[NH_{3\text{-}4}]^+$ but also water ions $[H_2O]^+$ are interfering here. This makes a clear assignment difficult. According to the experiments of Khawaja 2016, discrimination is possible based on comparison to the strong, adjacent mass line of the hydronium ion $[H_3O]^+$ ($m/z \approx 19u$). The amplitude of an X18 feature, if produced solely by $[H_2O]^+$, hardly ever exceeds 10% of the amplitude of the $[H_3O]^+$ peak, even at the highest laser energies and low delay times. However, even small amounts of nitrogen-bearing substances, for example amines or amino acids, can raise the amplitude of X18 easily to amplitudes of around 50% that of the $[H_3O]^+$ peak for any given LILIBID setting. Thus, a comparably high X18 amplitude is a strong indication for the presence of ammonium bearing substances. The X77 signature is the result of protonated/deprotonated phenyl rings $[C_6H_{6\pm1}]^+$ (Khawaja et al., 2019). The knowledge of these features results in the set of single substances, shown in Table 4, selected for tests at various concentration levels. All subsequently mentioned solutions, both for single-substance or mixtures, are based on doubly distilled and deionized $H_2O$ (18.2 MΩ "Milli-Q").

Table 4: List of tested single substances. Solutions are based on a $10^{-6}$ M NaCl solution of doubly distilled and deionized $H_2O$ (18.2 MΩ "Milli-Q").

| Substance name | Chemical Formula | Contributed organic feature(s) |
|---|---|---|
| Iso-Butyraldehyde | $C_4H_8O$ | X29, X43 |
| n-Butyraldehyde | $C_4H_8O$ | X29, X43 |
| Phenol | $C_6H_6O$ | X77 |
| Propionaldehyde | $C_3H_6O$ | X29, X43 |
| Ethanolamine | $C_2H_7NO$ | X18, X29 |
| 2-Propanol | $C_3H_8O$ | X29, X43 |
| n-Butylamine | $C_4H_{11}N$ | X18, X29, X43 |
| 3-Pentanol | $C_5H_{12}O$ | X29, X43 |

Different amounts of each substance (Table 4) are dissolved in a $10^{-6}$ M NaCl solution. This minor amount of salt is required to emulate the natural, minor traces of salts in each Type 2 particle (see Postberg et al., 2009a & 2018a; Khawaja et al., 2019). To reduce unwanted interferences from molecular mass lines at higher masses, and to mimic fragments from the otherwise insoluble aliphatic hydrocarbons, only low mass (e.g. carbon number 2-5) non-aromatic organic compounds were chosen, each carrying N- and/or O-bearing functional groups. The latter improves significantly the solubility and allows a wider concentration range to be tested. After the individual tests, three substances were selected to produce different

mixtures for the measurements to determine the effect of composition on the ion yield. The selection of substance and concentration was based on the substance's capability to properly reproduce the aforementioned spectral features X29, X43 as well as X18. The X77 feature was ultimately excluded, because phenol, the only reasonably soluble substance found to reproduce this feature, introduced too many spectral features at other masses, complicating the interpretation of the spectra. In total, four mixture solutions were produced for the ion yield measurements: Mixture A, B C and D. The final selection of the chosen single substances and their concentrations, used to produce these mixtures, are given in Table 5 (see main chapter C, "Results").

Each mixture as well as the reference solutions (18.2 MΩ $H_2O$ and $10^{-6}$ M NaCl) were measured using three different delay times (DT) to emulate different impact speed regimes of CDA spectra and thus reproduce any potential dynamical effects on the ion yield. The delay time ranges correspond to the following, approximate impact speed regimes, based on the work of Klenner et al. (2019) for salt-poor water ice particles:

- Low DT: < 5.5 µs → 9-11 km/s
- Moderate DT: 5.5 – 6.5 µs → 6.5-8.5 km/s
- High DT: > 6.5 µs → 4-6 km/s

The exact DTs are tuned within the respective range at the beginning of each measurement day, depending on the daily calibration performance of the instrument. Final DT values are given in main chapter C, while further instrument settings, e.g. voltages, nozzle diameter or laser energy, are listed in the appendix (section "LILBID measurement settings", Table 8).

To look for possible systematic effects on spectra from instrument shifts (due to e.g. temperature changes) or sample aging, repeat measurements were made. A new sample of mixture A was assembled again a day after the initial measurements were made. Subsequently, both the old and the new sample of mixture A were measured, labeled as follows (see Fig. 23):

Mixture A, sample 1 at day 1 → Mix A-1.0

Mixture A, sample 1 at day 2 → Mix A-1.1

Mixture A, sample 2 at day 2 → Mix A-2.0

For the same purpose, mixture B was measured again a second time, roughly half an hour later on the same day as its initial measurement. Labels are as follows (see Fig. 23):

Mixture B at $t_0$ → Mix B-1st

Mixture B at $t_0$ + 30 min → Mix B-2nd

The measurements of highly concentrated NaCl were performed with a solution of 4 M NaCl under the same procedure as for the measurements of the organics. The exact DT values are given in main chapter C, while the other instrument settings can be found in the appendix (see "LILBID measurement settings", Table 8).

## 2.2 LILBID spectra analysis via Python

The evaluation of the recorded spectra was done using a Python routine. This determined the sample ion yield by comparing the spectral integral of the sample with the spectral integral of a known reference, producing the spectral ratio ($k_{IY}$):

$$k_{IY} = \frac{Int_{Sample}}{Int_{Reference}} \tag{3.2}$$

However, before the integrals were calculated, all LIBID spectra were subject to baseline correction based on "adaptive iteratively reweighted Penalized Least Squares" or airPLS (Zhang et al., 2010). One spectral integral is formed by the following approximation:

$$Int_x = \sum_{i=0}^{n-1}[\frac{(m_{i+1}-m_i)}{2} * (Amp_i + Amp_{i+1})] \tag{3.3}$$

Here "i" is one datapoint in the respective spectrum, while "n" is the maximum number of recorded datapoints. "$m_i$" is the mass/charge ratio at "i", calculated via mass calibration from the TOF "$t_i$" at "i". The used mass calibration is a quadratic equation: $m_i = a * t_i^2 + b * t_i + c$. The values for a, b and c can vary slightly, depending on the instrument's daily performance and the measured substances. Exact numbers are given in the appendix (section "LILBID measurement settings", Table 8). When the individual spectral ratios of each single measurement in one reference were obtained, the three DT regimes were statistically evaluated to produce an average ratio for each DT regime. The composition-correction ($k_{comp}$) was then finally calculated by forming the total average ratio from the three DT regime average ratios.

# C. Composition dependent ion yields after impact ionization

## 1. Introduction

Unlike refractory materials, e.g. silicates, oxides or metal, ice particles are difficult to use for analogue experiments in an electrostatic dust accelerator to study the compositional influence on the ion yield. As previously mentioned, they don't survive the necessary coating process (e.g. Pt coating, Hillier et al., 2009), or the currently used charging technique within the accelerators. But reliable knowledge about the compositional influence on charge generation during impacts is crucial to deduce particle sizes from ion yields, because different compositions produce different amounts of ions under identical conditions. Remaining uncorrected, this would introduce a bias to the size determination. Therefore, the alternative experimental approach of laser-induced liquid beam ion desorption (LILBID) has been chosen to determine compositional dependences on the ion yields. It allows various chemical compounds in a liquid water matrix, which were reported to be present within the E-ring ice grains, for example different salts (Postberg et al., 2009a) or organic substances (Postberg et al., 2018a; Khawaja et al., 2019), to be analyzed. Previous work has so far studied primarily the impact of increasing salt concentrations on the ion yield (Wiederschein et al., 2015) and showed a distinct, non-linear, correlation.

As a next step, possible correlations in ion yield for polar, organic substances with low to moderate molecular masses, typical of those implied to be present in most Type 2 particles (Khawaja et al., 2019), were investigated. For this purpose, sample spectra are compared with a reference spectrum of a solution of $10^{-6}$ M NaCl. The resulting ratios reflect the ion yield of the sample material and can be used to determine a composition-correction to help achieve unbiased particle size determinations. The same procedure is similarly carried out for Type 5, the new compositional type in the CDA data (see main chapter D). LILBID spectra of a concentrated NaCl-solution (4 M) are analyzed for this purpose. The respective measurements were conducted by Fabian Klenner. Composition-correction values for Type 1 and 3 were derived from the aforementioned ion yield work of Wiederschein et al. (2015).

# 2. Results

The following three substances were selected from the list of single substances (see Table 4) for the actual mixture measurements (see Table 5):

n-Butyraldehyde → Aldehyde/Oxygen-bearing

n-Butylamine → Amine/Nitrogen-bearing

3-Pentanol → Alcohol/Oxygen-bearing

Different concentrations of n-Butylamine were selected to take into account the varying amplitudes of the X18 spectral feature in Type 2 spectra.

Table 5: Final mixtures for the LILBID measurements. Solutions are based on a $10^{-6}$ M NaCl solution in 18.2 MΩ $H_2O$. Substance concentrations are given in mol/kg.

| Mixture | Substances & Concentrations [mol/kg] | | |
|---|---|---|---|
| | n-Butyraldehyde | n-Butylamine | 3-Pentanol |
| A | 0.1 | $10^{-3}$ | 0.1 |
| B | 0.1 | $10^{-4}$ | 0.1 |
| C | 0.1 | $10^{-5}$ | 0.1 |
| D | 0.5 | None | 0.5 |

The resulting spectral ratios ($k_{IY}$) of the different mixtures mostly show similarly growing values with increasing delay time (see Fig. 23). As there is an inverse relationship between LILBID delay times and CDA impact speeds, a low delay time corresponds to a high impact speed and vice versa (see Klenner et al., 2019). However, mixture A shows some differing values (see Fig. 23, green lines). Ratios of the first samples of mixture A (Mix A-1.0 & Mix A-1.1) are much lower than the ratios of the other mixtures (B – D), and they decline further with increasing delay time. In contrast, the second sample of mixture A (Mix A-2.0) shows significantly higher values overall, and only minor changes with respect to the different delay times. A statistical evaluation of the ratios in Fig. 23 produced the following average ratios:

Low DT: $1.016 \pm 0.006$

Moderate DT: $1.010 \pm 0.014$

High DT: $1.041 \pm 0.028$

The corresponding histograms can be found in the appendix (section “Ion yield histograms”, Fig. 41). The total average ratio is found to be $1.022 \pm 0.011$.

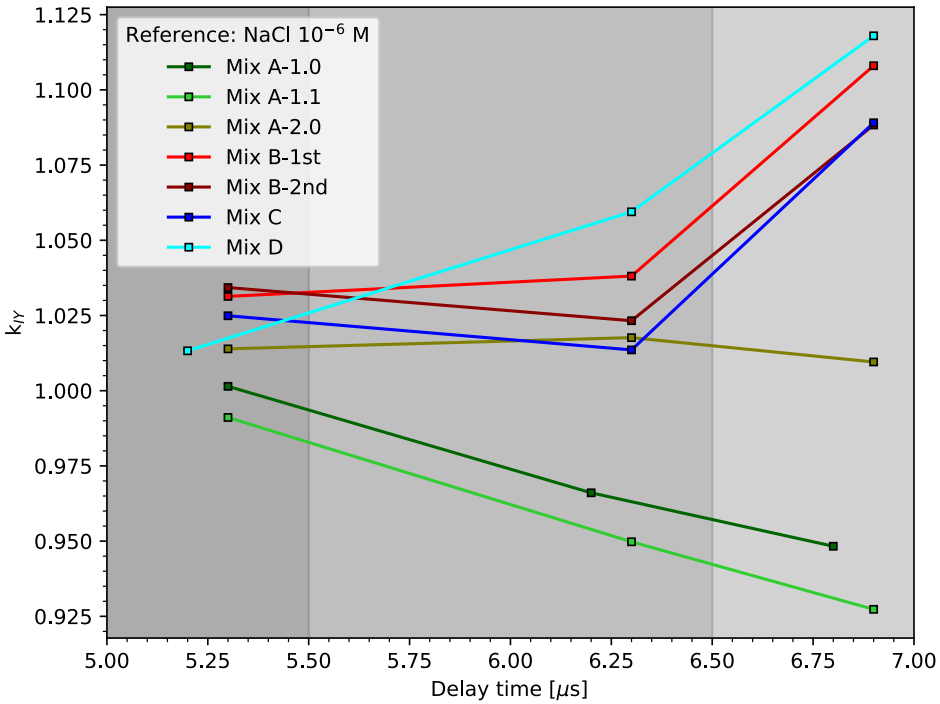


Fig. 23: Spectral ratios ($k_{IY}$) of the different mixtures (Table 5) for the $10^{-6}$ M NaCl reference. The three delay time regimes are displayed by the different grey scaled areas.

The wide spread of the average ratios can be clearly addressed to the anomalous behavior of mixture A compared to the mixtures B – D (see Fig. 23). Thus, a second, more constricted statistical evaluation is proposed here, that excludes mixture A for now:

Low DT: 1.026 ± 0.004

Moderate DT: 1.034 ± 0.009

High DT: 1.101 ± 0.006

The histograms can again be found in the appendix (section “Ion yield histograms”, Fig. 41). The total average ratio is 1.053 ± 0.01. These new average ratios, constrained to mixtures B – D, now show a clear positive correlation between average ratio and delay time. A similar correlation between spectral ratios and delay times is also visible for the highly concentrated salt measurements (see Fig. 24), conducted for Type 5, although here the ratios are higher than before, with the total average ratio now 1.316 ± 0.181.

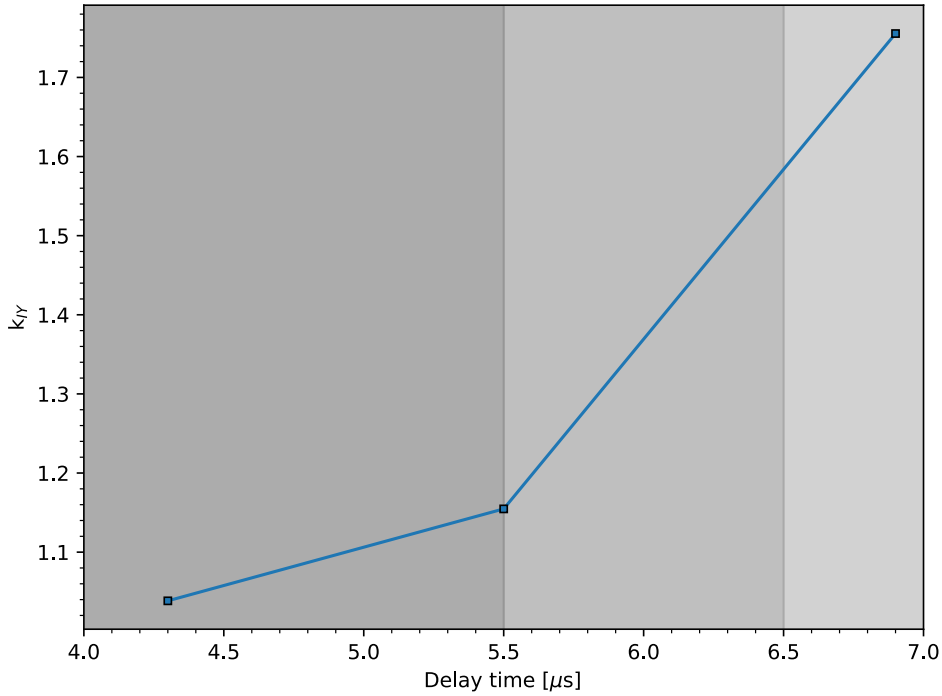


Fig. 24: Spectral ratios for the measurement of the 4 M NaCl solution. The three delay time regimes are shown by the different grey scaled areas. Reference is, as before, a $10^{-6}$ M NaCl solution. Measurements conducted by Fabian Klenner.

Based on the results of Wiederschein et al. 2015 (see Fig. 25) it's possible to directly calculate composition corrections for Type 1 and Type 3 without the need to estimate any spectral ratios. As previously mentioned, Type 1 particles possess a salt concentration of about $10^{-6}$ M (Postberg et al., 2009a), which results in a composition-correction value of about 1 (purple circle). Vice versa, Type 3 particles possess salt concentrations of around 0.2 M (Postberg et al., 2009a). By extrapolating the ion yields for NaCl concentrations above $10^{-1}$ M in Fig. 25 (red, dotted line), the intersection point (yellow square) with the right edge of Fig. 25 (≈ 0.2 M) indicates a composition-correction value of about 4 ± 3 for Type 3.

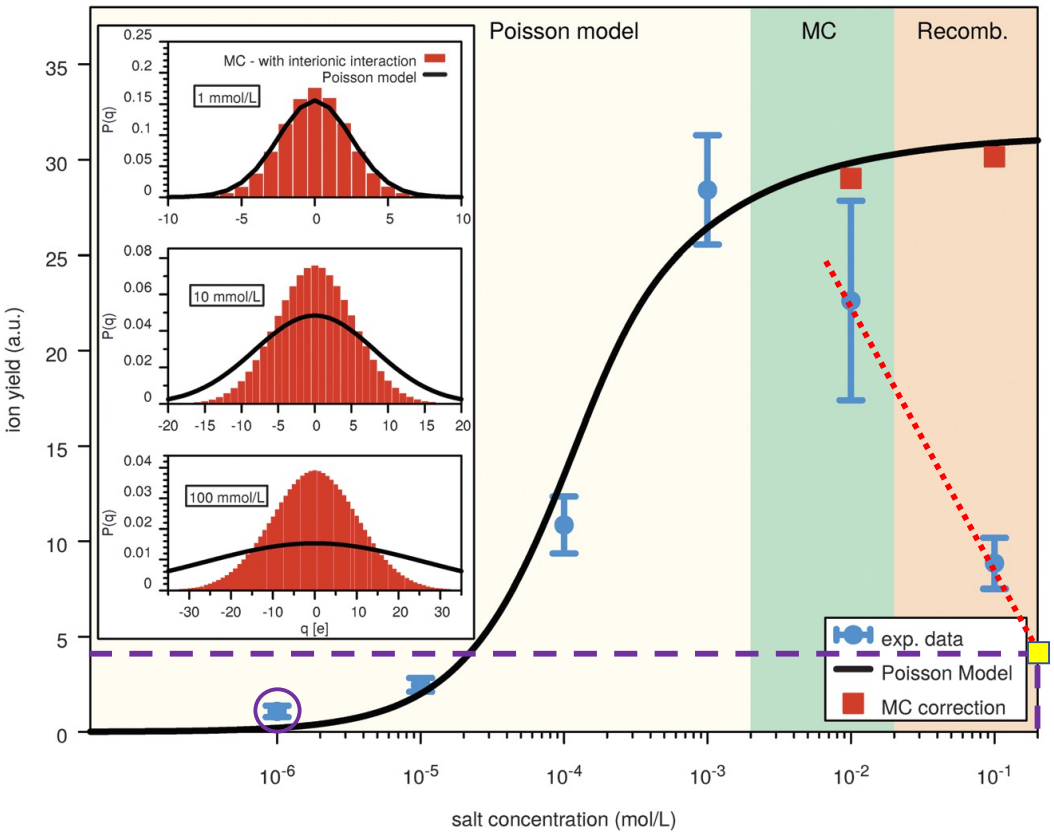


Fig. 25: NaCl concentration dependent spectral ion yields. Adapted from Wiederscheinet et al. (2015). The inclined, dotted red line represents the extrapolated ion yield trend for NaCl conentrations above $10^{-2}$ M (mol/L). The yellow square and the dashed, purple lines mark the intersection point of extrapolation and the salt concentration of Type 3 particles (≈ 0.2 M).

# 3. Discussion

The previously presented results indicate that the concentration of organics necessary to reproduce CDA Type 2 spectra (0.2-1.0 M, see Table 5) result in a slightly increased ion yield (1 → 1.05). In contrast, increasing the concentration of salts (~0.2 M NaCl) results in even larger ion yields (1 → 4). This difference in ion yield reflects the different molecular properties of the used organics and salts. The additional organics seem to ease the production of ions compared to the refence solution but not as much as salts do.

The observed, positive correlation of spectral ratio (≈ ion yield) with delay time (Fig. 23 & Fig. 24) is most likely an instrumental effect. It can be assigned to the delayed ion extraction and tendency of ions and polar yet neutral molecules to form ionic clusters after desorption (Klenner et al., 2019). The analyzed compounds in the samples, e.g. NaCl, cluster with $H_2O$ and/or each other:

| | | |
|---|---|---|
| $Na^+[NaCl]_n[H_2O]_m$ | → m/z = 81u + n* 58u + m*18u | → salt-water cluster |
| $Na^+[NaCl]_n[NaOH]_m$ | → m/z = 81u + n* 58u + m*40u | → salt-salt cluster |
| $[M^a]^+[H_2O]_m$ | → m/z = M + m*18u | → organic-water cluster |

This results in additional mass lines at higher masses in the sample spectra. However, the reference[b] doesn't contain such compounds at all or not enough of them to produce detectable signals. Thus, their spectra just show the common cluster series of $H_3O^+[H_2O]_n$ and $Na^+[H_2O]_n$. It's important to briefly recall, that due to the delayed ion extraction, different velocity, and therefore typically mass, ranges of ions and clusters are preferably extracted, depending on the delay time (DT). A low DT favors light, fast-moving material, whereas a high DT favors heavy, slow-moving material. Based on this, mass spectra recorded using a low DT preferably include mass lines with high amplitudes at lower masses. Vice versa, mass spectra recorded using high DT tend to favor mass lines at higher masses. Thus, recording of the aforementioned, additional cluster mass lines is preferred in the high DT spectra, while in the low DT spectra they just play a minor role. At low DT mass lines from the fragmentation of the organic molecules are also present. But since the mass scale is limited to the lower end, also the number of such mass lines, caused by molecular fragmentation, is limited, compared to cluster mass lines. The presence of additional distinct mass lines at high delay times in the sample spectra increases their spectral integrals compared to the integrals of the reference

[a] M → molecular mass of an organic molecule
[b] $10^{-6}$ M NaCl solution

spectra. Consequently, the spectral ratios (sample/reference) for the high DT regime grow, which ultimately leads to the observed positive correlation of DT regime and spectral ratio.

The anomalous ratios shown by mixture A[a] (see Table 5) may be due to several reasons. The first and probably most obvious explanation is the difference in n-Butylamine ($C_4H_{11}N$) concentrations. From mixture A to mixture B[b] there is a drop in concentration by a factor of 10 and another drop by a factor of 10 when proceeding to mixture C[c]. The concentrations of the other organic compounds remain constant. Mixture D[d] contains no n-Butylamine at all, with increased concentrations of the two other organic components. Assuming that n-Butylamine exhibits a similarly shaped ion yield/concentration distribution, as found for NaCl by Wiederschein et al. (2015), though perhaps shifted, distorted or even inverted to values between 0 and 1, it may be possible, that the chosen concentrations of mixture B and C are located at or close to the flat, constant parts of the distribution curve, while mixture A is located at its slope closer to the sweet spot. The resulting difference in ion yield could then explain the observed anomaly. However, there is one point, which argues against this explanation as the sole one. Only the first sample of mixture A (Fig. 23: Mix A-1.0 & Mix A-1.1) behaves anomalously in all delay time regimes. The second sample (Fig. 23: Mix A-2.0) is clearly affected only in the high delay time regime. This points at an issue with the first sample itself, for example from contamination or mistakes during the process of sample preparation. However, the spectra neither showed clear signs of contamination nor any other indication which could confirm preparation issues. But since the mass spectra of such organic mixtures are relatively complex, due to the numerous cluster mass lines, these explanations cannot be ruled out. Furthermore, there could be yet unknown chemical reactions between the three used compounds, which negatively influence the spectral integrals. Certain mass lines could be suppressed because the underlying molecular fragments have been decomposed during such reactions, producing new, unknown spectral signatures. The spectral signatures which arise from such reactions could interfere with preexisting mass lines, making it impossible to properly identify them. However, the presence of spectral signatures, produced by unknown chemical reactions, which are isobaric with existing mass lines but don't affect two assumed identical mixtures of compounds in the same way (i.e. mixes A-1.0 and A-2.0), also seems unlikely.

[a] Mix A: 0.1 M n-Butyraldehyde, 0.1 M 3-Pentanol, $10^{-3}$ M n-Butylamine
[b] Mix B: 0.1 M n-Butyraldehyde, 0.1 M 3-Pentanol, $10^{-4}$ M n-Butylamine
[c] Mix C: 0.1 M n-Butyraldehyde, 0.1 M 3-Pentanol, $10^{-5}$ M n-Butylamine
[d] Mix C: 0.5 M n-Butyraldehyde, 0.5 M 3-Pentanol

The anomalous behavior of mixture A needs further analysis and laboratory experiments to ultimately determine its origin. Until this is carried out, use of the mixture A results should be halted. The values obtained from the constrained evaluation must therefore be considered as the currently best available numbers. Thus, the final composition-correction used for Type 2 particles in subsequent particle size determination (see main chapter E, section "Radial size distribution") is 1.05, based on the total average ratio of this evaluation.

For Type 5, the total average ratio of approximately 1.3, derived from the highly concentrated NaCl measurements of Fabian Klenner, fits well into the picture of decreasing ion yields for very high salt concentrations, raised and discussed by Wiederschein et al. 2015. However, as shown in the following main chapter D, Type 5 particles not only contain presumably large amounts of sodium salts but also detectable levels of potassium. The highly concentrated NaCl measurements by Fabian Klenner were therefore performed as preliminary tests, potassium-bearing compounds have not yet been investigated via LILBID. Impact ionization of mineral grains indicates that potassium is about two times more sensitive to ionization than sodium (relative sensitivity factors of 72 for Na versus 132 for K, from Fiege et al., 2014). Despite the different original particle compositions, and depending on the actual concentration of potassium salts in the Type 5 grains, it is possible that the actual value for the composition correction may be higher than the 1.3 determined from the 4 M NaCl solution. Since no exact potassium concentration can be given at the moment, for now a higher value of 2 is assumed as the composition-correction factor for Type 5 in the later particle size determination. An upcoming measurement campaign with the LILBID setup is intended to analyze salt-rich and very salt-rich particle compositions, based on the results of this work, and answer outstanding questions about the exact K-content and its effect on composition-correction.

The results from Wiederschein et al. 2015 for Type 1 are quite clear. As mentioned before, $10^{-6}$ M NaCl is the analogue solution concentration which results in spectra that mimic CDA Type 1 spectra (Postberg et al., 2009a). Thus, it has been used as the main reference for the previous LILBID results and its composition-correction is considered to be equal to the estimated ion yield of 1. For Type 3 there is however some uncertainty, due to the way the ion yield has been determined. Considering the type of salt used and the concentration level (Postberg et al., 2009a), a composition-correction of $4 \pm 3$ is expected to be appropriate. In this case, the aforementioned LILBID campaign for salt-rich compositions should also help check the validity of the derived corrections.

# D. Type 5, a new compositional type in the E-ring

Alongside the general processing of spectral data, there is an ongoing search for new spectral types. This chapter will introduce and discuss a newly found compositional type of spectrum.

## 1. Introduction

From the very first results of the CDA spectra analyses it was clear that there are not only various compositional types but also systematic variations within each type category. Ice particles in particular quickly revealed a surprising variety (see main chapter B, section "Known spectral types"). Several subtypes have also been identified in spectra of Type 2 (organic bearing) ice particles, e.g. aromatics, O- & N- bearing compounds (Khawaja et al., 2019) or even high-mass and complex organic molecules (Postberg et al., 2018a). Similarly, spectra of Type 3 (salt rich) ice particles also demonstrate significant compositional variations, e.g. hydroxide- vs. chloride- vs. carbonate- rich compositions (Zou, 2021). Such discoveries are the result of both intensive and extensive manual spectral analysis, including sampling and comparison of hundreds of CDA spectra as well as measurement campaigns with the LILBID experiment (see main chapter B, section "Laser desorption laboratory experiments for icy dust analogues"). However, there are still unassigned spectra and significant effort is continuously spent to understand them. In this spirit and as a next step to broaden the scope of the published compositional types, I present here the next main type, Type 5.

The Type 5 spectra represent an essential part of this thesis. The name originates from the fact that it is the fifth main type discovered so far, following Types 1 – 3 for different kinds of water ice dust and Type 4 for mineral dust (see main chapter B, section "Known spectral types"). While the type has been identified and discussed internally for some time already, this work is its first formal and systematic introduction to a wider audience. In the following sections the basic spectral properties as well as the necessary knowledge for proper identification and classification are given. Finally, the composition and source of this type of particle are discussed.

## 2. Results

Two distinct peaks dominate Type 5 spectra (see Fig. 26), usually exhibiting broadly similar amplitudes (log space). They will be subsequently referred to as the “main peaks”.

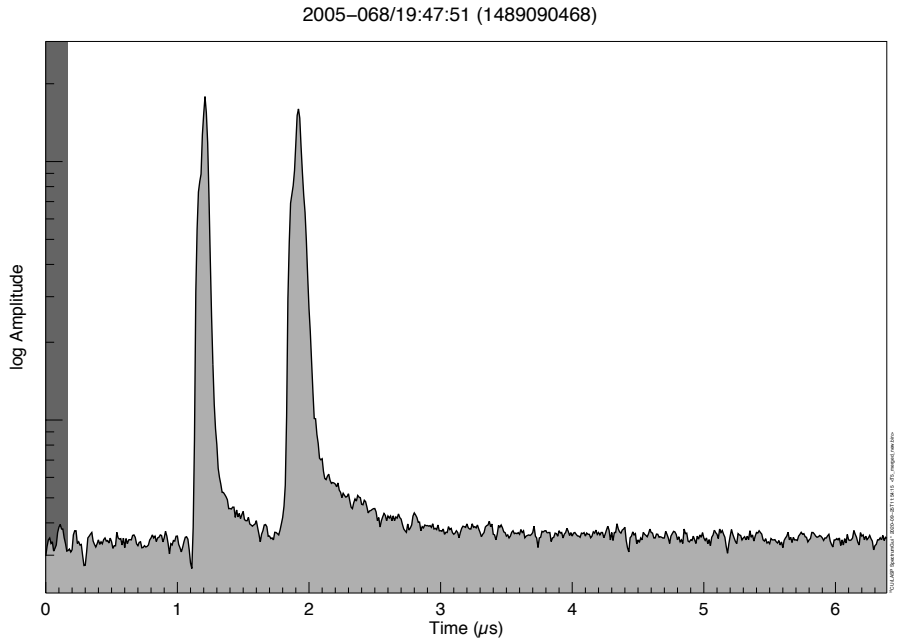


Fig. 26: Example spectrum of the new Type 5

The main peaks often possess a characteristic, asymmetric, shape: a relatively steep left slope and an extended, shallower right slope (see Fig. 27). Apart from the dominating main peaks, there are only few other peaks observable in most of the found spectra. But occasionally,

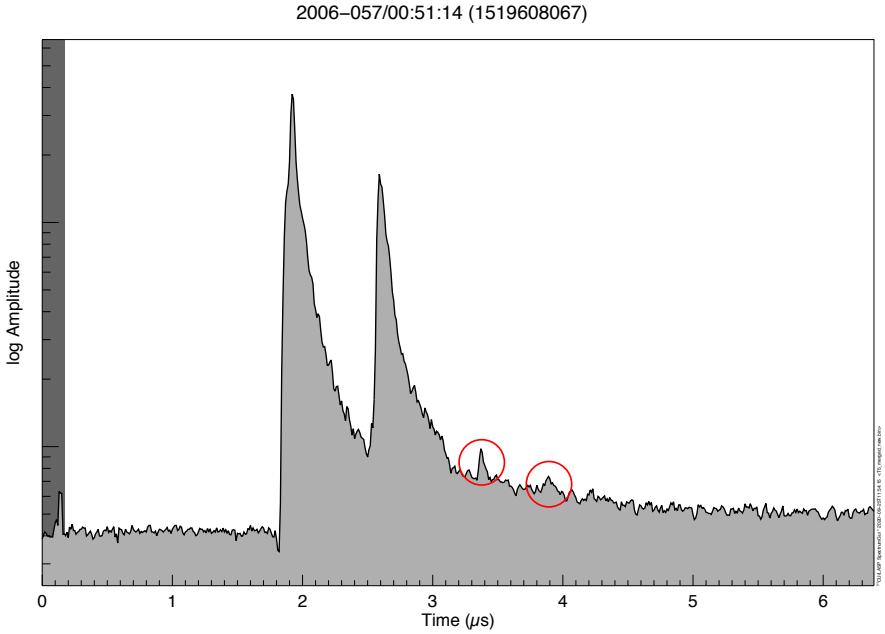


Fig. 27: Example spectrum showing the frequently ocuring extended slopes. The red circles indicate example minor peaks typical of those found infrequently in Type 5 spectra.

very tiny peaks or small peak-like structures can be identified (see Fig. 27). These small spectral features will be subsequently referred to as "minor peaks".

Extensive calibration testing revealed assigning the mass lines $^{23}Na^+$ and $^{39}K^+$ (m/z: 23u & 39u) to the major peaks as the most promising calibration setting. This calibration setting also allowed most of the minor peaks to be assigned to mass lines which were characteristic for an aqueous particle chemistry including salts (see Table 6). Thus, salty $H_2O$-ice seems to be a reasonable scenario for the particle composition. Grains with a similar composition have been shown to produce Type 3 spectra (Postberg et al., 2009a; 2011a).

Table 6: Minor peaks observed at least twice in the 188 Type 5 spectra. Peak masses are based on $Na^+/K^+$ calibration. The corresponding mass lines are derived from those observed in other compositional types (Types 1-4 & stream).

| Peak Mass [u] | Possible Mass Line(s) | Material Indicator |
|---|---|---|
| 26 – 28 | $Al^+/Si^+$ or bipartite organic molecular fragments | Siliceous or organic material |
| 45 – 47 | $^{23}Na_2^+$ | Salts |
| 56 – 57 | $^{39}K^+[H_2{}^{16}O]$ | Salty water ice |
| 62 – 64 | $^{23}Na^+[^{23}Na^{16}OH]$ | Salty water ice |
| 81 – 83 | $^{23}Na^+[^{23}Na^{35/37}Cl]$ | Chloride salts |

Theoretically, there is also an alternative calibration of $^{24}Mg^+$ and $^{40}Ca^+/[^{24}Mg^{16}O]^+$ for the main peaks. But compared to the $^{23}Na^+$ and $^{39}K^+$ calibration, two very strong points argue against it. First of all, magnesium is, unlike sodium, not a monoisotopic element. Thus, it should be possible to observe distinct, characteristic signatures of the two other stable Mg-isotopes[a] in well resolved Type 5 spectra such as Fig. 26. Since this characteristic isotopic pattern has never been clearly observed, it's very unlikely that Mg is present in significant amounts. Second, none of the published, endogenic[b] particle types (Types 1-3 and Stream particles, see Table 1) has thus far shown a magnesium and/or calcium dominated/enriched composition. Only mineral particles (Type 4) are confirmed to exhibit a composition involving these two elements (see Table 1). But these particles are believed to originate from a different source than the other E-ring particles. Summing up, this second calibration option appears to be very unlikely compared to the first option of $^{23}Na^+$ and $^{39}K^+$. Hence, the following results and discussions refer to the Na/K option and the $^{23}Na$ and $^{39}K$ isotopes.

[a] Mg-Isotopes 24:25:26 → 100:12.66:13.93 (normalized to $^{24}Mg$)
[b] Wrt. the E-ring and its embedded moons

Depending on the respective trigger situation either both main peaks ($Na^+$ and $K^+$) are visible or just $K^+$. The latter occurs when $Na^+$, the first main peak, was the trigger for the spectrum recording (main chapter B, section "Trigger mechanisms and basic spectral properties") and it is therefore not completely recorded. Unfortunately, impacts of other spectral types, producing very low amplitude spectra, in combination with line triggering, produced spectra which appear very similar to Type 5. To avoid confusion, it's necessary first to check the responsible trigger mass line. This is done by setting the remaining main peak to $K^+$ (m/z = 39) and then checking the resulting shift parameter. If it is between approximately -2.1 µs and -2.3 µs (based on Equ. 2.3), spectrum recording triggered on the mass line of $Na^+$ and the spectrum can be considered to be of Type 5. Values higher than -2.1 µs or significantly lower than -2.3 µs indicate a different type of spectrum.

So far 188 Type 5 spectra have been found and confirmed in the radial E-ring datasets (main chapter B, section "Data"). The according meta data (e.g. time stamp of detection, position of detection, QI amplitude, etc.) are available in an ASCII file online[a]. Further potential candidates were found in the spectral data of the close Rhea flyby in 2013 (flyby ID: R4), but since these spectra were recorded with a higher MP shrink factor (= higher spatial sampling rate at cost of spectral resolution), they have to be considered ambiguous and are therefore not taken into account for now. Unfortunately, the aforementioned issue of the QC channel impact trigger becoming insensitive (see main chapter B, section "Trigger mechanisms and basic spectral properties") limits the number of spectra with both main peaks that can be studied and compared. Most Type 5 spectra were triggered by $Na^+$ ions arriving at the multiplier and the first main peak is therefore not part of the spectrum. Ultimately only 19 out of the 188 known Type 5 spectra are qualitatively suitable and were triggered early enough to allow the appearance of both main peaks in the spectrum. They are subsequently referred to as either "archetype spectra" or just "archetypes". The respective spectra are marked with an "a" in the online ASCII file[a]. Based on these 19 archetypes, it is also possible to estimate compositional variations by analyzing the amplitude ratio of the main peaks ($Na^+/K^+$, Fig. 28). Since the minor peaks occur very rarely and exhibit amplitudes too close to the noise, or background flank, level, only the main peaks provide reliable numbers for this purpose. The individual $Na^+/K^+$ peak ratios of the 19 archetype spectra accumulate at around 1 to 1.5. An overall mean value for the $Na^+/K^+$ ratio of this spectral type can be estimated by co-adding the normalized and baseline corrected archetype spectra (Fig. 29). The resulting peak ratio is located at around 1.4

[a] http://dx.doi.org/10.17169/refubium-35885

(red line in Fig. 28) and serves as a first reference value. In general, these numbers are significantly smaller than those observed in Type 3 spectra (Postberg et al., 2009a; Zhou, 2021). More than 99% of those are dominated by Na-salts, thus exhibit ratios of 10 to 1000, with an average of around 100, and only a very small minority (less than 1%) are compatible with $Na^+/K^+$ ratios of around 1 and less. However, the numbers derived from the Type 5 archetypes must be taken with caution, since they represent just a small fraction of the whole Type 5 population. The overwhelming majority of Type 5 spectra were line-triggered on the first of the main peaks ($Na^+$) and thus their $Na^+/K^+$ peak ratios are unknown.

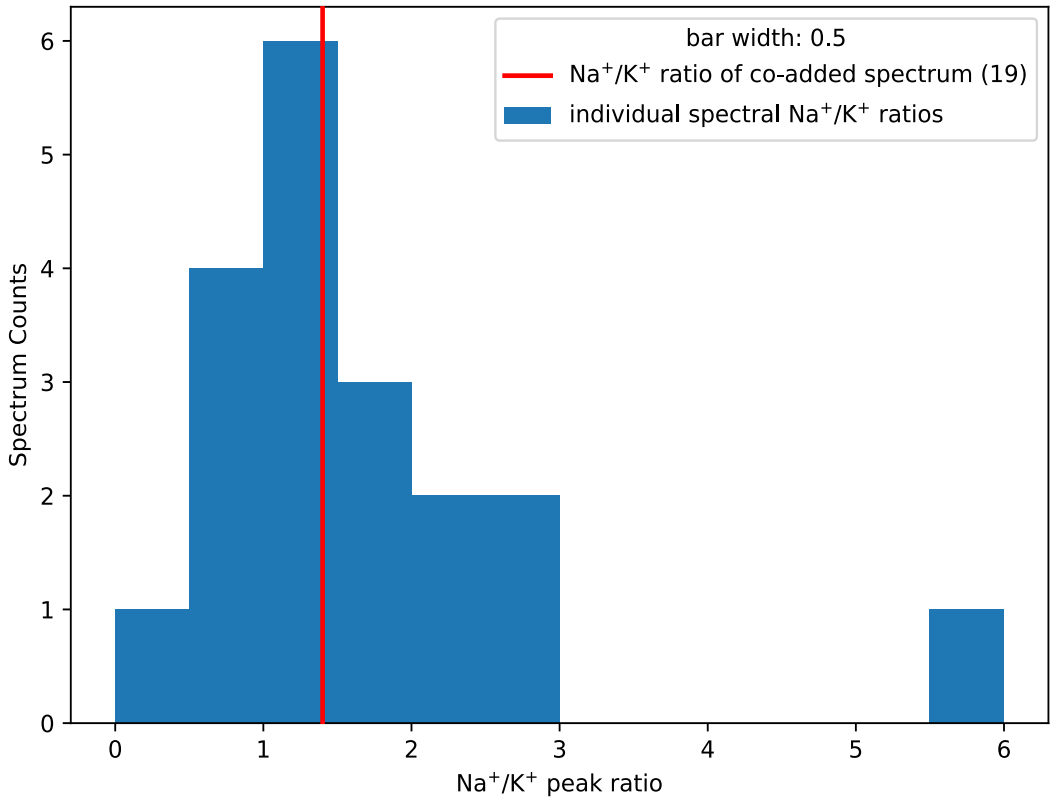


Fig. 28: Histogram of individual spectral $Na^+/K^+$ ratios. The bar width was set to 0.5. The red line marks the overall mean value derived from the co-added spectrum (see Fig. 29)

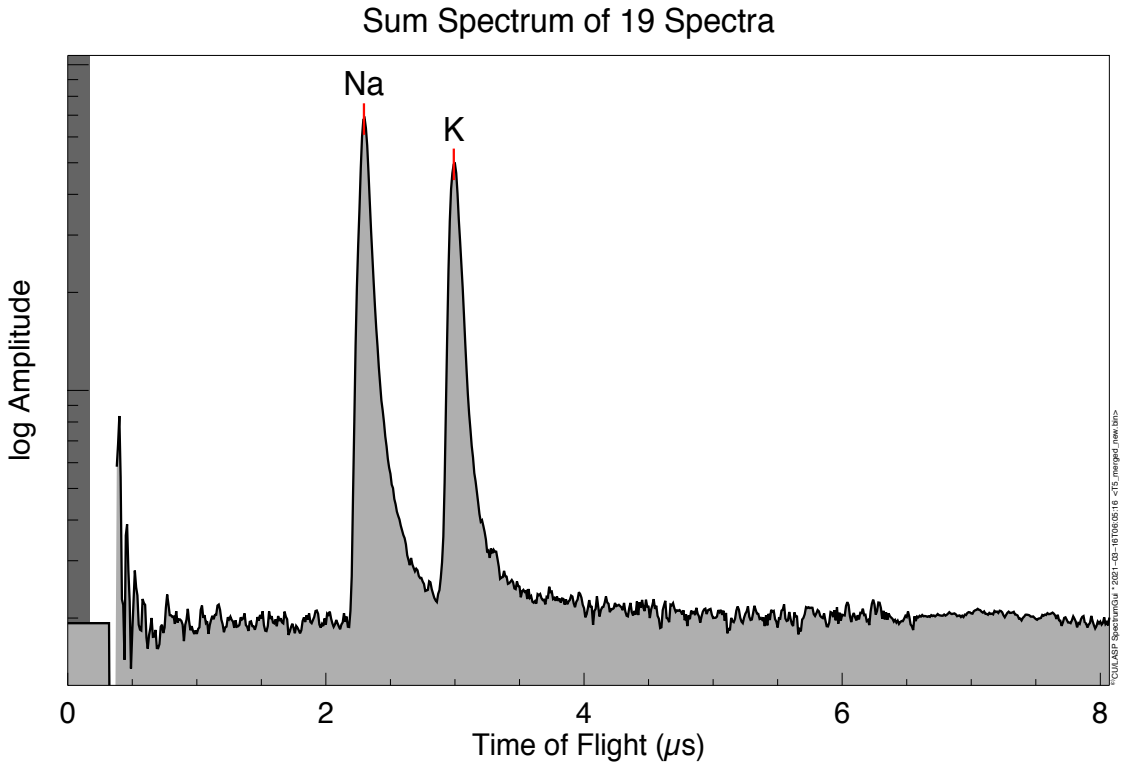


Fig. 29: Co-added Type 5 spectrum, made of the 19 archetype spectra. Individual spectra were normalized and the baseline was removed.

Another important observation from Type 5 spectra to report in this section is the average QI amplitude. The average of these values can give a first estimate about the order of magnitude of the Types' particle radii. The relevant values for Type 5 are listed in Table 7, together with the values for the Types 1 to 3 for comparison.

Table 7: Raw and composition-corrected average QI amplitudes of the three previously known spectral types of icy particles (Type 1-3) and the new type. Only spectral data from the uninclined, radial E-ring scans have been selected, to reduce the disturbing effects of a too wide impact speed distribution. The applied composition-correction values for Types 1 ($k_{comp}$ = 1) and Type 3 ($k_{comp}$ = 4) are based on Wiederschein et al., (2015; see main chapter B, section ""Particle size determination"). For Type 2 ($k_{comp}$ = 1.05) and Type 5 ($k_{comp}$ = 2) the LILBID measurement results presented in main chapter C have been used.

| Type | Number of Spectra | Average QI amplitude [fC] | | Highest detected value [fC] | |
|---|---|---|---|---|---|
| | | raw | corrected | raw | corrected |
| 1 | 4956 | 7.9 ± 0.2 | 7.9 ± 0.2 | 414.4 | 414.4 |
| 2 | 1141 | 62.3 ± 3.2 | 59.3 ± 3.1 | 817.45 | 778.5 |
| 3 | 1251 | 59.2 ± 5.0 | 14.8 ± 1.3 | 3318.1 | 829.5 |
| 5* | 188 | 9.0 ± 1.2 | 4.5 ± 0.6 | 129.1 | 64.6 |

* The new type

Last but not least, it's necessary to briefly anticipate another important result. The radial, relative, spectral frequency distribution of Type 5 in the E-ring can provide valuable insight into its properties. As shown in Fig. 31 (main chapter E, gray color), the relative, spectral frequency of Type 5 reaches a maximum (approx. 8% of analyzed spectra) within a relatively narrow region of the E-ring, between 7 to 9 $R_{Saturn}$ with respect to the SBC. There are very few Type 5 spectra (< 1 %), recorded around the orbital distance of Enceladus, the source of grains producing spectra of Types 1 – 3. Also, at the orbital distances of the other ice moons embedded within the E-ring (Fig. 31: vertical, dashed lines), no obvious increases in the relative frequency of Type 5 spectra are observed.

# 3. Discussion

The spectral simplicity of this particle type does not correspond to its scientific significance. Despite not exhibiting remarkable spectral features its very existence raises questions about hitherto unknown, or purely theorized, processes in Enceladus' dust plume and/or the E-ring. Before discussing the origin and source of grains which result in Type 5 spectra, it's necessary to first consider the role particle composition may play in the generation of these spectra.

## 3.1 Composition of Type 5 particles

The previously shown results clearly argue for a salt-enriched particle composition. The persuasive assignment of $Na^+$ and $K^+$ for the main peaks suggests the presence of a material which includes both elements. Cosmochemically, and in the Saturnian system, two types of materials are known to include both elements: salts or certain silicates (e.g. feldspars). The latter can be excluded, since silicates detected around Saturn are usually dominated by Mg, Ca and/or Fe (Type 4 in Table 1 and Fig. 21-d) or are pure silica (stream particles in Table 1 and Fig. 21-e). The existence of salt-bearing water ice dust particles (Type 3) around Saturn is already confirmed (Postberg et al., 2009a) and thus salts are clearly favored as the source for Na and K ions. Additionally, the occasionally observed minor peaks can be easily ascribed to several mass lines which are also known from Type 3 spectra, for example $Na^+$[NaOH] or $Na^+$[NaCl] (Table 1 and 6). Thus, a Type 5 composition similar to that of Type 3, salts embedded in a water-ice-matrix, seems to be very likely.

The reason for the lack of molecule-related mass lines, represented by the poor amplitudes and frequencies of the minor peaks, could be that these signals are suppressed by the presence of significant concentrations of Na- and K-bearing compounds. This would not be surprising, as the same phenomenon is also known from Type 3 spectra (Postberg et al., 2009a). Here, $H_2O$-related mass lines (e.g. $H_3O^+[H_2O]_n$) are effectively suppressed by the presence of salts, despite the overwhelming compositional dominance of $H_2O$ in the respective particles. Due to the low ionization energy of the alkali metal elements in the salts, significant quantities of ions from these compounds are produced in comparison to those from $H_2O$. Thus, within the impact plasma more ions are produced from the salts than from $H_2O$, despites its overwhelming abundance. This results in an apparent overabundance of salt-derived ions in the recorded spectra. However, in Type 5 spectra the mass lines connected to salt-molecules, usually present in Type 3 spectra with distinct amplitudes, suffer from a different suppression effect. Experimental results from LILBID indicate that high and very high salt concentrations have a

significant impact onto the spectral ion yield (Wiederschein et al., 2015). Initially, the spectral ion yield steadily increases with growing salt concentration until a threshold concentration. When exceeding this level, the correlation reverses and the ion yield decreases with increasing concentration. Since the ion yields in the respective work were estimated based on peak amplitudes related to Na-ions, it implies decreasing peak amplitudes at high and very high salt concentrations. If this effect applies similarly to CDA spectra, it would indicate very high salt concentrations in the original Type 5 particles, above even the level estimated for Type 3 particles.

Despite the previously described arguments in favor of salts in water ice, there are still open questions about the composition. For example, which Na/K-salts are responsible for the spectra and what is the exact salt concentration in the particles? Since these questions cannot be answered exclusively through analysis of CDA spectra, an upcoming dedicated measurement campaign with the LILBID experiment is going to address them in detail. Furthermore, this occasion will be used to determine the exact composition-correction to allow a more accurate particle size estimation.

## 3.2 Origin of Type 5 particles

A clear source of this particle type has not yet been discovered. But there are strong indications for an E-ring origin. First of all, so far Type 5 spectra have not shown spectral signatures typical of high impact speeds (e.g. mass lines of $C^+$ or $Rh^+$, Fiege et al., 2014). Thus, it can be assumed that Type 5 particles exhibit similar orbital dynamics as Types 1 – 3, which originate from Enceladus. Thus, it is unlikely that Type 5 spectra represent exogenous grains – e.g. trespassing ISD or captured IDP. Such particles move on extremely different trajectories compared to most E-ring grains, resulting in very high impact speeds. Second, the radial frequency distribution of Type 5 in the E-ring (Fig. 31) clearly indicates that these particles neither originate directly from Enceladus nor from one of the other moons embedded in the E-ring. There is no distinct accumulation to be found at any of the respective orbital distances of the moons (Fig. 31: dashed, vertical lines), which would indicate active production there. Thus, they must be formed in the E-ring itself and not from one of the moons.

So, how could Type 5 particles be formed? Considering the almost certain presence of salts within Type 5 particles, a lineage between Type 3 and Type 5 is proposed here. E-ring dust particles are subject to ongoing sputtering by Saturn's magnetospheric plasma (Jurac et al., 2001a+b, Johnson et al., 2008), slowly but continuously eroding the particles. For Type 3 particles (Fig. 30, leftmost first step), which can be characterized by a salt-poor outer ice shell

and a salt-rich ice core (Postberg et al., 2009a), the sputtering continuously erodes the salt-poor shell, while the core is unaffected (Fig. 30, second step in the center). This way the absolute amount of salt remains constant while the amount of water ice decreases. Consequently, the salt/water ratio continuously rises, and thus the salt concentration. After reaching a certain level, the salt concentration is so high (e.g. Fig. 30, third step to the right) that it results in the suppression of molecular mass lines in the CDA spectra, leaving behind just the main peaks ($Na^+$ and $K^+$), and producing Type 5 spectra. This process should result in lower particle sizes for Type 5 grains compared to those of Type 3. Looking at the composition-corrected average QI amplitudes in Table 7, a size difference is indeed indicated (4.5 fC for Type 5 vs 14.8 for Type 3). As shown later in main chapter E, the calculated average particle radii (Fig. 35) of all types are also in agreement with this process.

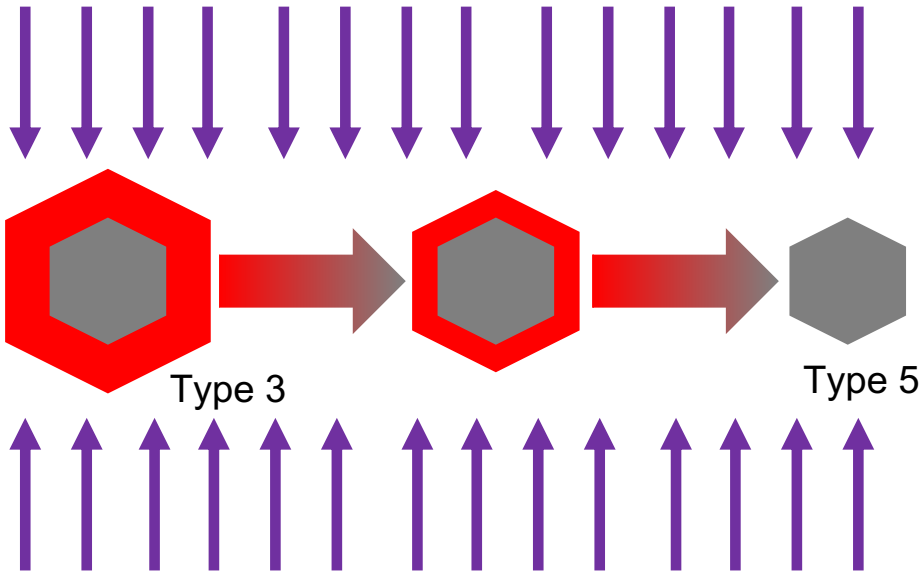


Fig. 30: Simple scheme on how the Type 5 particles possibly form from Type 3's via erosion by plasma sputtering (purple arrows). The ongoing bombardment of the water ice particles by electrons and ions continuously erodes the salt-poor outer ice shell (red) while the salt-rich ice core (grey) is mostly unaffected. Since the absolute amount of salt remains more or less constant the salt concentration is relativly enhanced throughout the process and eventually causes suppression of mass lines in the spactra, producing the known Type 5 spectra. Another clear result of this process is the reduction in particle size.

The accumulation of particles which produce Type 5 spectra within 7-9 $R_{Saturn}$ (relative to SBC) coincides very well with an anomaly of the particle dynamics in this region, which hinders the outwards migration of many E-ring particles. It is caused by the minimum of the local V-shaped electrostatic equilibrium potential of the grains (Mitchell et al., 2005) in combination with a reversal of the polarity of the particle surface charges (Kempf et al., 2006), representing a dynamical barrier that forces many of the dust particles to reside for a long time in this region, the so-called "storage ring" (Kempf & Beckmann, in preparation). A prolonged

residence time in this ring region would also give the plasma sputtering plenty of time to affect the dust particles. Consequently, more highly salt-enriched grains are produced and the relative Type 5 frequency is increased. In the other regions of the E-ring, particle migration happens much faster, resulting in lower production rates and thus a comparably lower relative, spectral frequency. The dynamical feature of the "storage ring", in combination with the aforementioned plasma sputtering driven transformation from Type 3, explains very well both the radial frequency distribution of Type 5 as well as its apparent high salt concentration.

However, there are also issues with the plasma sputtering approach. Firstly, there is the discrepancy in the average $Na^+/K^+$ peak amplitude ratio between Type 3 (~100) and Type 5 (1–1.5). If plasma sputtering really transforms Type 3 into Type 5, then the $Na^+/K^+$ peak ratio values should be more similar and consequently a large number of Na-rich Type 5 spectra has to exist in the spectral data. But where are these spectra? One possible answer could be that they are hidden in the numerous non-archetype Type 5 spectra. The record of most Type 5 spectra (approx. 90%) was initiated by the line-trigger of the $Na^+$ mass line. Thus, only the $K^+$ mass line was visible in these spectra. Because the triggering ion signal was not recorded completely due to minor electronics delays, it is impossible for these numerous spectra to estimate their actual $Na^+/K^+$ peak amplitude ratios. If this is really the case, there will be no way to identify these spectra. Alternatively, the Na-rich Type 5 spectra could be also hidden in the vast number of unprocessed spectra of the CDA spectral data. In this case, there is a good chance that they will be found in future. Another possible explanation could be an instrumental software bias of the CDA itself. Archetype spectra of Type 5, exhibiting a $Na^+/K^+ \approx 100$ or even more, would consequently display mainly one big, single peak, the mass line of $Na^+$, while the peak of the $K^+$ mass line is hardly existent. This makes it very difficult to identify and unambiguously calibrate these spectra. Compounding this problem, such single-peak spectra were usually discarded by the CDA onboard software, irrespective of their actual abundance. Consequently, very few of them were sent to Earth and the received population of archetype Type 5 spectra is biased by the misleadingly large number of spectra, that exhibit a more potassic composition with two distinct peaks, which were forwarded to earth untroubled. As before with the line-triggered Type 5 spectra, there's no way to solve this issue. To sum up, the observed lower average $Na^+/K^+$ ratio of Type 5 spectra compared to Type 3, could be explained by either the spectra hiding in the data or an instrumental software bias of the CDA data, both causing a misleading lack of Na-rich Type 5 spectra. Second, there's a lack of intermediate spectral types, which represent the transition zone between Type 3 and 5, if they are really related. Such spectra are expected to exhibit peaks of salt-molecule related mass lines (e.g.

$Na^+[NaOH]$ or $Na^+[NaCl]$) with distinctly reduced amplitudes, compared to those in Type 3 spectra, but still with clearly higher amplitudes than the minor peaks in Type 5 spectra. However, no spectra have been found so far that clearly fit in between the two endmembers. This may be due to multiple reasons for this lack: the transformation could happen abruptly and no intermediate types exist at all, or these spectra are still hidden in the wealth of returned data and need further scanning for identification.

# E. Compositional mapping of the E-ring

## 1. Introduction

As previously reported, much work has already been invested into analyses of the chemical and physical properties of E-ring dust particles. From the compositions of E-ring particles, conditions within Enceladus have been revealed, for example the presence of salts within the ice particles (Postberg et al., 2009) as well as nano-silica (Hsu et al., 2015), or a complex organic chemistry (Postberg et al., 2018a, Khawaja et al., 2019), all strongly support the picture of a sub-surface ocean with hydrothermal interaction, deep within Enceladus. The work presented in this chapter will build upon these findings and aims to connect basic particle properties, such as composition and size, with their spatial distribution in the E-ring.

To achieve this goal, the chapter is split into separate parts. The first part shows the distribution of ice particles of different composition with respect to the ring's radial and vertical extent. The presented profiles display the relative, spectral frequency of the compositional types of ice particles at different locations in the ring. Part two focuses on particle sizes. The profiles here display the estimated average particle radii of the different compositional types as a function of their distance to Saturn.

# 2. Results

## 2.1 Composition

This section concerns spatial effects on the composition of the E-ring ice dust particles, as recorded by Cassini's CDA. Herein, the E-ring composition will be given by the relative spectral frequencies of the three confirmed spectral types of water ice particles (Types 1-3) as well as the new high salinity type (Type 5). As mentioned in main chapter B (section "SPICE based spectra analysis"), this has been necessary because the absolute number of all dust particles decreases by several orders of magnitude, radially as well as vertically (Fig. 38). Each of the following profiles was made by the method of boxcar analysis (appendix, section "Boxcar analysis") and Equations 3.0 and 3.1 (main chapter B, section "SPICE based spectra analysis").

### 2.1.1 Radial profile

The first step in a multidimensional, compositional analysis of the E-ring is to consider grain variations with respect to the radial distance to Saturn Barycenter (SBC), in the close proximity of the equatorial ring plane (RPL, $z < 0.1\ R_{Saturn}$). As mentioned before, the radial distance to the SBC thus represents the variable parameter here, while the vertical distance to the RPL is fixed to a minimum ($|d_{RPL}| < 0.1\ R_{Saturn}$). Furthermore, it requires filtering out all instrument pointing of more than 25° away from the RPL (vertical) and Dust-RAM (horizontal) to reduce the bias introduced by dynamically exotic dust particle populations. The best results were eventually achieved by merging all data sets to one large file, which was then analyzed as a whole to eventually produce the compositional profile (see Fig. 31). It covers nearly the whole radial range of the E-ring with the best possible accuracy, provided by the large number of included spectra. It allowed the inclusion of more spectra per box than any individual orbit would have, which resulted in error bars of up to ± 2 %. The relative frequency of Type 1 spectra is around 57 % close to 4 $R_{Saturn}$ and rises with increasing radial distance. This increase flattens begins to rapidly flatten at 9 $R_{Saturn}$, at around 76 %, and ultimately reaches approximately 78-79 % at around 12 $R_{Saturn}$. Outside this distance, the relative frequency remains more or less constant, within the limits of the 2 % uncertainty. Type 2 shows a gradual decrease of its relative abundance, followed by a slight recovery. It begins with an abundance of approximately 28 % at ~4 $R_{Saturn}$ and first drops to a plateau of 14-16 % close to 6 $R_{Saturn}$, which spans out to 7 $R_{Saturn}$. Then it drops even further down to a minimum of 6-7 % at around 9 $R_{Saturn}$. Beyond this point the relative frequency of Type 2 spectra increases again slightly to 12-13 % at around 11 $R_{Saturn}$, from where it remains approximately constant. The relative frequency of Type 3 is around 14 % from 4 to 5 $R_{Saturn}$ followed by a distinct increase up to a

maximum of 21-22 % at approximately 6 $R_{Saturn}$. Further outward the relative abundance of Type 3 grains almost continuously, gradually, decreases. First it drops to a level of approximately 16-17 % that spans from 7 to 8 $R_{Saturn}$. Beyond, the relative frequency decreases further down to 9 % at 12 $R_{Saturn}$ and remains on that level further outward. The fourth analyzed type, Type 5, is practically absent within 5 $R_{Saturn}$ (relative frequency < 0.5 %) before it rises a little to around 1% at 6 $R_{Saturn}$. From there it rises significantly, to reach a maximum of nearly 8% between 7.5 and 8 $R_{Saturn}$. Further outward a continuous decrease can be observed down to the 1% level beyond 12 $R_{Saturn}$.

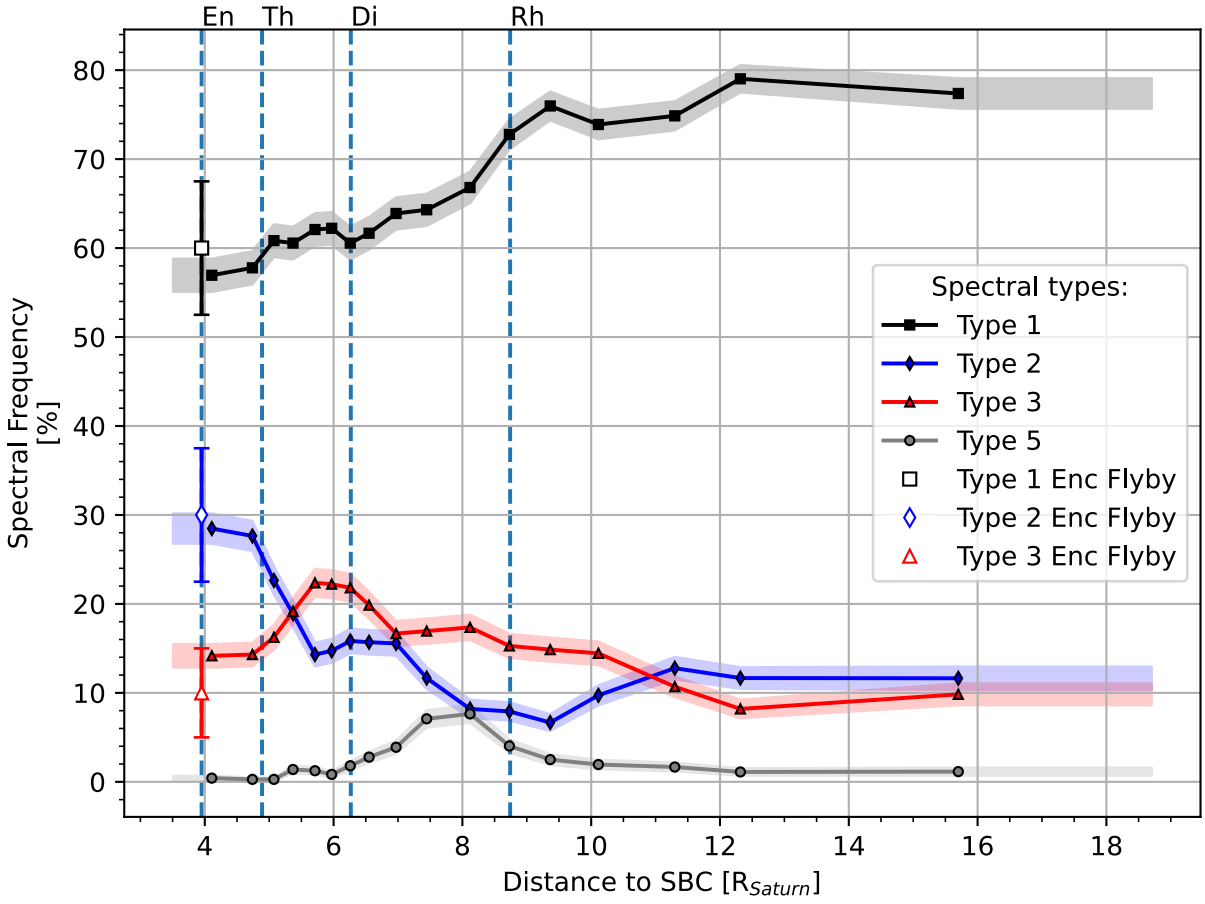


Fig. 31: Radial, compositional profile of all datasets (Table 2) merged to one file. 6393 spectra included in total. Box width: 720 spectra; Step size: 360 spectra. Radial distance to SBC was intertwined with the number of spectra per box (appendix, section "Boxcar analysis"). Vertical distance to RPL < 0.1 $R_{Saturn}$, angular distance of instrument boresight with respect to RPL and Dust-RAM both ≤ 25°. The colored areas to the far left and right of the plots indicate the radial coverage of this analysis. The dashed, vertical lines mark the embedded icy moons' mean orbital distances wrt SBC: Enceladus (En), Tethys (Th), Dione (Di) & Rhea (Rh). The blank symbols represent the relative, spectral frequency of the three main types, recorded next to the Encealdus plume (adapted from Postberg et al., 2011a and 2018b)

Similar to the general, radial, Type 2 frequency distribution, the radial HMOC encounter probability also shows a clear decreasing trend with respect to the radial distance to Saturn (see Fig. 32). From 4 to 8 $R_{Saturn}$ the chance of encountering a Type 2-HMOC within the E-ring population drops from about 2.2 % down to roughly 0.5 %. From there it decreases even further to approximately 0.2 – 0.3 % when reaching 12 $R_{Saturn}$ although this decrease is not significant with respect to the error bars on the points.

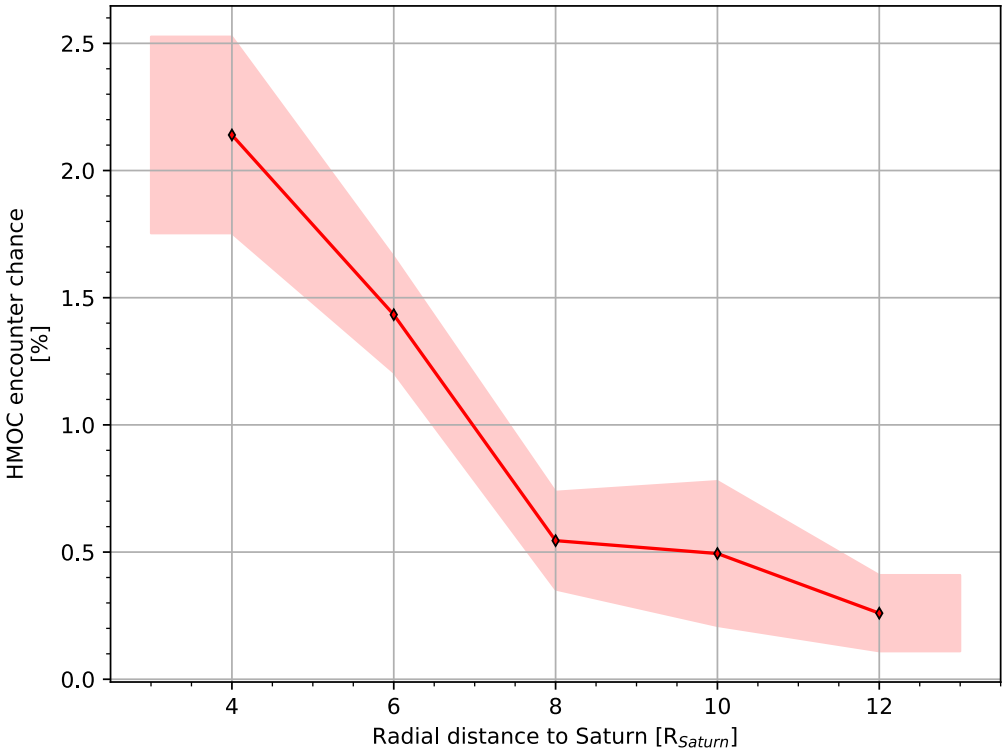


Fig. 32: Radial profile of the encounter chance distribution of the Type 2-HMOC subtype. $P_{encounter}$ [%] = 100 * $n_{HMOC}/n_{tot}$. Each point covers a radial range of ±1 $R_{Saturn}$. Thus, there is no radial overlap. The percentages refer to the total number of spectra in the respective distance range. 7353 spectra included in total. Data adapted from Postberg et al. (2018a).

### 2.1.2 Vertical profile

The next step in such an analysis is to consider variations or trends with respect to the vertical distance from the RPL. Unlike the previous analysis with respect to the radial distance, here the vertical distance to the ring plane (above and below RPL) is now the variable parameter and the radial distance should be held relatively constant. The most obvious option for such analysis is to use the data records of steep E-ring crossings (see Table 3). With a radial distance range of 4.3 to 5.0 $R_{Saturn}$ to SBC at RPX and a vertical distance range of ± 1 $R_{Saturn}$ with respect to RPL, these datasets are eligible for the purpose of a first vertical, compositional E-ring analysis.

As before, directly merging all available data sets to one big file provides the best results for the vertical analysis (see Fig. 33). The vertical profile shows a surprisingly clear, though sightly asymmetric structure. At the outer rims (± 0.8 $R_{Saturn}$ with respect to RPL) Type 1 clearly dominates with frequencies of 73 % and 79 % below and above the ring plane respectively. Type 2 spectra are responsible for 9 % of the total for both locations. Type 3 occurs 17 % of the time below the ring plane and 12 % above the ring plane and 12 % above the ring plane. These two endpoints of the Type 3 frequency range are connected by a relatively flat trend line with a shallow decrease from below to above the ring plane. By comparing the exact numbers of the relative Type 3 frequency at the lowermost (-0.8 $R_{Saturn}$), center (0 $R_{Saturn}$) and uppermost (+0.8 $R_{Saturn}$) parts of the E-ring (17.3 ± 4.2 %, 17.5 ± 2.0 % and 12.3 ± 4.1 %), one can see that there is a constant overlap throughout the whole vertical range, considering their error bars. Thus, the shallow decrease of Type 3 frequency is not statistically significant and could also be described by a mean level of approximately 14-15 %. In contrast to this, Type 1 and 2 follow distinct, complementary trends. Type 1 drops down in relative frequency from about 73 % at -0.8 $R_{Saturn}$ by more than 15 % to approximately 56 % at the ring plane and rises back to 79 % at 0.8 $R_{Saturn}$. Vice versa, Type 2 starts with a relative frequency of about 9 % at -0.8 $R_{Saturn}$, peaks with 26 % at 0 $R_{Saturn}$ and drops back to 9 % at 0.8 $R_{Saturn}$. The error bars for both types are between 3 and 5 % and thus there's no continuous overlap. Compared to the other three types, the relative Type 5 frequency is quite low as one might expect in this E-ring region (< 5 $R_{Saturn}$ from Saturn). Right at the ring plane Type 5 is practically absent, while at the rims the relative frequency apparently rises to 1-2 %. But these higher values have error bars of similar size and thus must be interpreted with caution.

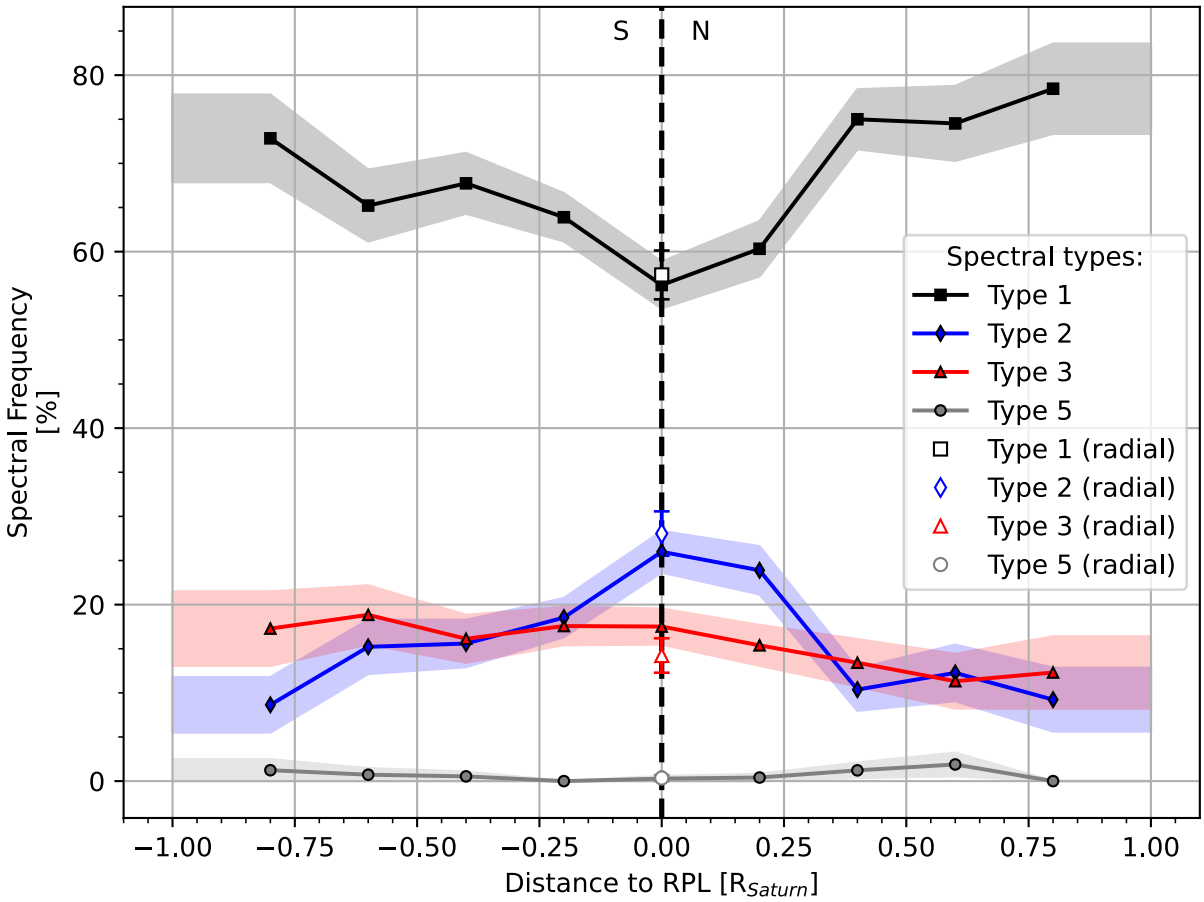


Fig. 33: Bidirectional, vertical profile of the E-ring composition of all datasets (Table 3) merged to one file. 851 spectra included in total. Postive distance values represent the northern hemisphere above the equatorial ring plane (RPL) while negative values cover the southern hemisphere below RPL. The radial distances at the moment of ring plane crossing (RPX) are between 4.3 and 5 $R_{Saturn}$. Blank symbols represent the according type frequencies at the ring plane from the previous radial analysis. The dashed line illustrates the ring plane itself. Box width: 0.4 $R_{Saturn}$; Step size: 0.2 $R_{Saturn}$. Regions beyond ± 1 $R_{Saturn}$ with respect to RPL were cut due to the drastic drop in spectrum numbers.

Aside from that, for all analyzed four spectral types the frequencies of this profile and the numbers, extracted from the radial analysis between 4.5 and 5 $R_{Saturn}$, match quite well right at the ring plane, despite the significant differences in flight trajectory and impact speeds. Since only four datasets were available for this kind of vertical analysis at the time of this work number statistics are not as good as for the radial profiles and local fluctuations may still affect the results. To reduce them it's possible to combine both positive and negative distances to a monodirectional reference, the absolute distance to RPL. The resulting new profile (see Fig. 34) then assumes the ring is vertically symmetric with respect to its compositional distribution, which seems to be applicable at least for Types 1 and 2 (see Fig. 33). As before, Type 1 dominates at the outer edge (0.8 $R_{Saturn}$ from the RPL) at a relative abundance of 75 %. When approaching the ring plane, this decreases with just one plateau at 0.4 $R_{Saturn}$ and reaches 56% at the ring plane. In the case of Type 2, at 0.8 $R_{Saturn}$ just 8 % of the spectra belong to this type

but this number grows with increasing proximity to the ring plane. At 0.4 $R_{Saturn}$ there is a plateau and ultimately reaches a maximum of 26 % of Type 2 spectra at the ring plane. As suggested earlier, the trend line of relative Type 3 frequency approximates an almost flat, constant level of about 15 %. However, as there seems to be a North/South asymmetry (see Fig. 33), this might be misleading.

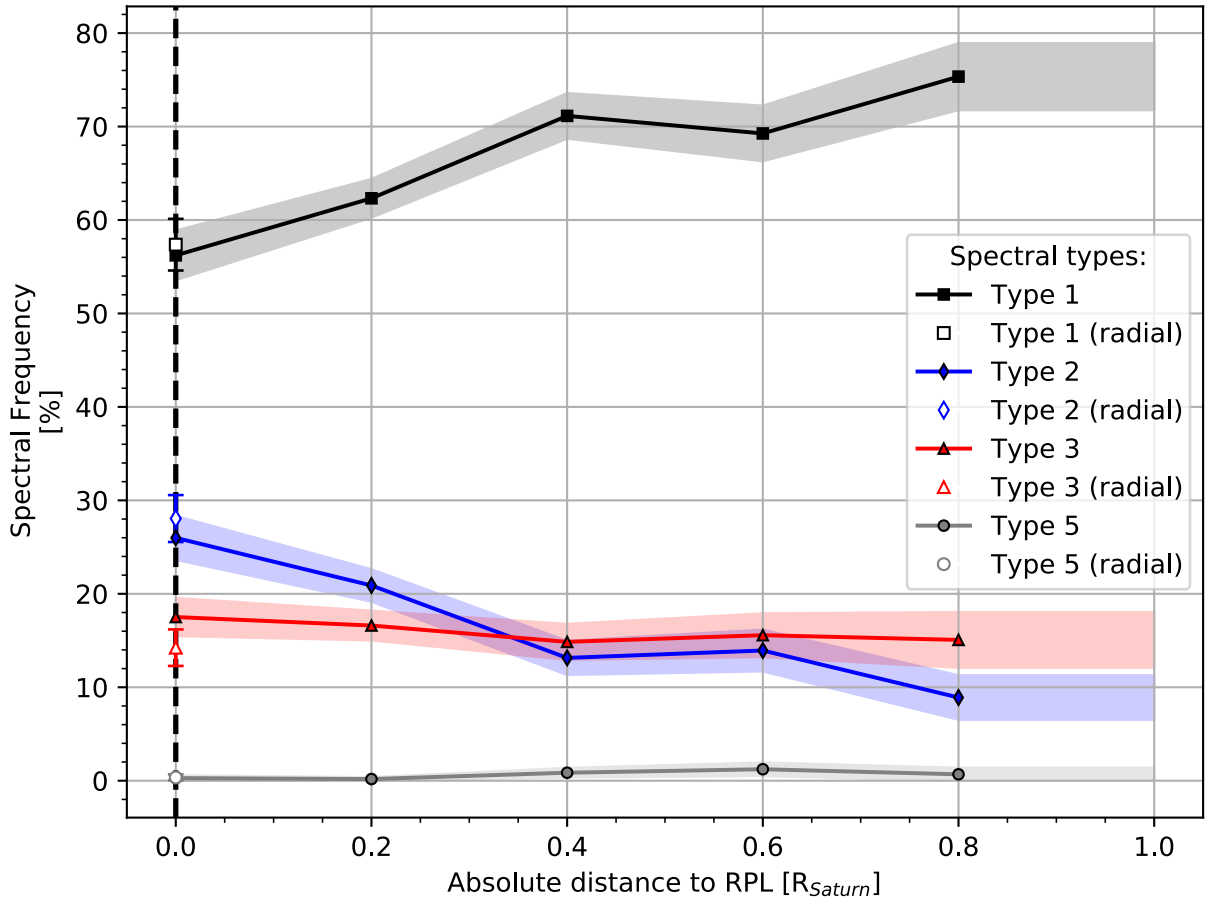


Fig. 34: Monodirectional, vertical profile of the E-ring composition. Selected data and spatial restrictions as before (Table 3). 851 spectra included in total. Blank symbols represent the according type frequencies at the ring plane from the previous radial analysis. The dashed line represents the ring plane. All four datasets merged to one file. Box width: 0.4 $R_{Saturn}$; Step size: 0.2 $R_{Saturn}$. Regions beyond 1 $R_{Saturn}$ with respect to RPL are cut due to the drastic drop in spectrum numbers

## 2.2 Radial size distribution

Using the same boxcar method that was used to determine compositional profiles, the CDA data can also be investigated with respect to the average particle equivalent radius of each compositional type (see Fig. 35). However, compared to the compositional analysis there are some issues (see also chapter B, section "Particle size determination"):

- The applied formula for particle mass determination (Equ. 2.6) was derived from calibration experiments using iron particles and not water ice particles.
- The shape of equation 2.6 results in a high sensitivity to changes in impact speed. To keep this bias to a minimum, the conducted boxcar analysis is exclusively done with data from a relatively narrow impact speed range of 6 to 7 km/s. This window has been chosen because it encompasses the majority of all radial spectral data (~55%) and still covers most of the original, radial distance range of the E-ring (see appendix, section "Radial Kepler-RAM-speed coverage", Fig. 42). The box size is adjusted accordingly.
- The CDA chemical analyzer instrument was sensitive to only a narrow window of particle sizes (in that the spectra were useable) and never the whole size range of E-ring particles. This was due to the aforementioned, limited sensitivity range of the QI channel (see Fig. 22).
- The recorded QI channel amplitude is affected by the particle composition. Thus, all used QI amplitudes must be composition-corrected (see Equ. 2.9). The following values are used for this purpose:
  $k_{comp,\ Type\ 1} = 1$ & $k_{comp,\ Type\ 3} \approx 4$ (Wiederschein et al. 2015)
  $k_{comp,\ Type\ 2} = 1.05$ & $k_{comp,\ Type\ 5} \approx 2$ (see main chapter C)

They are mentioned here again to draw particular attention to them, because the accompanying systematic biases cannot be completely avoided.

Anyway, based on the assumption of spherical particles, for each spectrum a corresponding particle equivalent radius is calculated and then the individual radii are averaged for each box (see Fig. 35). Average radii for each box are calculated as follows:

$$\bar{r}_{Type,box}[\mu m] = \frac{1}{n_{Type}} * \sum_{i=1}^{n_{Type}} r_{i,Type} \qquad (3.4).$$

$r_{i,Type}$ is the individual calculated particle equivalent radius (composition-corrected). The respective error bars are calculated via the SEM:

$$\Delta r_{Type,box}[\mu m] = \frac{1}{n_{Type}} * \sqrt{\sum_{i=1}^{n_{Type}} (\bar{r}_{Type,box} - r_{i,Type})^2} \qquad (3.5)$$

However, this exclusively represents the statistical errors of each box. Because there are still certain systematic errors, the numbers in Fig. 35 represent a first approximation of the inherent uncertainties. A similar size determination procedure for the vertical data could not be performed, as the respective vertical datasets are, individually, relatively homogeneous with respect to their impact speed distribution and do not overlap. Thus, such any meaningful "speed filtering" would remove the majority of the data making the resulting profile very ambiguous.

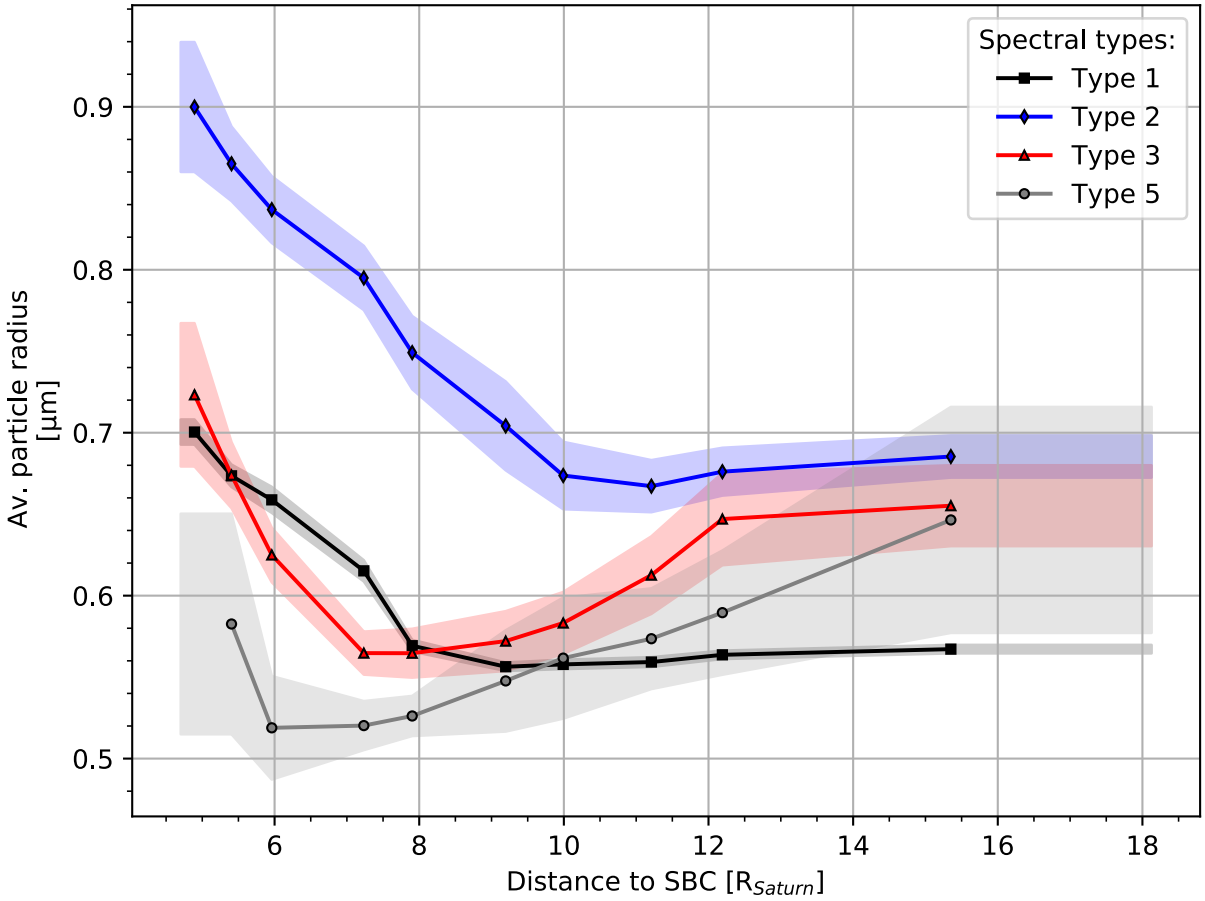


Fig. 35: Radial profile for the average particle radius of all datasets (Table 2) merged to one file. 3543 spectra included in total. Box width: 700 spectra (270 for leftmost box); Step size: 350 spectra (135 for leftmost box). Radial distance to SBC was intertwined with the number of spectra per box (appendix section "Boxcar analysis"). Vertical distance to RPL < 0.1 $R_{Saturn}$; Angular distance of instrument boresight with respect to RPL and Dust-RAM both ≤ 25°; Impact speed: 6-7 km/s; Leftmost box of Type 5 was removed due to containing just one spectrum, causing undefinable error bars.

At first glance one can see that Type 2 particles represent generally the largest particles, while the other three observed types exhibit a more complex pattern. Within the inner third of the analyzed E-ring (< 9 $R_{Saturn}$), Types 1 and 3 are distributed relatively similarly whereas Type 5 is clearly the smallest. Further outwards (> 10 $R_{Saturn}$), the curves of Type 3 and 5 become larger than Type 1, to finally draw near the level of Type 2. Furthermore, it's possible to distinguish two different kinds of trends, visible in the size profiles (see Fig. 35). Types 1 and 2 show distinct, almost linear decreases in size from maxima in the inner E ring at 5 $R_{Saturn}$

towards minima at around 10 to 11 $R_{Saturn}$. This is followed by a subtle increase in size further out. The trends for Types 3 and 5 are marked by a more rapid initial size decrease phase from inward to outward with minima between 7 and 8 $R_{Saturn}$. In contrast to Type 1 and 2, the minimum here is subsequently followed by a distinct, continuous increase when moving to the outer E ring. At the outer boundary of the analysis at about 15 $R_{Saturn}$, the average size of Type 3 and 5 reached a similar level as at the inner boundary at about 5 $R_{Saturn}$.

# 3. Discussion

The previous results clearly lead to the conclusion that the E-ring seems not to be compositionally homogeneous. However, this means there must be certain processes which produce the observed trends. The following section discusses which processes most likely contribute in particular settings.

## 3.1 Radial compositional profile

To begin with, around the mean orbital distance of Enceladus (Fig. 31: leftmost dashed line) the relative, spectral frequencies of the three compositional main types (1-3) inferred in this work, are in good agreement with previous compositional results for the E-ring in the vicinity of the Enceladus' plume (Fig. 31: blank symbols). The latter are based on CDA spectral data, recorded during the close Enceladus flybys E5, E17 and E18 (Postberg et al., 2011a and 2018b) before and after the plume crossings. Back then Type 5 was unknown and thus not considered, which is no surprise when keeping into account its small relative frequency at this location (Fig. 31). This good match of the main types' relative frequencies on one side demonstrates the reliability of both the present and the former compositional results and on the other side it illustrates that the Enceladus plume actively shapes and dominates the E-ring composition around it. The other ice moons within the E-ring are not known to show similar characteristics. For example, CDA data recorded near Rhea show no compositional changes when approaching the moon (Khawaja, 2016).

However, the radial setting is by far more spatially extended than just representing the region around Enceladus' orbit and considers not only the particle composition but also the particle sizes. Since the radial distance to the SBC is likely to correlate most strongly with the particle age (Horanyi et al., 2008; Kempf et al., 2018), it should also reflect the degree of alteration by external processes. Two such processes are known to affect microscopic dust particles: plasma sputtering (e.g. Jurac et al., 2001a+b or Johnson et al., 2008) and photochemical alteration (e.g. Allamandola et al., 1988). While the former acts mainly in a more physical sense (microscopic sandblasting), which lowers particle sizes by erosion, the latter is known for its impact on the particle chemistry. But ultimately how can these two be linked to explain the observed compositional profiles (e.g. Fig. 31)? To start with the three compositional main types (Types 1-3), one should recall the internal, compositional structure of each particle type. As summarized by Cable et al. 2021 (see Fig. 36), these three particle types are suspected to form through different processes below the surface of Enceladus. Type 1 particles most likely represent the direct condensates of $H_2O$ vapor, formed during ascension

of the vapor inside the vents (see Fig. 36, Panel A). Therefore, they exhibit a relatively simple and homogeneous compositional structure. By contrast, Type 3 particles form by flash-freezing of salty ocean water spray, possibly followed by coating with condensing water-vapor (see Fig. 36, Panel C, purple area). The initial spray is produced by bursting gas bubbles in the sub-surface ocean water. However, Type 2 particles can form via both ways, either by vapor condensation similar to Type 1 or by heterogenous nucleation like Type 3:

1. The vapor is not exclusively made of $H_2O$. Amongst others, it also contains volatile organic compounds (VOC) with relatively low molecular masses (<< 200u) and freezing points and sometimes even increased polarity, for example aldehydes or amines (Khawaja et al., 2019). Due to these properties, such VOCs are capable of easily adsorbing/condensing onto preexisting ice particles in colder parts of the vents (see Fig. 36, red edges & lightly shaded area in all panels). This organic "coating" adds distinct amounts of organic compounds to the composition of the affected particles, transforming them into Type 2 particles.
2. There are also non-volatile organics of relatively high molecular mass and comparably low polarity, for example aliphatic and/or aromatic hydrocarbons. They do neither move into the vapor phase nor dissolve in the water itself but accumulate at the water surface. Similar to Type 3, bubble-bursting aerosolizes them and the resulting droplets then serve as nucleation cores for a subsequent water vapor condensation in the vents to form the final Type 2 particle (see Fig. 36, Panel B purple area). This kind of Type 2 particle carries organic compounds with very high molecular masses, producing spectral signals indicative of high mass organic cations (HMOC; Postberg et al., 2018a).

All Type 2 ice particles, forming either way, can grow larger in mass and size compared to Type 1 (see Table 7 and Fig. 35). They also presumably acquire a more complex core-shell structure. So, in the end, there are multiple differently constructed particle types: one smaller yet homogeneous type of almost pure water ice (Type 1) and several which are larger but internally heterogeneous, enriched in salts and/or organics. Each of these particle types reacts differently to the aforementioned alteration processes by plasma sputtering and photochemistry. First of all, Type 1 particles lack detectable amounts of radiation sensitive compounds, such as organic molecules. Second, since any change of the spectral signals of the salts in Type 3 particles is too minor to be recognizable in CDA spectra, the ice-salt chemistry of Type 3 particles is not expected to change in a major way over a timescale of decades based on photochemical alteration, as discussed later in more detail. Thus, Type 1 and 3 can be

considered to suffer primarily only from physical erosion by plasma sputtering. In contrast, the organic molecules present in Type 2 grains are sensitive to photochemical reactions and thus this process has to be taken into account when considering the evolution of Type 2 grains, in addition to the physical, sputtering processes.

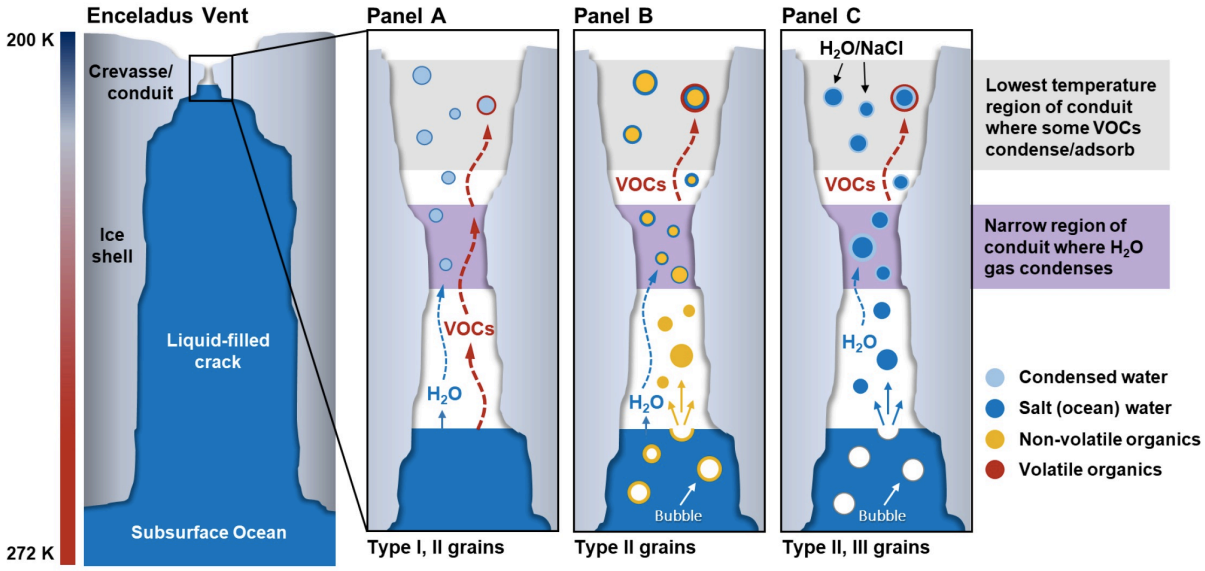


Fig. 36: Scheme of the formation of the three primary ice particle types inside the crack system at the southern polar terrain (Tiger stripes) of Enceladus. Adapted from Cable et al. (2021), itself based on Khawaja et al. (2019). Type 1 is produced from condesation of water vapor (Panel A), whereas Type 3 eclusively forms from flash-freezing of ocean water droplets, produced by bubble brusting, followed by condensation of water vapor (Panel C). Type 2 particles form either from the adsorption/condensation of volatile organics onto other ice particles (Panel A-C) or the condensation of water vapor onto aerosolized, non-volatile organics, also ejected from the ocean via bubble bursting (Panel B).

The compositional profiles within the E-ring (Fig. 31) may be explained by combining knowledge about the particles' internal compositional heterogeneities with their potential reaction to the two alteration processes. The trend line of Type 1 in Fig. 31 clearly shows an increase of the relative frequency relative to the other types with growing distance to SBC and thus with particle lifetime. Based on this observation and the fact that the absolute numbers of all particle types decrease drastically with respect to the radial distance to Saturn (Fig. 38), either the Type 1 particle population must be somehow refreshed from somewhere within the E-ring to compensate this otherwise drastic depletion or the other particle types (Types 2 and 3) vanish even faster due to the plasma sputtering than those of Type 1. The latter is very unlikely since particles of Type 2 and 3 tend to be typically larger than Type 1 particles (see Table 7) and therefore survive the sputter erosion longer (Jurac et al., 2001b). Since impact speed related changes of the spectral appearance would come along with distinct spectral signatures, for example the $Rh^+$ mass line of the target material (Postberg et al., 2009b), which

have not been observed in noticeable numbers, the refreshment theory represents the most likely explanation. But a distinct and well localized source of Type 1 grains apart from Enceladus has not yet been found. Instead, there must be a diffuse source. To identify this source, another look onto the trend line of Type 2 (Fig. 31) can help. The declining trend line of Type 2 mirrors the increasing trend line of Type 1, indicating a link between the two. Hence, a conversion process from Type 2 to Type 1 is proposed here, based on a widespread removal of organic compounds from the icy dust particles, driven by the aforementioned photochemical alteration (Fig. 37). The radial distribution of the Type 2-HMOC encounter chance (Fig. 32) also follows the declining trend of the relative Type 2 frequency. Since this decline mimics the general trend of Type 2 very well, this decline is unlikely to be due to spatial dilution. Thus, there must be an alteration process that effectively reduces the numbers of the Type 2-HMOC subtype, supporting the general picture of a removal of organic-bearing ice particles during particle ageing.

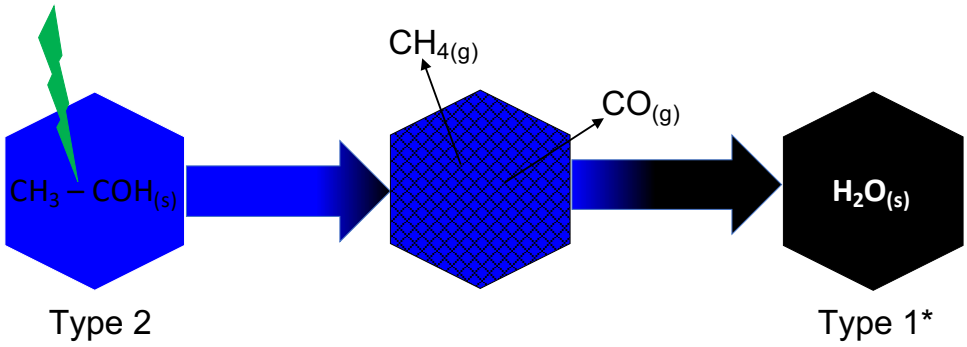


Fig. 37: Schematic showing the process by which photons with sufficient energy cleave entrained organic molecules, producing lower mass, highly volatile fragments which can then outgas from the ice particles. Acetaldehyde is used as an example here, but the process can also occur with other organics suspected to be present in Type 2 grains.

For example, solar UV radiation is easily capable of cleaving the organic molecules carried by the ice particles, into smaller compounds. In general, such small organic molecules are more volatile than the predominant water ice and, due to their small molecular sizes, they are able to escape the particles (Fig. 37). The continuous molecular fragmentation and escaping process produces dust particles with a lowered concentration of organic compounds. Once the concentration of organic compounds drops below the spectral detection threshold of CDA, it becomes impossible to distinguish the formerly organic bearing CDA spectra from Type 1 spectra. The spectral transformation of Type 2 into Type 1 particles could then explain the observed compositional trend lines of Type 1 and 2 particles. For the Type 2-HMOC subtype, it should take longer to remove the large organic molecules compared to the smaller organic molecules in non-HMOC Type 2 particles.

However, Type 3 particles behave different under these conditions. Even after exposure to radiation, the spectral signals of the embedded salts, predominantly of sodium-chloride and -carbonate (Zou, 2021), can be assumed to not change much under UV radiation in the Saturnian environment within the life time of an E-ring grain. Photodissociation and photochemically driven redox reactions for example could possibly result in the transformation of $Cl^-$ to $Cl_2$ and $CO_3^{2-}$ to $CO_2$, which would be then capable of escaping from the particles into space. But the lost anions could then be easily replaced by hydroxide anions ($OH^-$), produced from the water ice. Nevertheless, the sodium remains present in the particles and the resulting CDA spectra are still clearly of Type 3, though with subtle changes in the amplitudes of cluster peaks in the spectra. The size-shrinking plasma sputtering may therefore be the most relevant alteration process for this type of particles. But since Type 3 typically belong to the larger particle fraction and it takes longer for them to be eroded via plasma sputtering (Jurac et al., 2001b). This idea is supported by the fact that the relative frequency of Type 3 does not start to decrease until approximately at the mean orbital distance of Dione at ~6.25 $R_{Saturn}$ from SBC (see vertical, dashed lines in Fig. 31). The observed increase of the Type 3 frequency inside this distance boundary can be addressed to the three types' relative behavior in combination with the used boxcar analysis method and Equ. 3.0: Because Type 2 is affected by both sputter erosion and photochemical conversion to Type 1, it loses relatively more particles than Type 1 and 3 and resulting in this considerable decline of its relative frequency. Type 1 only loses particles to sputter erosion but presumably benefits from a replenishment by former Type 2 grains. Hence, its numbers decrease only slightly and its relative frequency even grows slightly. For Type 3 sputter erosion is also the only relevant process. But because the erosion takes longer due to the larger particle sizes, its numbers decline only slightly as well, producing the relative enrichment. This "enrichment" is however just an apparent effect since the types' absolute particle numbers do not grow in any way.

As discussed already in the preceding main chapter, Type 5 and its radial frequency distribution can be understood as the result of a combination of E-ring particle dynamics and the ongoing plasma sputtering of the salt-rich Type 3 particles in Saturn's magnetosphere. Thus, they fit very well in a picture of ongoing particle transformation, where Type 2 particles are transformed into Type 1, due to radiation-driven photochemical alteration, and Type 3 transform into Type 5 via plasma sputtering. However, considering the calculated average particle radii (Fig. 35) there is a discrepancy between the calculated values of the average particle radius of this work and the modelled size regimes in Kempf & Beckmann (in preparation). This discrepancy can be attributed to the fact that both approaches include

uncertainties, based on certain assumptions and simplifications. Firstly, different particle shapes or porosities have not been considered in either of the approaches. Secondly, the impact of particle composition was not taken into account by the modeling while the particle size calculations presented here did not consider the fact that Equ. 2.6 was originally elaborated with iron particles and later used for water ice particles. Thus, it is perhaps no surprise that the exact values of both approaches differ significantly, though one describes the possible effects of the other.

So how is it possible to connect all of the discussed approaches with the observed radial size distributions (Fig. 35)? The observed similarities between the distributions of Type 1 and Type 2, the salt-poor, on one side and Type 3 and Type 5, supposedly salt-enriched, on the other side clearly support the idea of particle transformation within the E-ring. Furthermore, the obvious difference between these two trends implies that two different processes are indeed responsible. The general decrease of the average particle radii within 6 – 10 $R_{Saturn}$ points at the preferred disappearance of larger particles in this region and/or the additional production of smaller ones, both of which are explicable by plasma sputtering. But why do Type 3 and Type 5 actually show such distinct growth at larger distances to SBC compared to Types 1 and 2? Several scenarios could be possible:

*Dynamical removal:* The presence of relatively more smaller dust particles within this region, causing the minima of the calculated average particles radii in this region, could be produced based on the erosion of larger particles by plasma sputtering in connection with prolonged residence times in this region due to the dynamical barrier of the "storage ring" (see main chapter D, "Discussion"). But without any further constraints this should affect all particle types the same way and thus result in more or less similarly shaped size distributions, which is not the case according to Fig. 35. However, Misra et al. (2012) showed that salt-rich ice particles might exhibit amplified surface potentials and thus increased surface charges compared to salt-poor ice particles. This effect is particularly clear for the region around the Rhea orbit but there are also indications for it around the Dione orbit, though much less distinct there. Consequently, this effect would cause any salt-rich ice particle (Type 3 and 5) present in this region to become more susceptible to the different electro-magnetic forces acting around Saturn. Taking into account that smaller, lighter particles are generally more responsive to perturbation forces which disturb their trajectories compared to larger, heavier particles (Kempf et al., 2018), this could mean that in the region between the orbits of Dione and Rhea smaller representatives of salt-rich ice particles (Type 3 and 5) start to experience changes of their trajectories, for example with respect to orbital eccentricity or the semi-major axis. Such differing trajectories make

smaller particles on one side harder to detect and identify with the CDA instrument and on the other side they are more likely to collide with one of the moons or even the main rings of Saturn. In both cases the small, salt-rich ice particle are removed from the instrumental perception and thus missing in the CDA data of the outer regions of the E-ring, resulting in the increasing trends of the average particle radii towards the outermost regions of the E-ring.

*Error in the impact speed determination:* An under-/overestimated speed causes in return an over-/underestimated particle mass and thus size, due to the reverse correlation in Equ. 2.6. But such an issue should affect again all particle types the same way irrespective of their composition and not just the salty types.

*Unknown instrumental bias:* For example, contamination of the Rhodium target with salts, instrumental dead time in certain regions of the E-ring due to high dust density or trigger issues might play a crucial role. But as before, these issues are not composition-dependent and thus not very likely to be the cause.

However, since this issue can't be ultimately clarified based on the available data, it has to be addressed in future work.

## 3.2 Vertical compositional profile

Although spatially much more confined compared to the radial profile, the vertical profile still conveys important information about the E-ring structure. First of all, Type 3 particles are confirmed to be detectable at vertical distances of up to approximately ±1 $R_{Saturn}$ with respect to the equatorial ring plane (RPL). This confirms the vertical extent of the E-ring, as already reported by CDA observations (see Fig. 38) but without the corresponding analysis of particle compositions. Moreover, the observed vertical distribution of Type 3 particles, which clearly originate from Enceladus (Postberg et al., 2009a and 2011a), gives another strong argument that the particles in these extended E-ring regions mostly stem from Enceladus's subsurface instead of a different source.

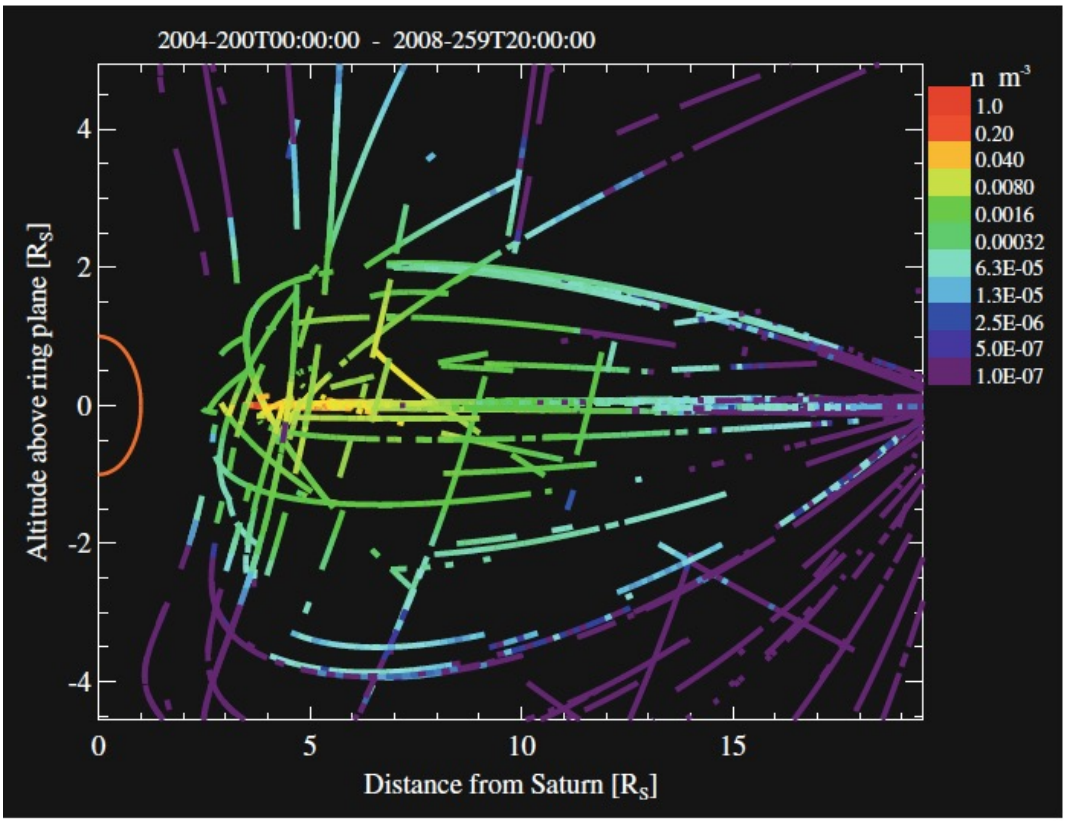


Fig. 38: Spatial particle density map of the E-ring, recorded by Cassini's CDA instrument. From Srama et al. 2011. Note that the number densities go down by several orders of magnitude when going from the inner to the outer E-ring or leaving the ring plane in vertical direction.

The second, perhaps even more relevant information, is the surprisingly distinct, vertical, compositional stratification of the E-ring (see Fig. 33), though earlier work (Khawaja, 2016) reported no clear compositional stratification of the E-ring near Rhea. So what produces this stratification? Kempf et al. (2010) showed that, after being ejected through the cryo-volcanoes at the moon's south polar terrain and leaving its Hill Sphere, particles of a given size

achieve a distinct speed component perpendicular to the ring plane, if their ejection velocity exceeds a certain level. According to Schmidt et al. (2008) the ejection velocity and particle size correlate inversely. Thus, smaller and therefore lighter particles, predominantly of Type 1 (Table 7), are more often ejected at faster speeds – with a corresponding higher velocity component perpendicular to the ring plane – than larger, heavier particles, predominantly of Types 2 or 3 (Table 7). Therefore, the orbits of smaller particles can be expected to reach larger, vertical distances with respect to the ring plane, while the orbits of larger particles should be mostly confined to the proximity of the ring plane. This idea is supported by the results of Horanyi et al. (2008). They modeled the spatial particle density distribution in the E-ring (Fig. 39) and its results show that small particles ($r < 0.5$ μm) distribute fairly widely and should be observable throughout the whole E-ring. Vice versa, moderately sized ($r = 0.5 – 1$ μm) and big particles ($r = 1 – 3$ μm) should be better confined to the ring plane at radial distances of up to Rhea's mean orbital distance and less. Comparing these modeling results with the results of this work (Fig. 33), they seem to be in good agreement. Particles of Type 1 and 5, typically smaller than those of Type 2 and 3 (see Table 7), exhibit their frequency maxima at high vertical distances ($\pm$ 0.8 $R_{Saturn}$ from the RPL). Type 2 grains near the ring plane. The vertical frequency distribution of Type 3 particles is surprisingly flat and does not show any distinct accumulation. The reason for this is currently unknown but will be addressed in future work. However, it should also be mentioned here that, since there are currently no size estimates available for this vertical analysis, it is possible that there are similar discrepancies with respect to the particle size ranges between the results of this work and the modeling results of Horanyi et al. (2008), as previously discussed for the work of Kempf & Beckmann (in preparation). Another ambiguity may be introduced by the unknown, true orbital parameters of the detected particles. But as mentioned previously, in main chapter B (section "Data"), interferences between radial and vertical contributions cannot be avoided completely.

Thirdly, there are indications of a north-south asymmetry (Fig. 33), mostly as variations in the previously described general frequency trends, for example the spike in the Type 1 frequency and the corresponding dip in the Type 2 frequency at 0.4 $R_{Saturn}$ above the RPL. They may be caused by differing positions with respect to the Sun during the CDA sampling periods (see Table 3). It has been previously observed (Hedman et al., 2012) that the Sun has a strong impact onto the vertical thickness and structure of the E-ring, due to the solar radiation pressure. But to ultimately distinguish its contribution it would be necessary to investigate each dataset in Table 3 by itself. This in return would produce significant statistical uncertainties, due to the

particularly low spectrum numbers in some of the used data sets, that very likely mask Sun-driven variations.

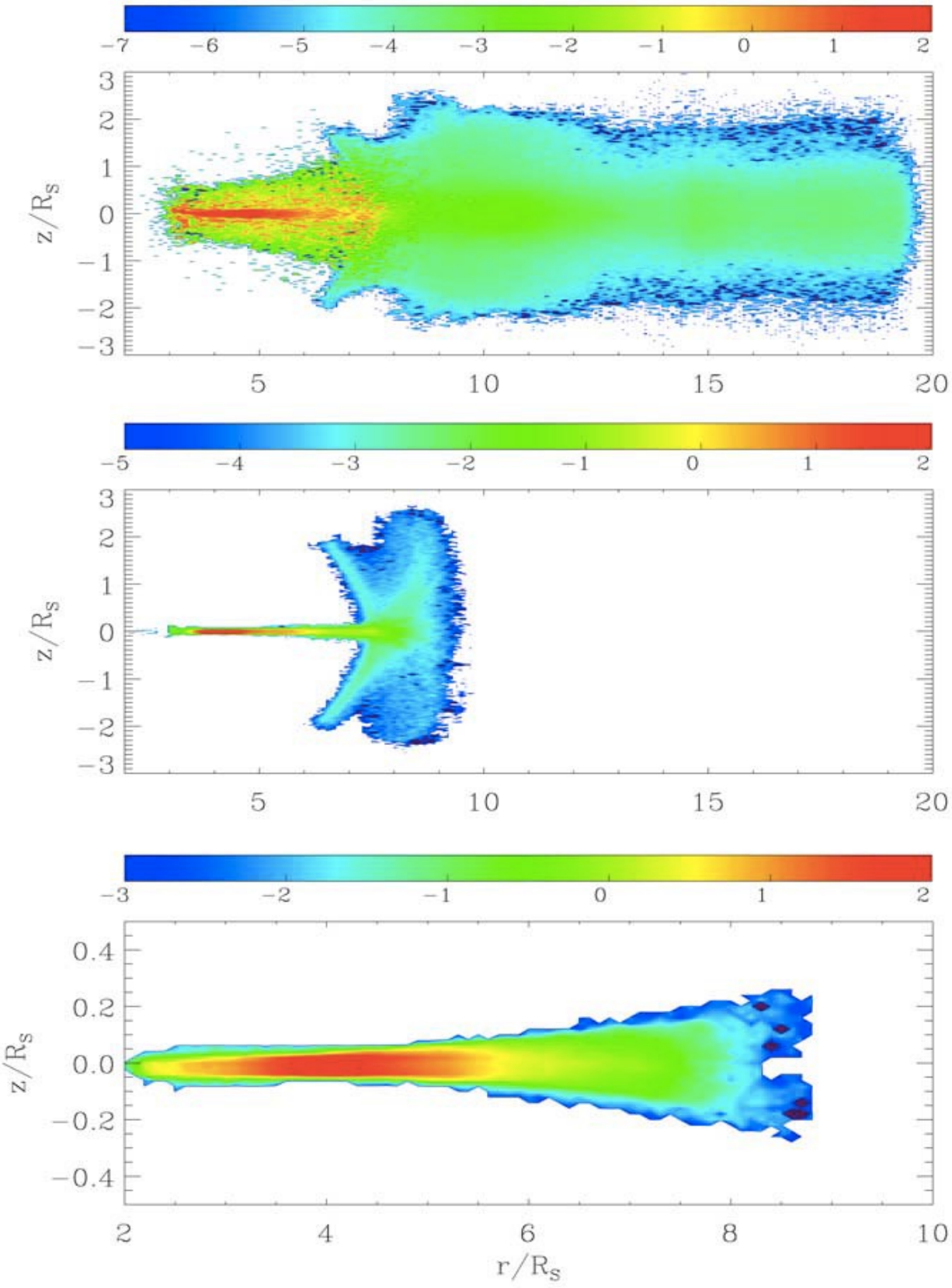


Fig. 39: Simulated, spatial particle distribution for three different particle size regimes. Top: 0.1 – 0.5 µm; Mid: 0.5 – 1.0 µm; Bottom: 1 – 3 µm. From Horanyi et al. (2008)

The radial profile of the average particle radius (see Fig. 35) also shows certain parallels to these modeling results (Fig. 39), but there are also some issues. The moderate and large particle regimes ultimately terminate at around 9 $R_{Saturn}$ with respect to SBC, while the small regime last until 20 $R_{Saturn}$. Furthermore, based on the coloration in the figure, a decrease in particle numbers from 4 to 9 $R_{Saturn}$ is predicted. For comparison, in the radial size profile (Fig. 35) each compositional type except Type 5 shows a distinct decline of its average particle radius distribution, which terminates ultimately between 8 $R_{Saturn}$ (Type 3) and 10 $R_{Saturn}$ (Type 2) from SBC. So, outside this 9 $R_{Saturn}$ boundary, small particles are clearly dominating in both the modeling results as well as the radial profile. But as mentioned before, there are issues that need further clarification. For example, why Type 3 (and Type 5) shows such a rerise of its average particle radius in the outer E-ring, or how can one explain the discrepancy between the size regimes of the modeling (Fig. 39) and the calculated average particle radii (Fig. 35). The former issue has been discussed before but needs further effort in future work. The latter issue could be explained by a biased size determination due to deficiencies in the impact speed determination, the mass-impact speed-QI amplitude calibration formula (Equ. 2.6) or an inaccurate composition correction. However, these cannot be solved with the currently available data and instruments and thus must be addressed in future as well.

# F. Summary and Outlook

## 1. Summary

The main scope of this work is the exploration of the compositional structure of Saturn's large, diffuse E-ring. In this context, Time-of-Flight (TOF) mass spectra of thousands of µm to sub-µm ice particles, which populate the E-ring in vast numbers, have been investigated. The spectra were recorded by the Cosmic Dust Analyzer (CDA), an impact-ionization, TOF mass spectrometer onboard the Cassini-Huygens spacecraft, which orbited the planet Saturn from 2004 to 2017.

Several periods have been selected from this extensive spectral record, based on the orientation of Cassini's trajectory, to account for the enormous spatial extent of the ring. Selections from early 2005 to mid 2006, as well as in spring 2015, which represent periods of spacecraft trajectories at low inclinations, address the radial dimension of the E-ring. The time from late 2006 to late 2008, when Cassini was moving on significantly inclined trajectories, was used to investigate the ring's vertical dimension. All spectra in the selected periods were analyzed for particle composition, as well as the QI channel amplitude, which was then used to estimate particle size. Based on the spatial selection criteria, the spectrum-derived particle properties may then be directly associated with the radial or vertical extent of the E-ring. This ultimately allows radial and vertical profiles of relative particle composition and size to be produced, to study the compositional structure of the E-ring.

Furthermore, laboratory measurements with a LILBID (Laser-Induced Liquid Beam Ion Desorption) time-of-flight mass spectrometer have been conducted as a part of this work. This instrument is capable of mimicking the CDA spectra of different compositional types of ice particles (see Table 1). The goal of the experiments was to determine the effect of composition, especially of organics and salts, onto the ion yield of ice-dominated particles. This information is necessary to achieve a compositionally unbiased particle size determination from the ion yields. Therefore, different test samples, either enriched in polar organic substances of low to moderate molecular masses (based on Khawaja et al., 2019) to mimic Type 2 spectra, or NaCl for Type 3 and 5, have been measured and compared to the well-known reference solution of $10^{-6}$ M NaCl for Type 1 particles (Postberg et al., 2009a; Klenner et al., 2019).

The major results of the work conducted for this thesis are as follows:

## Type 5, a new particle type:

A new compositional type of ice particle has been found in the E-ring, called Type 5. The spectral appearance is characterized by the overwhelming dominance of two mass lines $^{23}Na^+$ (m/z ≈ 23u) and $^{39}K^+$ (m/z ≈ 39u) with similarly high amplitudes. Rare observations of tiny spectral features at masses 63u ($^{23}Na^+[^{23}Na^{16}O^1H]$) and 81u ($^{23}Na^+[^{23}Na^{35}Cl]$) suggest Na- & K-salts in water ice as the basic particle composition. But, to explain the characteristic spectral appearance, the salt concentration must clearly exceed the concentration level proposed for Type 3 particles (Postberg et al., 2009a). The general lack of mass lines characteristic of high impact speeds, e.g. $^{12}C^+$ & $^{103}Rh^+$ (e.g. Postberg et al., 2009b or Fiege et al., 2014), in combination with the increase in the relative abundance of this type of particle in the E-ring at around 8 RSaturn from Saturn, argue for an endogenic E-ring origin. Formation from Type 3 particles via plasma sputtering within an accumulation region dictated by E-ring particle dynamics is capable of explaining both the salty composition as well as providing evidence for accumulation within this E-ring region (see below). But there are still open questions, such as the discrepancy in the $Na^+/K^+$ ratio between Types 3 and 5 or the exact salt concentration level of Type 5 particles, which have to be addressed by future laboratory work.

## Compositional correction of CDA ion yields:

The LILBID experiments showed that the addition of organics for the Type 2 analogue (at concentrations of approx. 0.2 – 1.0 M) increases the ion yield by a factor of ~1.05 compared to the reference, providing the amine concentration is kept below $10^{-3}$ M. For higher amine concentrations this factor seems to decrease to ~1.02. The ion yield factors of salt-rich particles (Type 3 & 5) are even higher. For a Type 3 analogue containing ~0.2 M NaCl the enhancement factor is about 4 (Wiederschein et al., 2015) and for a Type 5 analogue containing ~4 M NaCl this factor is at least 1.3, expected to be extrapolated to a value of 2 when considering the significant amounts of potassium salts in Type 5 grains. However, further testing is needed to verify this value.

## E-ring spatial composition variations:

The compositional results of this work regarding the relative frequencies of the three main particle types 1-3 show a good correlation with previously published compositional results. The relative frequencies of grain types at around 4 $R_{Saturn}$ found in this work almost perfectly agree with the respective numbers given for the E-ring in the near vicinity of

Enceladus by Postberg et al. (2011a & 2018b). These were recorded during targeted, close Enceladus flybys (E5, E17 and E18), which also included deep dives through the cryovolcanic plumes. Thus, the presented results can be taken as reliable.

The E-ring is also found to exhibit distinct radial and vertical variations in both composition and size distribution. Since the number density of E-ring ice grains drastically decreases outside 4 $R_{Saturn}$ and above and below the ring plane, the absolute abundances of all compositional types decrease as well. However, there are interesting variations in the relative frequencies (or percentages) of the compositional types. In both dimensions, Type 1 and 2 particles show opposing trends. Type 1 shows a radial increase in relative frequency from about 60 % to about 80 %, when moving from the inner E-ring to the outer E-ring (>12 $R_{Saturn}$ with respect to Saturn). Similarly, in the vertical dimension, at a Saturnian distance of about 5 $R_{Saturn}$, Type 1 shows an increase of about 20% compared with its relative frequencies at the ring plane and the regions below (-1 $R_{Saturn}$) and above (+1 $R_{Saturn}$) the ring plane. Vice versa, the relative frequency of Type 2 particles decreases radially from about 30% at the innermost E-ring to about 10 % at the outer E-ring. Its relative frequency also decreases in the vertical dimension, by about 15 % from the ring plane to the regions above and below the ring plane. The relative frequency of Type 3 particles shows a more complex pattern. Near Enceladus their abundance is around 10%, and reaches a maximum of almost 25 % at a distance of 6 $R_{Saturn}$ from where the proportion steadily decreases radially outward, reaching levels below 10 % in the outermost E-ring. Vertically, the relative frequency is relatively constant with just a slight indication of asymmetry given by the slightly higher proportion of Type 3 grains below the ring plane. Type 5 is practically absent near Enceladus, increasing to its highest proportion of about 8 % at a Saturnian radial distance of around 8 $R_{Saturn}$. Further outward the relative frequency decreases again to about 1% outside 12 $R_{Saturn}$. As the vertical analysis was based on data from a Saturnian radial distance near 5 $R_{Saturn}$, the abundance of Type 5 particles is too low to make any assessment of vertical variations.

The radial profile of the mean particle radius showed two different types of radial size distributions in the E-ring, with Types 1 and 2 behaving differently to Types 3 and 5. The average sizes of Types 1 and 2 are characterized by a nearly linear decrease in the inner E-ring up to 9 to 10 $R_{Saturn}$, followed by a more or less constant average size. Types 3 and 5 also exhibit this initial decrease but reach a minimum earlier, at 7 to 8 $R_{Saturn}$, followed by surprising distinct increase in average sizes in the outer half of the E-ring. This shape is possibly caused by a loss of smaller salty particles in the outer E-ring induced by particle dynamics, which relatively increases the average particle radius.

These results indicate that certain particle transformations happen in the E-ring, which produce evolved secondary “E-ring ice particles” from primary “Enceladus ice particles”. Types 1 and 2 exhibit opposing frequency trends in both observed spatial dimensions, as well as possess similarly shaped radial profiles of their average particle radii. Thus, it’s very likely that secondary Type 1 particles are formed from Type 2 particles, due to photochemical degradation of their organic compounds. Solar radiation cleaves the initial, relatively large, organic molecules to smaller, more volatile fragments, which more easily escape from the particles. This strips the ice particles of their organic content, making them compositionally indistinguishable from primary Type 1 particles. Evolution may also affect the salt content in the Type 3 grains, with some presumably converting into Type 5 particles via plasma sputtering in Saturn’s magnetosphere. Constant bombardment by ions and electrons acts like a sandblaster, slowly eroding the particles. The removal of water ice relatively increases the salt content and consequently the salt concentration. After exceeding a certain concentration level, the spectral appearance changes and the transformation to Type 5 is accomplished. The aforementioned E-ring particle dynamics provide the opportunity for both particle transformations to act most efficiently in the region between 7 and 9 $R_{Saturn}$. On one hand, in this region occurs a polarity reversal of the particle surface charges (Kempf et al., 2006) and on the other hand there is also the nearby minimum of the V-shaped local electrostatic equilibrium potential (Mitchell et al., 2005). The combined occurrence of both phenomena drastically slows down the outwards migration of many E-ring particles (Kempf & Beckmann, in preparation). The resulting long residence times provide the required time for the particle sputtering and chemical evolution to cause the observed changes in composition and average particle size.

# 2. Outlook

Based on the results of this work, several projects are planned to solve remaining issues and address open questions. An immediate near-term project is a dedicated LILBID experimental campaign for high and very high salt concentrations of both Na- & K-salts. This campaign will focus on the determination of the exact salt concentration level of Type 5 particles as well as the types of salt hidden in these spectra. This will also help to ultimately confirm or contradict the idea of evolved Type 3 grains as the Type 5 source.

A very valuable ongoing project is the automatized compositional classification of all spectra in the CDA data record. With the help of machine learning algorithms, trained using the manually classified spectra of this work, hundreds of thousands of currently unclassified spectra are soon to be revealed. These additional spectra will significantly improve all spectral statistics and additionally provide further candidates for the different compositional types and subtypes (e.g. Khawaja et al., 2019 or Zou, 2021). Following examination of the machine learning results, a more detailed analysis than in this work can be conducted of the compositional alteration of organic material in Type 2 spectra with time, and thus with respect to the radial distance to Saturn. In this way the photochemical degradation will be investigated and the effect of radiation on particle composition should be become clearer.

# G. Appendix

## 1. Boxcar analysis

To produce the presented radial and vertical profiles from the continuously distributed spectral data, the so-called boxcar analysis (BA) method was used. In this method, the spectra are grouped in multiple intervals with respect to a chosen reference parameter (e.g. spacecraft distance to SBC at the moment of detection). These intervals are called boxes and their size, the box width, as well as the distance between two boxes, the step size, are the same for all boxes. The box width must be on one side large enough, that the boxes include as many spectra as possible, to achieve better statistics. But on the other side, the width must be as small as possible to allow as many boxes as possible on the overall range of the reference parameter, to achieve a better spatial resolution. Based on this, too large boxes would apply a strong smoothing effect, that easily erases interesting local structures. Too small boxes might exhibit small numbers of spectra and statistical, small-scale fluctuations become dominant, blurring any sought-after large-scale trends. As the spectra are not evenly distributed with respect to the reference parameter, the final box width is the result of manual testing.

The step size is adjusted to be smaller than the box width to achieve overlapping boxes, with the ratio of step size and box width determining the degree of overlap. The overlap allows to place generally more boxes in the overall range of the reference parameter for a given box width and thus to obtain a better resolved/smoother image of trends in the data than for boxes directly bordering each other. Depending on the degree of overlap the emphasis of the analysis can be put either on local variations or large-scale trends, with a higher degree favoring the former and a minor degree favoring the latter. To achieve a reasonable compromise between both sides, the overlap was always set to 50% or 0.5 in this work, for example a box width of 1 $R_{Saturn}$ means a step size of 0.5 $R_{Saturn}$. Thus, the resulting step size is half the box width. All spectra located within one box are analyzed with respect to the desired analysis parameter (e.g. relative spectrum frequency), producing an average value for this box. After this was done for each box, the resulting values are arranged in a diagram based on the according box locations on the reference parameter scale, producing the final profile.

For the radial analyses in this work, an additional modification of this method was applied. Two refence parameters were intertwined to consider and incorporate additional information into the respective profiles. This was achieved by choosing the total number of spectra per box as the primary reference parameter, with the count starting at the spectrum with

the smallest distance to SBC, proceeding towards increasing distances to SBC and finally ending at the largest distance to SBC. Since the spectrum number itself represents a dimensionless, hardly meaningful reference, the mean radial distances to SBC of each box were chosen as the respective box locations. The merge of these two reference parameters (spectrum number and distance to SBC) grants the advantage, that it produces comparable statistics for all boxes but also takes into account the spatial distribution of the spectrum number density. This way regions of higher spectrum number densities generated relatively more boxes than depleted regions, which allowed a more detailed analysis of such denser regions. All plots based on this modified boxcar analysis with intertwined reference parameters are marked accordingly. For the vertical analysis this modification was not used, as there is a well-defined reference point, the ring plane.

## 2. LILBID experimental setup

(Based on Klenner et al. 2019 and 2020a as well as references therein, if not mentioned explicitly otherwise)

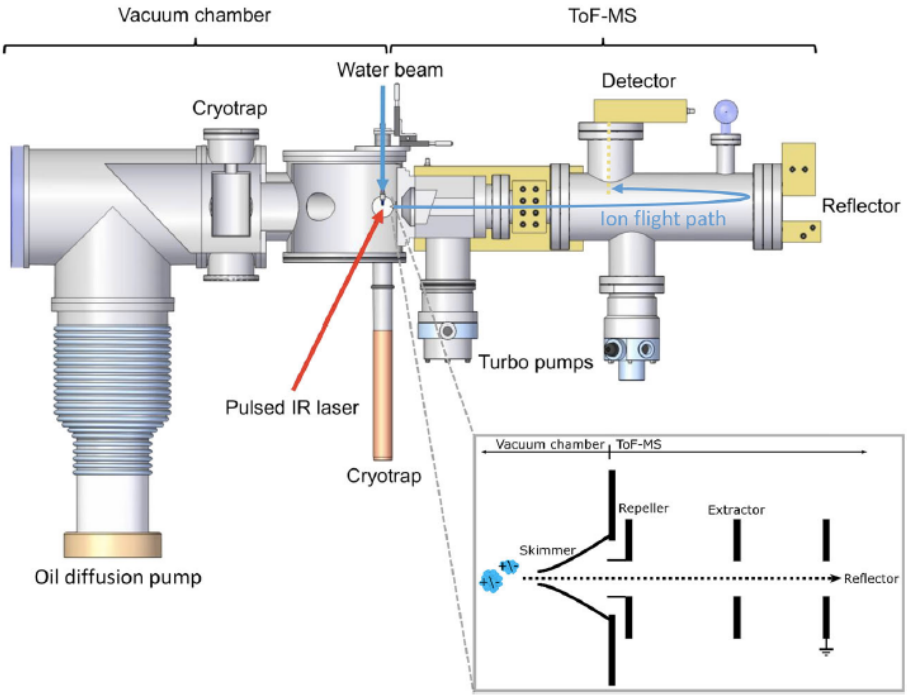


Fig. 40: Scheme of the LILBID instrument, adapted from Klenner et al. (2019)

The instrument consists of two parts (see Fig. 40):

- The vacuum chamber
- The actual Time-of-Flight Mass Spectrometer (Tof-MS)

The aqueous sample solution is injected via an injection valve (model MX9925, Rheodyne) into the vacuum chamber (~5 × $10^{-5}$ mbar) through a quartz nozzle (opening Ø = 16 µm). The nozzle can be adjusted precisely with a three-axis basic frame. An HPLC pump (model 300c, Gynkotek) sustains a constant water flow of 0.17 mL/min. To keep the vacuum constant, excess liquid of the beam is captured by a liquid nitrogen-cooled (lnc) cryotrap, which is located beneath the nozzle (Fig 23). In addition, vaporized liquid and liquid spray are trapped by a second lnc-cryotrap, hanging besides the nozzle in the vacuum chamber (Fig 19). The liquid beam remains stable for about 2mm vertically downward after leaving the nozzle, before it dissipates into droplets. A pulsed, infrared laser (Opolette HE 2731, OPOTEK; 20 Hz, 7 ns pulse length; max power density ≈ 1150 MW/cm$^2$) is used to disperse the stable water beam section. It is set to operate at a wavelength of 2840 nm, to fit together with the absorption frequency of the O-H stretch vibration in water molecules, and a variable pulse energy of up to 4 mJ. The laser beam is directed and focused onto the water beam by an arrangement of one moveable $CaF_2$ lense, a gold mirror and a second $CaF_2$ lense, which is integrated in the window to the vacuum chamber wall.

Once the laser hits the water beam, the water absorbs the laser energy, immediately heats up and explosively dissipates into atomic, molecular and macroscopic fragments, both of ionic and neutral nature. Some of these particles fly through the skimmer, which connects the vacuum chamber and the ToF-MS section. The skimmer serves as a momentum separator, producing a better-collimated particle stream and furthermore as a vacuum separator, which hinders the lower vacuum in the ToF-MS ($10^{-7}$ mbar) to unintendedly equilibrate with the higher vacuum in the actual vacuum chamber. The ToF-MS is a reflectron-type time-of-flight mass spectrometer (Mamyrin, 1993), built by the company Kaesdorf. It uses the principle of delayed extraction (see small rectangle in Fig 19; Charvat & Abel, 2007) and can be tuned to analyze either cations or anions. Since this work is related to CA subsystem of the CDA, only the cation mode is used.

After passing the skimmer the particles arrive in the extraction region and have passed a field-free drift length of ~2.5 cm. Due to varying initial velocities, they arrive at different times. The arrival time is related to the particle mass and the energy transferred by the laser pulse ($t \sim \frac{1}{v_{in}} \sim \frac{m}{E_{Laser}}$). The latter is determined by both the maximum applied power density as well as the distance away from the location of maximum power density along and through the water beam. Within the extraction region, the variation of the initial velocity is decreased by the resulting difference in proximity to the extraction electrodes. Fast particles have already passed through relatively more of the extraction region before the electrodes (Fig. 40: repeller

and extractor) are charged. This way faster ion particles are subject to proportional less acceleration than slow ones, as soon as the extraction electrodes are switched on.

The extraction electrodes of the spectrometer are charged after a given delay time to accelerate all present ion particles to the actual mass spectrometer. This charged status is kept for 30 µs. Ion particles, that arrive too late in the extraction region, are stopped by the repeller electrode because of the applied potential. Therefore, by setting a certain delay time, this gated system picks ion particles based on their initial velocity, which allows to reproduce different impact speed regimes of CDA spectra ($t_{delay} \sim \frac{1}{v_{imp,CDA}}$). The delay time can be tuned with a pulse generator (model DG 535, Stanford Research Systems). The signals of the subsequently arriving ion particles are detected (Photonis Chevron MCP-Set), amplified (Preamp 100, Kaesdorf) and finally digitized (12 bit, Acqiris). The record is managed with LabVIEW. The final mass spectrum represents the average of several hundreds of individual spectra. Each individual spectrum again represents the ion particles produced from one single laser pulse. Thus, it requires a sample volume of ~0.5 mL to produce, collect and add enough individual spectra. Aqueous solutions of NaCl ($10^{-6}$ M) are used both as reference sample as well as base for all test sample solutions. All solutions are freshly prepared with doubly distilled and deionized water (18.2 MΩ “Milli-Q”).

# 3. LILBID measurement settings

Table 8-1: Part 1 of instrument settings of the LILBID measurements

| **Day** | **2019-11-19** | | **2019-11-20** | | | | | |
|---|---|---|---|---|---|---|---|---|
| **Solution** | NaCl $10^{-6}$ M | Mix A-1.0 | NaCl $10^{-6}$ M | Mix A-1.1 | Mix A-2.0 | Mix B-1st | Mix B-2nd | Mix C |
| **Laser intensity [%]** | 99.2/96.9/93.1 | | 99.2/96.9/93.1 | | | | | |
| **Flashlamp energy [J]** | 5.4 | | 5.4 | | | | | |
| **Energy density [MW/cm^2]** | 1152 | | 1152 | | | | | |
| **Delay times [µs]** | 5.3/6.2/6.8 | | 5.3/6.3/6.9 | | | | | |
| **MCP voltage [kV]** | 1.51 | | 1.52 | | | | | |
| **Laser wavelength [nm]** | 2840 | | 2840 | | | | | |
| **Nozzle diameter [µm]** | 16 | | 16 | | | | | |
| **Number of spectra** | 489/489/488 | 485/482/491 | 491/482/481 | 493/481/491 | 486/488/487 | 483/490/487 | 483/482/490 | 488/482/478 |
| **Mass calibration factor a** | 0,34971 | | 0,34971 | | | | | |
| **Mass calibration factor b** | -0,22661 | | -0,22661 | | | | | |
| **Mass calibration factor c** | 0,39211 | | 0,39211 | | | | | |

Table 8-2: Part 2 of instrument settings of the LILBID measurements

| **Day** | **2019-12-19** | | **2021-04-16** | |
|---|---|---|---|---|
| **Solution** | NaCl $10^{-6}$ M | Mix D | NaCl $10^{-6}$ M | NaCl 4M |
| **Laser intensity [%]** | 99.2/96.9/93.1 | | 100/96.2/92 | |
| **Flashlamp energy [J]** | 5.4 | | 5.35 | |
| **Energy density [MW/cm^2]** | 1152 | | 1152 | |
| **Delay times [µs]** | 5.2/6.3/6.9 | | 4.3/5.5/6.9 | |
| **MCP voltage [kV]** | 1.52 | | 1.20 | |
| **Laser wavelength [nm]** | 2840 | | 2840 | |
| **Nozzle diameter [µm]** | 16 | | 15 | |
| **Number of spectra** | 480/488/488 | 481/484/485 | 150/150/150 | 300/300/300 |
| **Mass calibration factor a** | 0,34971 | | 0.34780 | |
| **Mass calibration factor b** | -0,22661 | | -0.22450 | |
| **Mass calibration factor c** | 0,39211 | | 0.39800 | |

# 4. Ion yield histograms

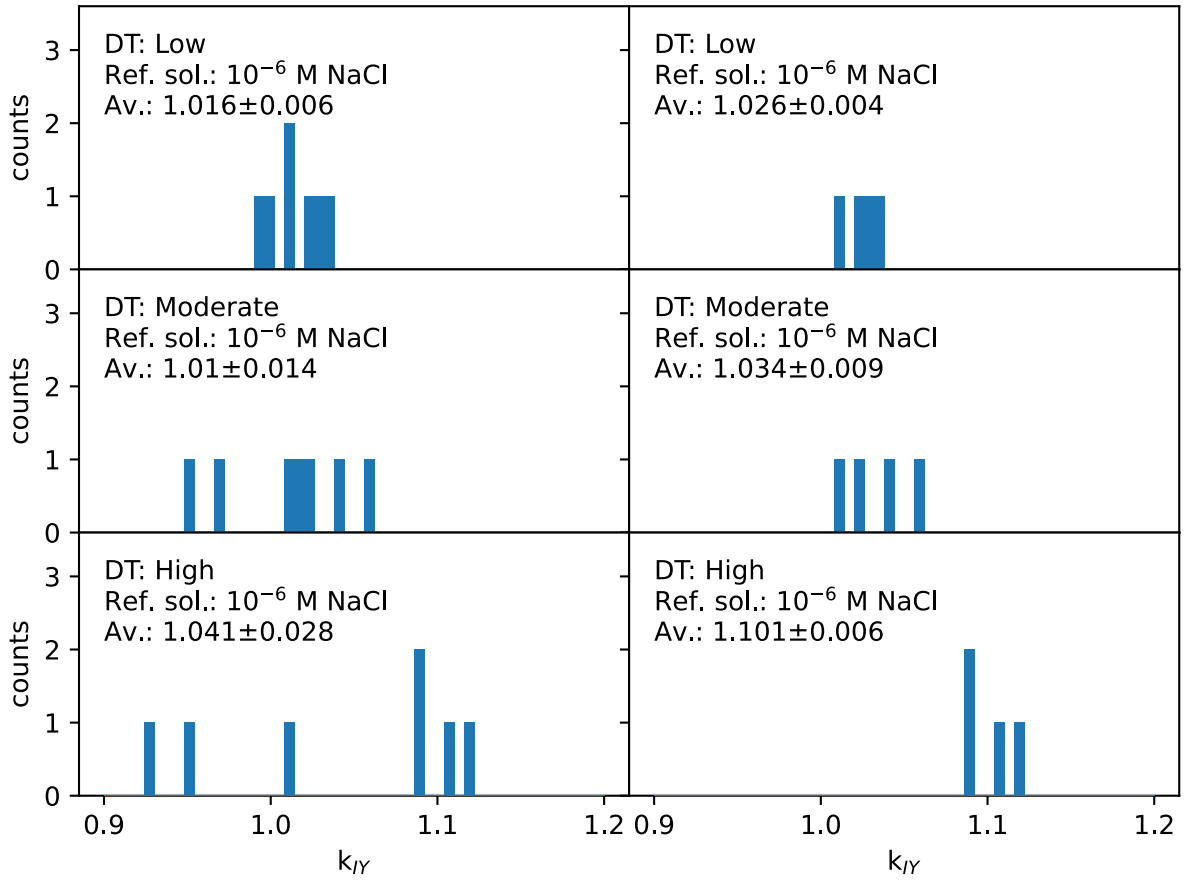


Fig. 41: Histograms for the results of the LILBID ion yield experiments. Left side: unconstrained analysis, including Mix A. Right side: constrained analysis, excluding Mix A.

# 5. Radial Kepler-RAM-speed coverage

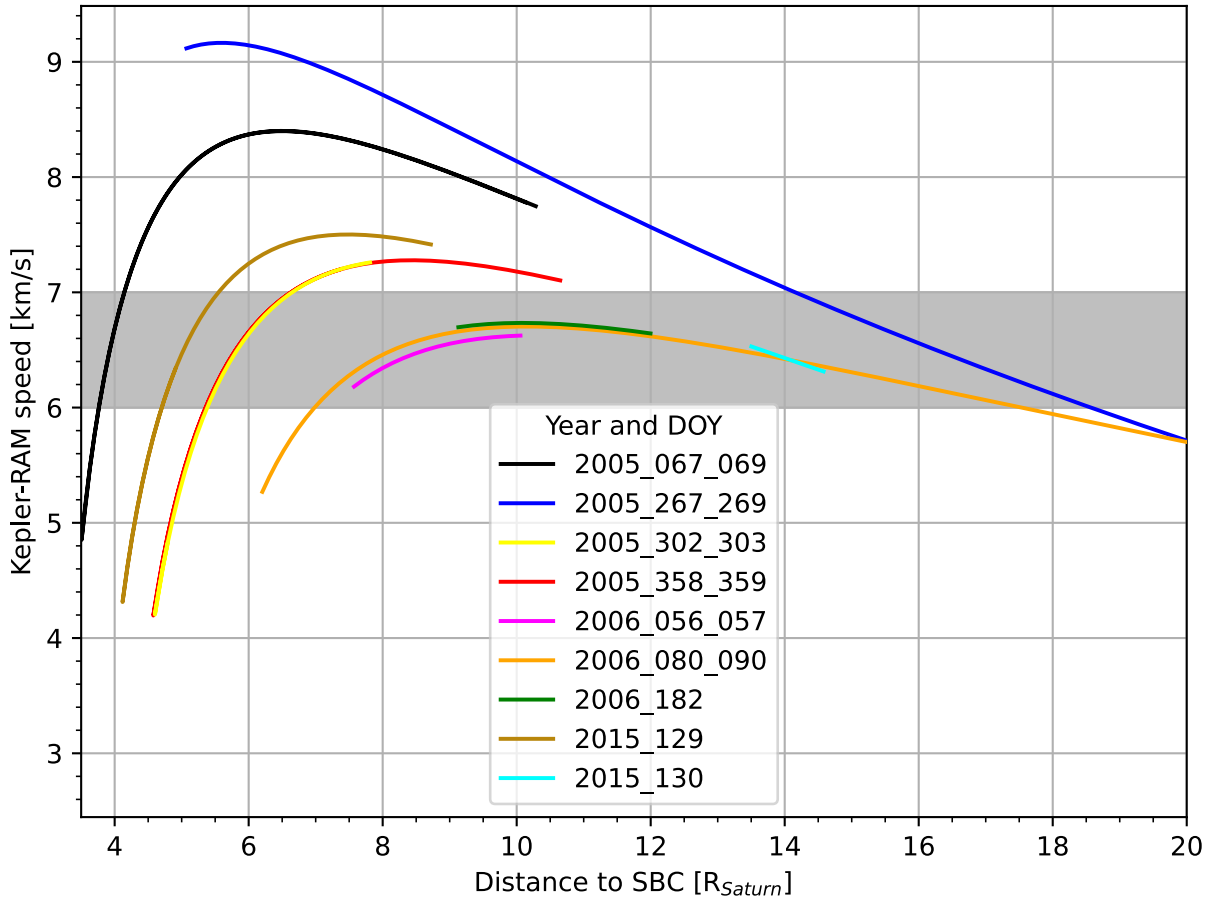


Fig. 42: Radial coverage of the Kepler-RAM impact speed for the used datasets. The grey area represents the speed regime selected for the radial profile of the average particle radii.

# H. Bibliography


Acton, C., Bachman, N., Semenov, B. & Wright, E. (2018). A look towards the future in the handling of space science mission geometry. Planetary and Space Science, 150, 9–12. https://doi.org/10.1016/j.pss.2017.02.013

Acton, C. H. (1996). Ancillary data services of NASA's Navigation and Ancillary Information Facility. Planetary and Space Science, 44(1), 65–70. https://doi.org/10.1016/0032-0633(95)00107-7

Aggarwal, H. R. & Oberbeck, V. R. (1974). Roche Limit of a Solid Body. The Astrophysical Journal, 191, 577. https://doi.org/10.1086/152998

Allamandola, L., Sandford, S. & Valero, G. (1988). Photochemical and thermal evolution of interstellar/precometary ice analogs. Icarus, 76(2), 225–252. https://doi.org/10.1016/0019-1035(88)90070-x

Altobelli, N., Postberg, F., Fiege, K., Trieloff, M., Kimura, H., Sterken, V. J., Hsu, H. W., Hillier, J., Khawaja, N., Moragas-Klostermeyer, G., Blum, J., Burton, M., Srama, R., Kempf, S. & Gruen, E. (2016). Flux and composition of interstellar dust at Saturn from Cassinis Cosmic Dust Analyzer. Science, 352(6283), 312–318. https://doi.org/10.1126/science.aac6397

Annex, A., Pearson, B., Seignovert, B., Carcich, B., Eichhorn, H., Mapel, J., von Forstner, J., McAuliffe, J., del Rio, J., Berry, K., Aye, K. M., Stefko, M., de Val-Borro, M., Kulumani, S. & Murakami, S. Y. (2020). SpiceyPy: a Pythonic Wrapper for the SPICE Toolkit. Journal of Open Source Software, 5(46), 2050. https://doi.org/10.21105/joss.02050

Auer, S., Grün, E., Srama, R., Kempf, S. & Auer, R. (2002). The charge and velocity detector of the cosmic dust analyzer on Cassini. Planetary and Space Science, 50(7–8), 773–779. https://doi.org/10.1016/s0032-0633(02)00019-3

Barabashov, N. P. & Semeikin, B. E. (1933). Monochromatic photometry of Saturn and its rings. Astronomy Reports (Astron. Zh.), 10, 381–389.

Barbosa Aguiar, A. C., Read, P. L., Wordsworth, R. D., Salter, T. & Hiro Yamazaki, Y. (2010). A laboratory model of Saturn's North Polar Hexagon. Icarus, 206(2), 755–763. https://doi.org/10.1016/j.icarus.2009.10.022

Baum, W., Kreidl, T., Westphal, J., Danielson, G., Seidelmann, P., Pascu, D. & Currie, D. (1981). Saturn's E ring. Icarus, 47(1), 84–96. https://doi.org/10.1016/0019-1035(81)90093-2

Bond, G. P. (1850). Discovery of inner dark ring of Saturn Nov. 15, 1850. Monthly Notices of the Royal Astronomical Society, 11(2), 20–21. https://doi.org/10.1093/mnras/11.2.20

Bond, W. C. (1851). On the new ring of Saturn. The Astronomical Journal, 2, 5. https://doi.org/10.1086/100200

Brumfiel, G. (2012). The astronomical unit gets fixed. Nature. https://doi.org/10.1038/nature.2012.11416

Buratti, B. J., Thomas, P. C., Roussos, E., Howett, C., Seiß, M., Hendrix, A. R., Helfenstein, P., Brown, R. H., Clark, R. N., Denk, T., Filacchione, G., Hoffmann, H., Jones, G. H., Khawaja, N., Kollmann, P., Krupp, N., Lunine, J., Momary, T. W., Paranicas, C., . . . Soderblom, L. A. (2019). Close Cassini flybys of Saturn's ring moons Pan, Daphnis, Atlas, Pandora, and Epimetheus. Science, 364(6445). https://doi.org/10.1126/science.aat2349

Cable, M. L., Porco, C., Glein, C. R., German, C. R., MacKenzie, S. M., Neveu, M., Hoehler, T. M., Hofmann, A. E., Hendrix, A. R., Eigenbrode, J., Postberg, F., Spilker, L. J., McEwen, A., Khawaja, N., Hunter Waite, J., Wurz, P., Helbert, J., Anbar, A., de Vera, J. P. & Núñez, J. (2021). The Science Case for a Return to Enceladus. The Planetary Science Journal, 2(4), 132. https://doi.org/10.3847/psj/abfb7a

Canup, R. M. & Righter, K. (2000). ORIGIN OF THE EARTH AND MOON (2nd ed.). The University of Arizona Press.

Cassini, G. D. (1685). Découverte de la lumière celeste qui paroist dans le zodiaque. A Paris: de l'lmprimerie royale, par Sebastien Mabre-Cramoisy (ETH-Bibliothek Zürich), 1–68.

Charvat, A. & Abel, B. (2007). How to make big molecules fly out of liquid water: applications, features and physics of laser assisted liquid phase dispersion mass spectrometry. Physical Chemistry Chemical Physics, 9(26), 3335. https://doi.org/10.1039/b615114k

Conrath, B. J., Gautier, D., Hanel, R. A. & Hornstein, J. S. (1984). The helium abundance of Saturn from Voyager measurements. The Astrophysical Journal, 282, 807. https://doi.org/10.1086/162267

Courtin, R., Gautier, D., Marten, A., Bezard, B. & Hanel, R. (1984). The composition of Saturn's atmosphere at northern temperate latitudes from Voyager IRIS spectra - NH3, PH3, C2H2, C2H6, CH3D, CH4, and the Saturnian D/H isotopic ratio. The Astrophysical Journal, 287, 899. https://doi.org/10.1086/162748

D'Angelo, G. & Podolak, M. (2015). CAPTURE AND EVOLUTION OF PLANETESIMALS IN CIRCUMJOVIAN DISKS. The Astrophysical Journal, 806(2), 203. https://doi.org/10.1088/0004-637x/806/2/203

de Pater, I., Martin, S. C. & Showalter, M. R. (2004). Keck near-infrared observations of Saturn's E and G rings during Earth's ring plane crossing in August 1995. Icarus, 172(2), 446–454. https://doi.org/10.1016/j.icarus.2004.07.012

de Pater, I., Showalter, M. R., Burns, J. A., Nicholson, P. D., Liu, M. C., Hamilton, D. P. & Graham, J. R. (1999). Keck Infrared Observations of Jupiter's Ring System near Earth's 1997 Ring Plane Crossing. Icarus, 138(2), 214–223. https://doi.org/10.1006/icar.1998.6068

de Pater, I., Showalter, M. R., Lissauer, J. J. & Graham, J. R. (1996). Keck Infrared Observations of Saturn's E and G Rings during Earth's 1995 Ring Plane Crossings. Icarus, 121(1), 195–198. https://doi.org/10.1006/icar.1996.0078

Denk, T. & Mottola, S. (2019). Studies of irregular satellites: I. Lightcurves and rotation periods of 25 Saturnian moons from Cassini observations. Icarus, 322, 80–102. https://doi.org/10.1016/j.icarus.2018.12.040

Dikarev, V. V. (1999). Dynamics of particles in Saturn's E ring: Effects of charge variations and the plasma drag force. Astronomy and Astrophysics, 346, 1011–1019. https://ui.adsabs.harvard.edu/abs/1999A&A. . .346.1011D

Dollfus, A. & Brunier, S. (1982). Observation and photometry of an outer ring of saturn. Icarus, 49(2), 194–204. https://doi.org/10.1016/0019-1035(82)90071-9

Dougherty, M. K., Khurana, K. K., Neubauer, F. M., Russell, C. T., Saur, J., Leisnerand, J. S. & Burton, M. E. (2006). Identification of a Dynamic Atmosphere at Enceladus with the Cassini Magnetometer. Science, 311(5766), 1406–1409. https://doi.org/10.1126/science.1120985

Draine, B. (2003). Interstellar Dust Grains. Annual Review of Astronomy and Astrophysics, 41(1), 241–289. https://doi.org/10.1146/annurev.astro.41.011802.094840

FEIBELMAN, W. A. (1967). Concerning the "D" Ring of Saturn. Nature, 214(5090), 793–794. https://doi.org/10.1038/214793a0

Fiege, K. (2013). Compositional Analysis of Interstellar Dust as seen by the Cassini Cosmic Dust Analyzer (Dissertation). Ruprecht Karls Universität Heidelberg.

Fiege, K., Trieloff, M., Hillier, J. K., Guglielmino, M., Postberg, F., Srama, R., Kempf, S. & Blum, J. (2014). Calibration of relative sensitivity factors for impact ionization detectors with high-velocity silicate microparticles. Icarus, 241, 336–345. https://doi.org/10.1016/j.icarus.2014.07.015

Fielding, L. A., Hillier, J. K., Burchell, M. J. & Armes, S. P. (2015). Space science applications for conducting polymer particles: synthetic mimics for cosmic dust and micrometeorites. Chemical Communications, 51(95), 16886–16899. https://doi.org/10.1039/c5cc07405c

Fortney, J. J. & Nettelmann, N. (2009). The Interior Structure, Composition, and Evolution of Giant Planets. Space Science Reviews, 152(1–4), 423–447. https://doi.org/10.1007/s11214-009-9582-x

Friichtenicht, J. F., Roy, N. L. & Becker, D. G. (1971). The Cosmic Dust Analyzer: Experimental Evaluation of an Impact Ionization Model. International Astronomical Union Colloquium, 13, 299–310. https://doi.org/10.1017/s0252921100049216

Friichtenicht, J. F., Slattery, J. C., United States. National Aeronautics and Space Administration & Space Technology Laboratories. (1963). Ionization Associated with Hypervelocity Impact. National Aeronautics and Space Administration.

GEHRELS, T., BAKER, L. R., BESHORE, E., BLENMAN, C., BURKE, J. J., CASTILLO, N. D., DACOSTA, B., DEGEWIJ, J., DOOSE, L. R., FOUNTAIN, J. W., GOTOBED, J., KENKNIGHT, C. E., KINGSTON, R., MCLAUGHLIN, G., MCMILLAN, R., MURPHY, R., SMITH, P. H., STOLL, C. P., STRICKLAND, R. N., . . . ESPOSITO, L. (1980). Imaging Photopolarimeter on Pioneer Saturn. Science, 207(4429), 434–439. https://doi.org/10.1126/science.207.4429.434

Godfrey, D. (1988). A hexagonal feature around Saturn's north pole. Icarus, 76(2), 335–356. https://doi.org/10.1016/0019-1035(88)90075-9

Guerin, P. (1970). The new ring of Saturn. Sky and Telescope, 40, 88.

Guillot, T. (1999). Interiors of Giant Planets Inside and Outside the Solar System. Science, 286(5437), 72–77. https://doi.org/10.1126/science.286.5437.72

Haff, P., Eviatar, A. & Siscoe, G. (1983). Ring and plasma: The enigmae of Enceladus. Icarus, 56(3), 426–438. https://doi.org/10.1016/0019-1035(83)90164-1

Hamilton, D. P., Skrutskie, M. F., Verbiscer, A. J. & Masci, F. J. (2015). Small particles dominate Saturn's Phoebe ring to surprisingly large distances. Nature, 522(7555), 185–187. https://doi.org/10.1038/nature14476

Hansen, C. J., Esposito, L., Stewart, A. I. F., Colwell, J., Hendrix, A., Pryor, W., Shemansky, D. & West, R. (2006). Enceladus' Water Vapor Plume. Science, 311(5766), 1422–1425. https://doi.org/10.1126/science.1121254

Havnes, O., Morfill, G. & Melandsø, F. (1992). Effects of electromagnetic and plasma drag forces on the orbit evolution of dust in planetary magnetospheres. Icarus, 98(1), 141–150. https://doi.org/10.1016/0019-1035(92)90215-s

Hayashi, C. (1981). Structure of the Solar Nebula, Growth and Decay of Magnetic Fields and Effects of Magnetic and Turbulent Viscosities on the Nebula. Progress of Theoretical Physics Supplement, 70, 35–53. https://doi.org/10.1143/ptps.70.35

Hedman, M., Burns, J., Hamilton, D. & Showalter, M. (2012). The three-dimensional structure of Saturn's E ring. Icarus, 217(1), 322–338. https://doi.org/10.1016/j.icarus.2011.11.006

Hedman, M., Murray, C., Cooper, N., Tiscareno, M., Beurle, K., Evans, M. & Burns, J. (2009). Three tenuous rings/arcs for three tiny moons. Icarus, 199(2), 378–386. https://doi.org/10.1016/j.icarus.2008.11.001

Hide, R. (1966). On the circulation of the atmospheres of Jupiter and Saturn. Planetary and Space Science, 14(8), 669–675. https://doi.org/10.1016/0032-0633(66)90099-7

Hillier, J., Green, S., McBride, N., Altobelli, N., Postberg, F., Kempf, S., Schwanethal, J., Srama, R., McDonnell, J. & Grün, E. (2007). (b) Interplanetary dust detected by the Cassini CDA Chemical Analyser. Icarus, 190(2), 643–654. https://doi.org/10.1016/j.icarus.2007.03.024

Hillier, J. K., Fiege, K., Trieloff, M. & Srama, R. (2013). Numerical modelling of mineral impact ionisation spectra. Planetary and Space Science, 89, 159–166. https://doi.org/10.1016/j.pss.2013.08.016

Hillier, J. K., Green, S. F., McBride, N., Schwanethal, J. P., Postberg, F., Srama, R., Kempf, S., Moragas-Klostermeyer, G., McDonnell, J. A. M. & Grun, E. (2007). (a) The composition of Saturn's E ring. Monthly Notices of the Royal Astronomical Society, 377(4), 1588–1596. https://doi.org/10.1111/j.1365-2966.2007.11710.x

Hillier, J. K., Postberg, F., Sestak, S., Srama, R., Kempf, S., Trieloff, M., Sternovsky, Z. & Green, S. F. (2012). Impact ionization mass spectra of anorthite cosmic dust analogue particles. Journal of Geophysical Research: Planets, 117(E9), n/a. https://doi.org/10.1029/2012je004077

Hillier, J. K., Sestak, S., Green, S., Postberg, F., Srama, R. & Trieloff, M. (2009). The production of platinum-coated silicate nanoparticle aggregates for use in hypervelocity impact experiments. Planetary and Space Science, 57(14–15), 2081–2086. https://doi.org/10.1016/j.pss.2009.09.019

Hillier, J. K., Sternovsky, Z., Kempf, S., Trieloff, M., Guglielmino, M., Postberg, F. & Price, M. (2018). Impact ionisation mass spectrometry of platinum-coated olivine and magnesite-dominated cosmic dust analogues. Planetary and Space Science, 156, 96–110. https://doi.org/10.1016/j.pss.2017.10.002

Horányi, M. (2000). Dust streams from Jupiter and Saturn. Physics of Plasmas, 7(10), 3847. https://doi.org/10.1063/1.1288909

Horányi, M., Juhász, A. & Morfill, G. E. (2008). Large-scale structure of Saturn's E-ring. Geophysical Research Letters, 35(4). https://doi.org/10.1029/2007gl032726

Hsu, H. W., Kempf, S., Postberg, F., Trieloff, M., Burton, M., Roy, M., Moragas-Klostermeyer, G. & Srama, R. (2011). (a) Cassini dust stream particle measurements during the first three orbits at Saturn. Journal of Geophysical Research: Space Physics, 116(A8), n/a. https://doi.org/10.1029/2010ja015959

Hsu, H. W., Postberg, F., Kempf, S., Trieloff, M., Burton, M., Roy, M., Moragas-Klostermeyer, G. & Srama, R. (2011). (b) Stream particles as the probe of the dust-plasma-magnetosphere interaction at Saturn. Journal of Geophysical Research: Space Physics, 116(A9), n/a. https://doi.org/10.1029/2011ja016488

Hsu, H. W., Postberg, F., Sekine, Y., Shibuya, T., Kempf, S., Horányi, M., Juhász, A., Altobelli, N., Suzuki, K., Masaki, Y., Kuwatani, T., Tachibana, S., Sirono, S. I., Moragas-Klostermeyer, G. & Srama, R. (2015). Ongoing hydrothermal activities within Enceladus. Nature, 519(7542), 207–210. https://doi.org/10.1038/nature14262

Huygens, C. (1659). Systema saturnium, sive de causis mirandorum saturni phaenomenon, et comite ejus planeta novo. The Hagae-Comitis, 1–84.

Iess, L., Rappaport, N. J., Jacobson, R. A., Racioppa, P., Stevenson, D. J., Tortora, P., Armstrong, J. W. & Asmar, S. W. (2010). Gravity Field, Shape, and Moment of Inertia of Titan. Science, 327(5971), 1367–1369. https://doi.org/10.1126/science.1182583

Johnson, R. E., Famá, M., Liu, M., Baragiola, R. A., Sittler Jr., E. C. & Smith, H. T. (2008). Sputtering of ice grains and icy satellites in Saturn's inner magnetosphere. Planetary and Space Science, 56(9), 1238–1243. https://doi.org/10.1016/j.pss.2008.04.003

Jurac, S., Johnson, R. E. & Richardson, J. D. (2001). (b) Saturn's E Ring and Production of the Neutral Torus. Icarus, 149(2), 384–396. https://doi.org/10.1006/icar.2000.6528

Jurac, S., Johnson, R. E., Richardson, J. D. & Paranicas, C. (2001). (a) Satellite sputtering in Saturn's magnetosphere. Planetary and Space Science, 49(3–4), 319–326. https://doi.org/10.1016/s0032-0633(00)00153-7

Keeler, J. E. (1895). A Spectroscopic Proof of the Meteoric Constitution of Saturn's Rings. The Astrophysical Journal, 1, 416. https://doi.org/10.1086/140074

Kempf, S. (2007). Saturnian Dust: Rings, Ice Volcanoes, and Streams (Habilitation). Technische Universität Carolo-Wilhelmina Braunschweig.

Kempf, S. & Beckmann, U. (2022). Dynamics and long-term evolution of Saturn's E ring particles. in preparation.

Kempf, S., Beckmann, U., Moragas-Klostermeyer, G., Postberg, F., Srama, R., Economou, T., Schmidt, J., Spahn, F. & Grün, E. (2008). The E ring in the vicinity of Enceladus I. Spatial distribution and properties of the ring particles. Icarus, 193(2), 420–437. https://doi.org/10.1016/j.icarus.2007.06.027

Kempf, S., Beckmann, U. & Schmidt, J. (2010). How the Enceladus dust plume feeds Saturn's E ring. Icarus, 206(2), 446–457. https://doi.org/10.1016/j.icarus.2009.09.016

Kempf, S., Beckmann, U., Srama, R., Horanyi, M., Auer, S. & Grün, E. (2006). The electrostatic potential of E ring particles. Planetary and Space Science, 54(9–10), 999–1006. https://doi.org/10.1016/j.pss.2006.05.012

Kempf, S., Horányi, M., Hsu, H. W., Hill, T. W., Juhász, A. & Smith, H. T. (2018). Saturn's Diffuse E Ring and Its Connection with Enceladus. Enceladus and the Icy Moons of Saturn. https://doi.org/10.2458/azu_uapress_9780816537075-ch010

Kempf, S., Srama, R., Horányi, M., Burton, M., Helfert, S., Moragas-Klostermeyer, G., Roy, M. & Grün, E. (2005). (a) High-velocity streams of dust originating from Saturn. Nature, 433(7023), 289–291. https://doi.org/10.1038/nature03218

Kempf, S., Srama, R., Postberg, F., Burton, M., Green, S. F., Helfert, S., Hillier, J. K., McBride, N., Moragas-Klostermeyer, G., Roy, M. & Grün, E. (2005). (b) Composition of Saturnian Stream Particles. Science, 307(5713), 1274–1276. https://doi.org/10.1126/science.1106218

Khawaja, N. A. (2016, Dezember). Organic compounds in Saturn's E-ring and its compositional profile in the vicinity of Rhea (Dissertation). Ruprecht Karls Universität Heidelberg.

Khawaja, N., Postberg, F., Hillier, J., Klenner, F., Kempf, S., Nölle, L., Reviol, R., Zou, Z. & Srama, R. (2019). Low-mass nitrogen-, oxygen-bearing, and aromatic compounds in Enceladean ice grains. Monthly Notices of the Royal Astronomical Society, 489(4), 5231–5243. https://doi.org/10.1093/mnras/stz2280

Klenner, F., Postberg, F., Hillier, J., Khawaja, N., Cable, M. L., Abel, B., Kempf, S., Glein, C. R., Lunine, J. I., Hodyss, R., Reviol, R. & Stolz, F. (2020). (b) Discriminating Abiotic and Biotic Fingerprints of Amino Acids and Fatty Acids in Ice Grains Relevant to Ocean Worlds. Astrobiology, 20(10), 1168–1184. https://doi.org/10.1089/ast.2019.2188

Klenner, F., Postberg, F., Hillier, J., Khawaja, N., Reviol, R., Srama, R., Abel, B., Stolz, F. & Kempf, S. (2019). Analogue spectra for impact ionization mass spectra of water ice grains obtained at different impact speeds in space. Rapid Communications in Mass Spectrometry, 33(22), 1751–1760. https://doi.org/10.1002/rcm.8518

Klenner, F., Postberg, F., Hillier, J., Khawaja, N., Reviol, R., Stolz, F., Cable, M. L., Abel, B. & Nölle, L. (2020). (a) Analog Experiments for the Identification of Trace Biosignatures in Ice Grains from Extraterrestrial Ocean Worlds. Astrobiology, 20(2), 179–189. https://doi.org/10.1089/ast.2019.2065

Lakdawalla, E. (2010, 4. Mai). Saturn's hexagon recreated in the laboratory. The Planetary Society. https://www.planetary.org/articles/2471

Lavila, P. (2002). Analyzing time-of-flight spectra of CDA (Research Report). Max Planck Institut für Kernphysik.

Li, Y. W., Bugiel, S., Trieloff, M., Hillier, J. K., Postberg, F., Price, M. C., Shu, A., Fiege, K., Fielding, L. A., Armes, S. P., Wu, Y. Y., Grün, E. & Srama, R. (2014). Morphology of craters generated by hypervelocity impacts of micron-sized polypyrrole-coated olivine particles. Meteoritics & Planetary Science, 49(8), 1375–1387. https://doi.org/10.1111/maps.12338

Li, Y. W., Srama, R., Bugiel, S., Schilling, A., Trieloff, M., Hillier, J. K., Postberg, F., Fiege, K., Wu, Y. Y. & Grün, E. (2013). MORPHOLOGY OF IMPACT CRATERS GENERATED BY HYPERVELOCITY MICRON-SIZED OLIVINE AND IRON PARTICLES. Proc. '6th European Conference on Space Debris' Darmstadt, Germany, 22–25 April 2013 (ESA SP-723, August 2013).

Linti, S. (2018). Compositional Analysis of Saturn's Inner E Ring and Outer F Ring as seen during Cassini's Ring-Grazing Orbits (Master Thesis, Geosciences). Faculty of Chemistry and Earth Sciences of the Ruprecht-Karls Universität Heidelberg.

Mamyrin, B. A., Karataev, V. I., Shmikk, D. V. & Zagulin, V. A. (1973). The mass-reflectron. A new nonmagnetic time-of-flight high resolution mass-spectrometer. Zhurnal Ehksperimental'noj i Teoreticheskoj Fiziki, 64(1), 82–89.

Mamyrin, B. A. (1993). Laser assisted reflectron time-of-flight mass spectrometry. Internatonal Journal of Mass Spectrometry, 131, 1–19.

Mann, I., Meyer-Vernet, N. & Czechowski, A. (Hrsg.). (2012). Nanodust in the Solar System: Discoveries and Interpretations. Astrophysics and Space Science Library. https://doi.org/10.1007/978-3-642-27543-2

Martin, R. G. & Livio, M. (2012). On the evolution of the snow line in protoplanetary discs. Monthly Notices of the Royal Astronomical Society: Letters, 425(1), L6–L9. https://doi.org/10.1111/j.1745-3933.2012.01290.x

Maxwell, J. C. (1859). On the stability of the motion of Saturn's rings. Cambridge: Macmillan and Co.

McKay, C. P. (2004). What Is Life—and How Do We Search for It in Other Worlds? PLoS Biology, 2(9), e302. https://doi.org/10.1371/journal.pbio.0020302

McKay, C. P., Davila, A., Glein, C. R., Hand, K. P. & Stockton, A. (2018). Enceladus Astrobiology, Habitability, and the Origin of Life. Enceladus and the Icy Moons of Saturn, 437–452. https://doi.org/10.2458/azu_uapress_9780816537075-ch021

Meier, R. (1999). Near Infrared Photometry of the Jovian Ring and Adrastea. Icarus, 141(2), 253–262. https://doi.org/10.1006/icar.1999.6172

Misra, S., Mishra, S. K. & Sodha, M. S. (2012). Charging of ice grains in Saturn's E ring: theory and observations. Monthly Notices of the Royal Astronomical Society, 423(1), 176–184. https://doi.org/10.1111/j.1365-2966.2012.20774.x

Mitchell, C. J., Colwell, J. E. & Horányi, M. (2005). Tenuous ring formation by the capture of interplanetary dust at Saturn. Journal of Geophysical Research: Space Physics, 110(A9). https://doi.org/10.1029/2004ja010577

Mocker, A., Bugiel, S., Auer, S., Baust, G., Colette, A., Drake, K., Fiege, K., Grün, E., Heckmann, F., Helfert, S., Hillier, J., Kempf, S., Matt, G., Mellert, T., Munsat, T., Otto, K., Postberg, F., Röser, H. P., Shu, A., . . . Srama, R. (2011). A 2 MV Van de Graaff accelerator as a tool for planetary and impact physics research. Review of Scientific Instruments, 82(9), 095111. https://doi.org/10.1063/1.3637461

Mocker, A., Hornung, K., Sternovsky, Z., Kempf, S., Johnson, T., GrüN, E. & Srama, R. (2012). A linear tof mass spectrometer as a tool for the investigation of impact ionisation plasma. AIP Conference Proceedings, 1426, 859. https://doi.org/10.1063/1.3686413

Morales-Juberías, R., Sayanagi, K. M., Simon, A. A., Fletcher, L. N. & Cosentino, R. G. (2015). MEANDERING SHALLOW ATMOSPHERIC JET AS A MODEL OF SATURN'S NORTH-POLAR HEXAGON. The Astrophysical Journal, 806(1), L18. https://doi.org/10.1088/2041-8205/806/1/l18

Morbidelli, A., Chambers, J., Lunine, J. I., Petit, J. M., Robert, F., Valsecchi, G. B. & Cyr, K. E. (2000). Source regions and timescales for the delivery of water to the Earth. Meteoritics & Planetary Science, 35(6), 1309–1320. https://doi.org/10.1111/j.1945-5100.2000.tb01518.x

Morfill, G. E., Grün, E. & Johnson, T. V. (1983). Saturn's E, G, and F rings: Modulated by the plasma sheet? Journal of Geophysical Research, 88(A7), 5573. https://doi.org/10.1029/ja088ia07p05573

NASA/JPL. (2006, 11. Oktober). NASA Finds Saturn's Moons May Be Creating New Rings (Cassini-Huygens Press Release). saturn.jpl.nasa.gov. https://web.archive.org/web/20061016081210/http://saturn.jpl.nasa.gov/news/press-release-details.cfm?newsID=698

NASA/JPL/CICLOPS/Space Science Institute. (2008, 5. September). CASSINI IMAGES RING ARCS AMONG SATURN'S MOONS (Cassini-Huygens Press Release). CASSINI IMAGING CENTRAL LABORATORY FOR OPERATIONS (CICLOPS). http://ciclops.org/view.php?id=5253

Nicholson, P. D., Showalter, M. R., Dones, L., French, R. G., Larson, S. M., Lissauer, J. J., McGhee, C. A., Seitzer, P., Sicardy, B. & Danielson, G. E. (1996). Observations of Saturn's Ring-Plane Crossings in August and November 1995. Science, 272(5261), 509–515. https://doi.org/10.1126/science.272.5261.509

Pang, K. D., Voge, C. C., Rhoads, J. W. & Ajello, J. M. (1984). The E ring of Saturn and satellite Enceladus. Journal of Geophysical Research, 89(B11), 9459. https://doi.org/10.1029/jb089ib11p09459

Pitman, K. M., Buratti, B. J. & Mosher, J. A. (2010). Disk-integrated bolometric Bond albedos and rotational light curves of saturnian satellites from Cassini Visual and Infrared Mapping Spectrometer. Icarus, 206(2), 537–560. https://doi.org/10.1016/j.icarus.2009.12.001

PODOLAK, M. & ZUCKER, S. (2004). A note on the snow line in protostellar accretion disks. Meteoritics & Planetary Science, 39(11), 1859–1868. https://doi.org/10.1111/j.1945-5100.2004.tb00081.x

Porco, C. C., Helfenstein, P., Thomas, P. C., Ingersoll, A. P., Wisdom, J., West, R., Neukum, G., Denk, T., Wagner, R., Roatsch, T., Kieffer, S., Turtle, E., McEwen, A., Johnson, T. V., Rathbun, J., Veverka, J., Wilson, D., Perry, J., Spitale, J., . . . Squyres, S. (2006). Cassini Observes the Active South Pole of Enceladus. Science, 311(5766), 1393–1401. https://doi.org/10.1126/science.1123013

Postberg, F. (2007). A New View on the Composition of Dust in the Solar System: Results from the Cassini Dust Detector (Dissertation). Ruprecht Karls Universität Heidelberg.

Postberg, F., Clark, R. N., Hansen, C. J., Coates, A. J., Dalle Ore, C. M., Scipioni, F., Hedman, M. M. & Waite, J. H. (2018). (b) Plume and Surface Composition of Enceladus. Enceladus and the Icy Moons of Saturn. https://doi.org/10.2458/azu_uapress_9780816537075-ch007

Postberg, F., Kempf, S., Hillier, J., Srama, R., Green, S., McBride, N. & Grün, E. (2008). The E-ring in the vicinity of Enceladus II. Probing the moon's interior—The composition of E-ring particles. Icarus, 193(2), 438–454. https://doi.org/10.1016/j.icarus.2007.09.001

Postberg, F., Kempf, S., Rost, D., Stephan, T., Srama, R., Trieloff, M., Mocker, A. & Goerlich, M. (2009). (b) Discriminating contamination from particle components in spectra of Cassini's dust detector CDA. Planetary and Space Science, 57(12), 1359–1374. https://doi.org/10.1016/j.pss.2009.06.027

Postberg, F., Kempf, S., Schmidt, J., Brilliantov, N., Beinsen, A., Abel, B., Buck, U. & Srama, R. (2009). (a) Sodium salts in E-ring ice grains from an ocean below the surface of Enceladus. Nature, 459(7250), 1098–1101. https://doi.org/10.1038/nature08046

Postberg, F., Kempf, S., Srama, R., Green, S., Hillier, J., McBride, N. & Grün, E. (2006). Composition of jovian dust stream particles. Icarus, 183(1), 122–134. https://doi.org/10.1016/j.icarus.2006.02.001

Postberg, F., Khawaja, N., Abel, B., Choblet, G., Glein, C. R., Gudipati, M. S., Henderson, B. L., Hsu, H. W., Kempf, S., Klenner, F., Moragas-Klostermeyer, G., Magee, B., Nölle, L., Perry, M., Reviol, R., Schmidt, J., Srama, R., Stolz, F., Tobie, G., . . . Waite, J. H. (2018). (a) Macromolecular organic compounds from the depths of Enceladus. Nature, 558(7711), 564–568. https://doi.org/10.1038/s41586-018-0246-4

Postberg, F., Schmidt, J., Hillier, J., Kempf, S. & Srama, R. (2011). (a) A salt-water reservoir as the source of a compositionally stratified plume on Enceladus. Nature, 474(7353), 620–622. https://doi.org/10.1038/nature10175

Reipurth, B., Jewitt, D. & Keil, K. (2007). Protostars and Planets V. University of Arizona Press.

Sanchez-Lavega, A. (1994). Saturn's Great White Spots. Chaos: An Interdisciplinary Journal of Nonlinear Science, 4(2), 341–353. https://doi.org/10.1063/1.166012

Sánchez-Lavega, A. & Battaner, E. (1987). The nature of Saturn's atmospheric Great White Spots. Astronomy and Astrophysics, 185, 315–326.

Sánchez-Lavega, A., del Río-Gaztelurrutia, T., Delcroix, M., Legarreta, J. J., Gómez-Forrellad, J. M., Hueso, R., García-Melendo, E., Pérez-Hoyos, S., Barrado-Navascués, D. & Lillo, J. (2012). Ground-based observations of the long-term evolution and death of Saturn's 2010 Great White Spot. Icarus, 220(2), 561–576. https://doi.org/10.1016/j.icarus.2012.05.033

Schmidt, J., Brilliantov, N., Spahn, F. & Kempf, S. (2008). Slow dust in Enceladus' plume from condensation and wall collisions in tiger stripe fractures. Nature, 451(7179), 685–688. https://doi.org/10.1038/nature06491

Seager, S. & Dotson, R. Ž. (2010). Exoplanets. University of Arizona Press.

Showalter, M. R., N. Cuzzi, J. & Larson, S. M. (1991). Structure and particle properties of Saturn's E Ring. Icarus, 94(2), 451–473. https://doi.org/10.1016/0019-1035(91)90241-k

SMITH, B. A., SODERBLOM, L., BATSON, R., BRIDGES, P., INGE, J., MASURSKY, H., SHOEMAKER, E., BEEBE, R., BOYCE, J., BRIGGS, G., BUNKER, A., COLLINS, S. A., HANSEN, C. J., JOHNSON, T. V., MITCHELL, J. L., TERRILE, R. J., COOK, A. F., CUZZI, J., POLLACK, J. B., . . . SUOMI, V. E. (1982). A New Look at the Saturn System: The Voyager 2 Images. Science, 215(4532), 504–537. https://doi.org/10.1126/science.215.4532.504

SMITH, B. A., SODERBLOM, L., BEEBE, R., BOYCE, J., BRIGGS, G., BUNKER, A., COLLINS, S. A., HANSEN, C. J., JOHNSON, T. V., MITCHELL, J. L., TERRILE, R. J., CARR, M., COOK, A. F., CUZZI, J., POLLACK, J. B., DANIELSON, G. E., INGERSOLL, A., DAVIES, M. E., HUNT, G. E., . . . SUOMI, V. E. (1981). Encounter with Saturn: Voyager 1 Imaging Science Results. Science, 212(4491), 163–191. https://doi.org/10.1126/science.212.4491.163

Spahn, F., Albers, N., Hörning, M., Kempf, S., Krivov, A. V., Makuch, M., Schmidt, J., Seiß, M. & Miodrag Sremčević. (2006). (b) E ring dust sources: Implications from Cassini's dust measurements. Planetary and Space Science, 54(9–10), 1024–1032. https://doi.org/10.1016/j.pss.2006.05.022

Spahn, F., Schmidt, J., Albers, N., Hörning, M., Makuch, M., Seiß, M., Kempf, S., Srama, R., Dikarev, V., Helfert, S., Moragas-Klostermeyer, G., Krivov, A. V., Sremcevic, M., Tuzzolino, A. J., Economou, T. & Grün, E. (2006). (a) Cassini Dust Measurements at Enceladus and Implications for the Origin of the E Ring. Science, 311(5766), 1416–1418. https://doi.org/10.1126/science.1121375

Spencer, J. R. & Nimmo, F. (2013). Enceladus: An Active Ice World in the Saturn System. Annual Review of Earth and Planetary Sciences, 41(1), 693–717. https://doi.org/10.1146/annurev-earth-050212-124025

Spencer, J. R., Pearl, J. C., Segura, M., Flasar, F. M., Mamoutkine, A., Romani, P., Buratti, B. J., Hendrix, A. R., Spilker, L. J. & Lopes, R. M. C. (2006). Cassini Encounters Enceladus: Background and the Discovery of a South Polar Hot Spot. Science, 311(5766), 1401–1405. https://doi.org/10.1126/science.1121661

Srama, R. (2009). Cassini-Huygens and Beyond-Tools for Dust Astronomy (Habilitation). Universität Stuttgart.

Srama, R., Ahrens, T. J., Altobelli, N., Auer, S., Bradley, J. G., Burton, M., Dikarev, V. V., Economou, T., Fechtig, H., Görlich, M., Grande, M., Graps, A., Grün, E., Havnes, O., Helfert, S., Horanyi, M., Igenbergs, E., Jessberger, E. K., Johnson, T. V., . . . Zook, H. A. (2004). The Cassini Cosmic Dust Analyzer. Space Science Reviews, 114(1–4), 465–518. https://doi.org/10.1007/s11214-004-1435-z

Srama, R., Kempf, S., Moragas-Klostermeyer, G., Altobelli, N., Auer, S., Beckmann, U., Bugiel, S., Burton, M., Economomou, T., Fechtig, H., Fiege, K., Green, S. F., Grande, M., Havnes, O., Hillier, J. K., Helfert, S., Horanyi, M., Hsu, S., Igenbergs, E., . . . Röser, H. P. (2011). The cosmic dust analyser onboard cassini: ten years of discoveries. CEAS Space Journal, 2(1–4), 3–16. https://doi.org/10.1007/s12567-011-0014-x

Srama, R., Kempf, S., Moragas-Klostermeyer, G., Helfert, S., Ahrens, T., Altobelli, N., Auer, S., Beckmann, U., Bradley, J., Burton, M., Dikarev, V., Economou, T., Fechtig, H., Green, S., Grande, M., Havnes, O., Hillier, J., Horanyi, M., Igenbergs, E., . . . Grün, E. (2006). In situ dust measurements in the inner Saturnian system. Planetary and Space Science, 54(9–10), 967–987. https://doi.org/10.1016/j.pss.2006.05.021

Srama, R., Woiwode, W., Postberg, F., Armes, S. P., Fujii, S., Dupin, D., Ormond-Prout, J., Sternovsky, Z., Kempf, S., Moragas-Klostermeyer, G., Mocker, A. & Grün, E. (2009). Mass spectrometry of hyper-velocity impacts of organic micrograins. Rapid Communications in Mass Spectrometry, 23(24), 3895–3906. https://doi.org/10.1002/rcm.4318

Stephan, T. (2001). TOF-SIMS in cosmochemistry. Planetary and Space Science, 49(9), 859–906. https://doi.org/10.1016/s0032-0633(01)00037-x

Tamayo, D., Hedman, M. M. & Burns, J. A. (2014). First observations of the Phoebe ring in optical light. Icarus, 233, 1–8. https://doi.org/10.1016/j.icarus.2014.01.021

Timmermann, R. & Grün, E. (1991). Plasma Emission from High Velocity Impacts of Microparticles Onto Water Ice. International Astronomical Union Colloquium, 126, 375–378. https://doi.org/10.1017/s0252921100067154

Tomasko, M. G., Archinal, B., Becker, T., Bézard, B., Bushroe, M., Combes, M., Cook, D., Coustenis, A., de Bergh, C., Dafoe, L. E., Doose, L., Douté, S., Eibl, A., Engel, S., Gliem, F., Grieger, B., Holso, K., Howington-Kraus, E., Karkoschka, E., . . . West, R. (2005). Rain, winds and haze during the Huygens probe's descent to Titan's surface. Nature, 438(7069), 765–778. https://doi.org/10.1038/nature04126

Verbiscer, A. J., Skrutskie, M. F. & Hamilton, D. P. (2009). Saturn's largest ring. Nature, 461(7267), 1098–1100. https://doi.org/10.1038/nature08515

Waite Jr., J. H., Combi, M. R., Ip, W.-H., Cravens, T. E., McNutt Jr., R. L., Kasprzak, W., Yelle, R., Luhmann, J., Niemann, H., Gell, D., Magee, B., Fletcher, G., Lunine, J. & Tseng, W.-L. (2006). Cassini Ion and Neutral Mass Spectrometer: Enceladus Plume Composition and Structure. Science, 311(5766), 1419–1422. https://doi.org/10.1126/science.1121290

Westphal, A. J., Stroud, R. M., Bechtel, H. A., Brenker, F. E., Butterworth, A. L., Flynn, G. J., Frank, D. R., Gainsforth, Z., Hillier, J. K., Postberg, F., Simionovici, A. S., Sterken, V. J., Nittler, L. R., Allen, C., Anderson, D., Ansari, A., Bajt, S., Bastien, R. K., Bassim, N., . . . Zolensky, M. E. (2014). Evidence for interstellar origin of seven dust particles collected by the Stardust spacecraft. Science, 345(6198), 786–791. https://doi.org/10.1126/science.1252496

Whitehouse, D. (2009). Renaissance Genius: Galileo Galilei and His Legacy to Modern Science. Sterling Publishing Company.

Wiederschein, F., Vöhringer-Martinez, E., Beinsen, A., Postberg, F., Schmidt, J., Srama, R., Stolz, F., Grubmüller, H. & Abel, B. (2015). Charge separation and isolation in strong water droplet impacts. Physical Chemistry Chemical Physics, 17(10), 6858–6864. https://doi.org/10.1039/c4cp05618c

Ye, S., Gurnett, D. & Kurth, W. (2016). In-situ measurements of Saturn's dusty rings based on dust impact signals detected by Cassini RPWS. Icarus, 279, 51–61. https://doi.org/10.1016/j.icarus.2016.05.006

Zebker, H. A., Marouf, E. A. & Leonard Tyler, G. (1985). Saturn's rings: Particle size distributions for thin layer models. Icarus, 64(3), 531–548. https://doi.org/10.1016/0019-1035(85)90074-0

Zhang, Z. M., Chen, S. & Liang, Y. Z. (2010). Baseline correction using adaptive iteratively reweighted penalized least squares. The Analyst, 135(5), 1138. https://doi.org/10.1039/b922045c

Zou, Z. (2021). The composition of salt-rich ice grains emitted by Enceladus' cryo-volcanic plume and implications for the subsurface ocean (Dissertation). Freie Universität Berlin

(Compiled with the Scribbr APA-generator: https://www.scribbr.de/zitieren/apa-generator/)

# Author contact

Lenz Nölle

Telephone: +49 30 838 66056

Official email: lenz.noelle@fu-berlin.de

# I. Danksagung

Nach einer langen Zeit geht nun ein Kapitel meines Lebens zu Ende und viele haben zu seinem Gelingen beigetragen. Den wichtigsten möchte ich hier meinen Dank aussprechen.

Als erstes möchte ich meinem Betreuer Prof. Frank Postberg danken. Er hat es mir nicht nur möglich gemacht, an diesem tollen Thema zu arbeiten, sondern auch an vielen weiteren, interessanten Themen und das stets in einer angenehmen und produktiven Atmosphäre. Auch danke ich ihm für die während dieser Zeit entgegengebrachte Geduld und Unterstützung, sowie die Möglichkeit der Teilnahme an diversen Konferenzen, wodurch ich mein Wissen und meine Fähigkeiten testen und erweitern konnte.

Der nächste Dank richtet sich an Dr. Jon K. Hillier, der meine Arbeit Korrektur gelesen hat und auch sonst immer mit Rat und Tat hilfreich zur Stelle war. Ich wünsche seiner Frau, ihm und ihrem jüngsten Zuwachs Tristan alles Gute für die Zukunft.

Ebenso möchte ich mich bei Prof. Jürgen Schmidt bedanken, der sich bereit erklärt hat der zweite Gutachter meiner Dissertation zu werden.

Meinem ehemaligen Kommilitonen und langjährigen Kollegen Dr. Fabian Klenner danke ich vielmals für seine Anregungen und intensive Mitarbeit im Zuge der Laborexperimente mit dem LILBID Experiment, durch die dieser Teil der Dissertation überhaupt erst möglich geworden ist.

Meinem langjährigen Kollegen Dr. Nozair Ashraf Khawaja danke ich für die vielen, konstruktiven Gespräche zu meiner Dissertation sowie darüber hinaus und die stets angenehme, produktive Zusammenarbeit über die Jahre hinweg. Ich wünsche ihm und seiner Familie weiterhin alles Gute.

Auch möchte ich mich bei den Kollegen am LASP in Boulder, Colorado (USA) und IRS in Stuttgart bedanken, die durch die Bereitstellung der CDA Spektren, SPICE Daten und den dazugehörigen Softwareanwendungen, die Arbeit an und mit den CDA Spektren erst grundlegend möglich gemacht haben. Besonderen Dank gebühren dabei Prof. Sascha Kempf und Dr. Hsiang-Wen (Sean) Hsu aus Boulder, sowie Dr. Ralf Srama, Georg Moragas-Klostermeyer und Dr. Thomas Albin aus Stuttgart. Vielen Dank dafür.

Bei meinem Kollegen Muhammad Umair möchte ich mich für die tolle Unterstützung mit der Nachbearbeitung der LILBID Spektren bedanken, welche die Qualität der Laborergebnisse nochmals deutlich verbessert hat.

Simon Linti, René Reviol sowie den anderen Kolleginnen und Kollegen der Forschungsgruppe Planetologie und Fernerkundung danke ich für die zahlreichen anregenden Gespräche und die angenehme, gemeinsame Zeit.

Mein vermeintlich letzter aber dafür herzlichster Dank geht an meine gesamte Familie, die mich über all die Jahre immer und in jeder Hinsicht unterstützt hat. Ohne ihre kontinuierliche Unterstützung wäre diese Arbeit in dieser Form nicht möglich gewesen. Danke für alles, ohne euch wäre ich nicht da wo ich jetzt bin!

# J. Eidesstattliche Erklärung/Statutory Declaration

Hiermit erkläre ich, dass die vorliegende Dissertation mit dem Thema:

***Multidimensional scan of the Saturnian E-ring based on the data record of Cassini's Comic Dust Analyzer***

selbstständig von mir verfasst und angefertigt wurde. Es wurden außerdem keine anderen als die angegebenen Quellen und Hilfsmittel verwendet habe. Geistiges Eigentum anderer Autoren wurde als entsprechend gekennzeichnet. Ebenso versichere ich, dass ich an keiner anderen Stelle ein Prüfungsverfahren beantragt bzw. die Dissertation in dieser oder anderer Form an keiner anderen Fakultät als Dissertation vorgelegt habe.

Berlin, den _____ _____

(Lenz Nölle)